NOTE TO USERS

This reproduction is the best copy available.

UMI®

An Observational and Modeling Study of a Heavy Orographic Precipitation Event over the Oregon Cascades.

Matthew F. Garvert

A dissertation submitted in partial fulfillment
of the requirements for the degree of

Doctor of Philosophy

University of Washington

2005

Program Authorized to Offer Degree: Atmospheric Sciences

UMI Number: 3198788

Copyright 2005 by
Garvert, Matthew F.

All rights reserved.

INFORMATION TO USERS

The quality of this reproduction is dependent upon the quality of the copy
submitted. Broken or indistinct print, colored or poor quality illustrations and
photographs, print bleed-through, substandard margins, and improper
alignment can adversely affect reproduction.

In the unlikely event that the author did not send a complete manuscript
and there are missing pages, these will be noted. Also, if unauthorized
copyright material had to be removed, a note will indicate the deletion.

UMI®

UMI Microform 3198788
Copyright 2006 by ProQuest Information and Learning Company.
All rights reserved. This microform edition is protected against
unauthorized copying under Title 17, United States Code.

ProQuest Information and Learning Company
300 North Zeeb Road
P.O. Box 1346
Ann Arbor, MI 48106-1346

University of Washington
Graduate School

This is to certify that I have examined this copy of a doctoral dissertation by
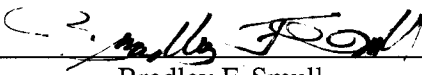
Matthew F. Garvert

and have found that it is complete and satisfactory in all respects,
and that any and all revisions required by the final
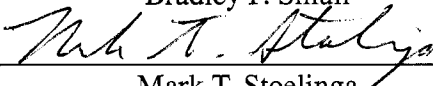examining committee have been made.

Chair of the Supervisory Committee:

_____

Clifford Mass

Reading Committee:

_____

Clifford F. Mass

_____

Bradley F. Smull

_____

Mark T. Stoelinga

Date: _____12/05/2005_____

University of Washington

Abstract

An Observational and Modeling Study of a Heavy Orographic Precipitation Event over the Oregon Cascades.

Matthew F. Garvert

Chair of the Supervisory Committee:
Professor Clifford Mass
Atmospheric Sciences

During 13-14 December 2001, a comprehensive set of observations over the central Oregon Cascades was collected as part of the IMPROVE-2 field project, permitting an unprecedented opportunity for the investigation of a heavy precipitation event over complex terrain. The collection of thermodynamic and kinematic observations concomitantly with microphysical measurements also provided a unique chance to isolate errors in a mesoscale scale model's microphysical parameterization which may be contributing to errors in quantitative precipitation forecasting. The Fifth Generation Penn State / NCAR Mesoscale Model (MM5) version 3.5 was run at various resolutions to simulate the 13-14 December 2001 system and verified against the vast observational dataset. The MM5's depiction of the synoptic features of the storm system was sufficiently accurate to permit further comparisons of mesoscale and microphysical data with the model.

High-resolution model simulations and comprehensive airborne Doppler radar observations identified kinematic structures influencing the production and mesoscale distribution of precipitation and associated microphysical processes. Two distinct scales of mesoscale wave-like air motions were identified: (1) a vertically-propagating mountain wave anchored to the Cascade crest associated with strong mid-level zonal (i.e. cross barrier) flow, and (2) smaller-scale (< 20 km horizontal wavelength) undulations over the windward foothills

triggered by interaction of the low-level along-barrier flow with multiple ridge-valley corrugations oriented perpendicular to the Cascade crest. Microphysical budgets and sensitivity analyses were also performed for the precipitation event and identified important parameters and assumptions in the model's microphysical parameterizations that should be rectified to improve quantitative precipitation forecasting.

TABLE OF CONTENTS

LIST OF FIGURES

iv

LIST OF TABLES

ACKNOWLEDGMENTS

I would like to express my sincere appreciation to my thesis advisor, Cliff Mass, and the remainder of my committee for their generous contributions to this work. Additionally, I want to acknowledge all of my friends, in- and outside the Atmospheric Sciences department, for the countless memories over the past six years. Lastly, I would like to thank my parents for their support over the years.

Chapter 1

INTRODUCTION

1.1 Overview and Motivation

Quantitative precipitation forecasting (QPF) has been identified as one of the most significant challenges of weather forecasting. Yet despite its importance, improvements in QPF have been relatively slow (Fritsch et al., 1998) with significant problems evident in numerical model simulations of precipitation distributions and amounts (Colle et al., 1999; Colle and Mass, 2000). Such deficiencies are particularly evident over orography where the complex interaction of terrain and microphysical processes produce large gradients in precipitation totals and distributions.

In a report of the Eighth Prospectus Development Team of the U.S Weather Research Program (USWRP), several strategic goals were set forth to improve QPF based upon integrating the increased understanding of microphysical processes with substantial advances in numerical modeling (Fritsch et al., 1998). It was recognized that achieving a comprehensive verification of the microphysical assumptions and predicted precipitation processes against a combination of in situ and remotely sensed microphysical observations was critical. Also, it was imperative that these microphysical measurements be taken concurrently with observations of wind, temperature, and humidity, so that errors in the simulated microphysics could be isolated from errors in these other predicted fields. Until the IMPROVE project, few dedicated efforts have been undertaken to verify and improve the microphysical parameterizations in this manner.

1.1.1   Increased Understanding of Precipitation Processes Over Terrain

Over recent decades the theoretical understanding of microphysical processes over mountainous terrain has substantially improved. Smith (1979) provided an extensive review of orographic precipitation mechanisms, recognizing the complex interaction between precipitation distribution and terrain influences. Smith (1979) noted that several factors are important to the orographic modification of precipitation including: the thermodynamic and kinematic properties of the upstream airflow; the height, width and shape of the barrier; and the microphysical processes leading to the formation of hydrometeors. Several questions were also raised regarding the efficiency of precipitation release during orographic lifting and the interaction between frontal and upslope precipitation.

In addition to Smiths' (1979) extensive review, a large number of research studies and field projects have enhanced the understanding of precipitation and kinematic processes over topography. The Cascade Project during the early 1970s examined land-falling storms over the Cascade Mountains of the Pacific Northwest. Using both airborne and ground-based observations, the study documented the structure of frontal systems as they interacted with topography as well as the differences in precipitation distributions along the windward and lee slopes of the Cascades (Hobbs, 1975). The research found that precipitation amounts increased by a factor of two to three over the windward slopes of the Washington Cascades compared to upstream Puget Sound locations, while lee sites experienced a reduction in precipitation compared to Puget Sound sites. It was found that growth of precipitation particles via riming and aggregation were both important microphysical processes contributing to enhanced precipitation amounts on the windward slopes.

More recent field studies such as the Coastal Observation and Simulation with Topography Experiment [COAST; Bond et al. (1997)], the California Land-Falling Jets Experiment [CALJET; Neiman et al. (2002)], the Sierra Cooperative Pilot Project [SIERRA: Reynolds and Arnett (1986)], and the Mesoscale Alpine Project [MAP; Bougeault et al. (2001)] have highlighted the importance of the dynamics and kinematics of the upstream flow on the

distribution of orographic precipitation. In a study of Sierra storms, Marwitz (1982, 1987a) showed the presence of a pronounced barrier jet over the windward slopes of the Sierra Mountains. Such storms were associated with the approach of a baroclinic zone and strong, stable prefrontal flow impinging upon the 2-km high barrier of the Sierra Mountains. Marwitz (1987b) and Rauber (1992) found that upstream convergence due to blocking created areas of high cloud liquid water (CLW) amounts and a displacement of maximum precipitation to well upstream of the crest. Additional evidence of upstream flow blocking and its impact on precipitation processes has been documented in the European Alps (Rotunno and Ferretti, 2001; Medina and Houze, 2003; Bousquet and Smull, 2003b) and the Wasatch Mountains of Utah (Cox et al., 2005).

On smaller spatial scales (horizontal scales < 20 km), studies over the Mogollon Rim area of Arizona showed that gravity waves generated by topography contributed to the modification of the precipitation distribution across the barrier. Bruintjes et al. (1994) observed enhanced small-scale vertical velocities, associated with the gravity waves, that extended through deep layers of the atmosphere. These gravity waves were excited by hills upwind of the main barrier and produced high CLW independent of the large-scale baroclinic storm system. The CLW regions were shown to greatly affect precipitation rates and the distribution of precipitation.

1.1.2 Advancements in Numerical Weather Prediction (NWP) Modeling

Coinciding with these advancements in the understanding of orographic precipitation processes, a significant increase in computational power has provided the ability to use mesoscale models for research and real-time simulations at high resolutions. Studies have shown that mesoscale models, when run at sufficiently high resolution, are capable of simulating accurately the complex kinematic and dynamical structures associated with mountainous terrain (Steenburgh and Mass, 1996; Doyle et al., 2000; Cairns and Corey, 2003). For example, Colle and Mass (1996) showed that a MM5 model simulation with a resolution of 3 km was able to realistically model the complex mesoscale features associated with a passage of a

cold front interacting with the Olympic Mountains of Washington. Yet despite the ability of mesoscale models to simulate the complex kinematic and dynamic responses caused by terrain, deficiencies in QPF prediction remain.

1.1.3   Problems with Quantitative Precipitation Forecasting (QPF)

Improvements in precipitation distributions through increasing model resolution (Westrick, 1998; Colle et al., 2000) have only provided limited success and do not significantly improve the accuracy of QPF. In an analysis of cool season storms over the Pacific Northwest, Colle et al. (2000) indicated that high-resolution model simulations consistently overpredicted precipitation amounts over the windward slopes of the Cascade Mountains and underpredicted precipitation amounts to the lee. Other research has validated these findings (Colle and Mass, 2000; Colle et al., 2003).

Most high-resolution mesoscale models' QPFs rely on bulk microphysical parameterizations (BMPs) that treat precipitation processes at the grid scale. BMPs predict mixing ratios for a limited number of cloud and precipitation hydrometeor types based upon a complex array of empirically and theoretically derived sources, sinks and exchange terms. Research has indicated that despite the complexity of these schemes serious flaws are present (Manning and Davis, 1997; Colle and Mass, 2000).

Previous field experiments such as COAST, CALJET, and MAP did not obtain sufficiently comprehensive data for the evaluation of the BMPs in mesoscale models, due to either a lack of key observing platforms and instruments or different goals in the use of such platforms (Stoelinga et al., 2003). Although some two-dimensional simulations have already been used to investigate sensitivities of BMPs (Meyers and Cotton, 1992; Colle and Zeng, 2004b; Thompson et al., 2004), there remained a lack of comprehensive observations to evaluate and isolate problems with the BMPs.
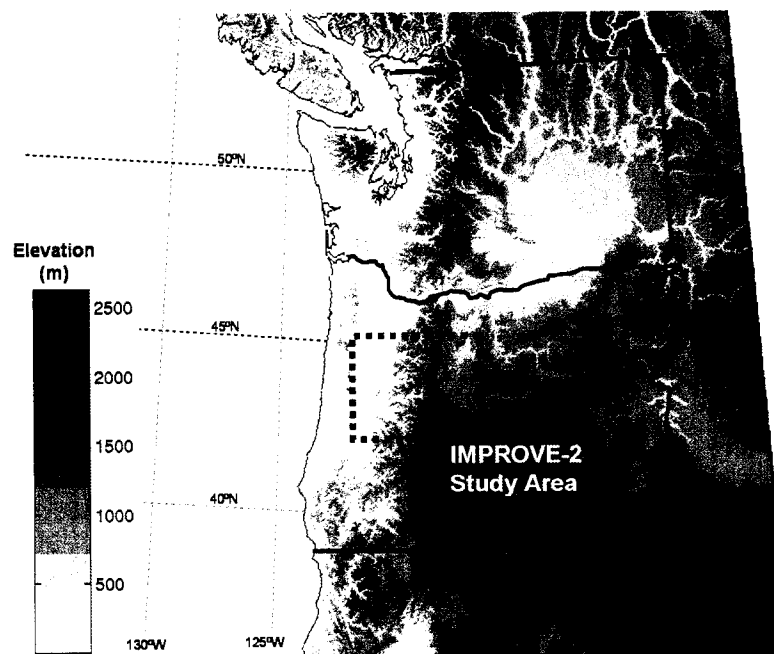
Figure 1.1: Topographic map of the Pacific Northwest with the IMPROVE-2 study area delineated by box.

1.2 IMPROVE Project

The data collected during second phase of the Improvement of Microphysical PaRameterization through Observational Verification Experiment (IMPROVE-2) provides a unique opportunity to examine the kinematics, dynamics and microphysical processes over topography and assess the validity of present day numerical model BMPs. The IMPROVE-2 field experiment, which took place in November and December 2001 over the Oregon Cascades (Fig. 1.1) collected an unparalleled and comprehensive set of observations that provided a detailed depiction of the thermodynamic and kinematic structure of many precipitation events (Stoelinga et al., 2003). In situ microphysical data were also obtained, thereby providing an opportunity to directly diagnose the representations in the BMP of important microphysical processes.

6

1.3 Thesis Goals

This thesis will utilize a high resolution numerical model and the comprehensive obser-
vational data-set of IMPROVE-2 to extensively examine a heavy orographic precipitation
event over the Oregon Cascades. Specific attention is focused on the verification of the
model's simulated kinematic fields and microphysical processes, which may be contribut-
ing to errors in the QPF. The detailed goals of the thesis are as follows:

- Perform simulations of an IMPROVE-2 case with a high-resolution mesoscale model
  that includes a state-of-the-art BMP.

- Determine possible errors in the model's representation of the observed kinematic
  fields (including mountain waves) using in situ flight measurements and remote sens-
  ing observations via airborne Doppler radar.

- Diagnose the important kinematics and associated microphysical processes that con-
  tribute to the observed surface precipitation distribution. Specifically examine the
  spatial changes in precipitation species and processes related to mountain waves that
  may be contributing to errors with model QPF.

- Compare the observed concentrations and size distributions of the observed hydrom-
  eteors against the simulated microphysical fields. Assess the accuracy of the assump-
  tions in the BMP against microphysical observations.

- Calculate a microphysical budget and perform sensitivity tests to identify potential
  problems and inaccurate assumptions in the model BMP that may be contributing to
  errors in QPF.

Chapter 2

DATA AND MODEL DESCRIPTION

2.1 IMPROVE-2 Observational Data-Set

In order to isolate deficiencies in the model's BMP, a large number of in situ and remotely sensed measurements of cloud and precipitation structures are required concomitantly with extensive observations of the kinematic and thermodynamic fields. To meet this need, a variety of instrumental platforms were deployed during IMPROVE-2 with a subset of them being listed in Table 2.1; their positions are indicated in Fig 2.1. For a complete list of the instrumental platforms deployed during IMPROVE-2 the reader is referred to Stoelinga et al. (2003).

Three important observational platforms used during IMPROVE-2 included the UW-Convair-580 research aircraft, NCAR S-band dual-polarization radar (S-Pol) and the National Oceanic and Atmospheric Administration (NOAA) P-3 research aircraft with tail-mounted Doppler radar. The Convair performed vertically-stacked southwest-northeast oriented horizontal flight legs (white dashed line in Fig. 2.1) and gathered microphysical data at a number of altitudes, thereby providing detailed depictions of cloud and precipitation growth within the storm systems. Microphysical instruments aboard the Convair included the PMS 2D-C (Knollenburg, 1976), a Stratton Park Engineering Company (SPEC) high-volume precipitation spectrometer (HVPS) (Lawson et al., 1993), and a Particle Measuring System (PMS) FSSP probe.

The NCAR S-Pol radar located upstream of the Cascade crest (SPL in Fig 2.1) also provided hydrometeor type information as well as reflectivity and radial velocity measurements. A second land-based radar, the NOAA / ETL vertically pointing S-band Doppler radar (White et al., 2000), was positioned over McKenzie Bridge, Oregon (MB in 2.1) and
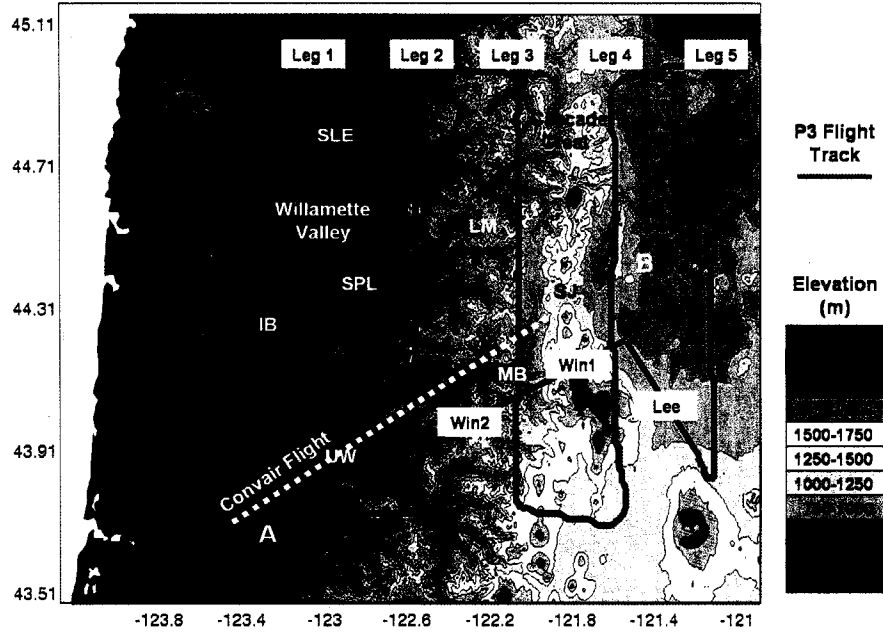
Figure 2.1: Map of the IMPROVE-2 study area with Convair and P-3 flight tracks displayed. Other observational assets are listed in Table 2.1

obtained reflectivity and kinematic data at very high temporal resolution (3-8s). The specifications and scanning strategies of both these radars are described in detail in Houze and Medina (2005).

Concurrently with collection of the S-Pol and Convair data, a valuable additional source of kinematic and microphysical data was gathered by the NOAA P-3 aircraft. The P-3 performed a "lawnmower" flight track, consisting of five north-south (N-S) flight legs at various elevations beginning over the Willamette Valley and concluding downwind (east) of the Oregon Cascade mountains. The individual legs were ~130-140 km long in the N-S direction with ~40 km spacing between each leg (red line in Fig. 2.1). The P-3 also performed a cross-mountain transect at minimum allowable altitudes, providing detailed measurements in the lee of the mountain (Lee in Fig. 2.1), above the windward slopes (Win 1 in Fig. 2.1),

Table 2.1: List of observational assets deployed during IMPROVE-2. The locations of the observations are displayed in Fig 2.1.

Observational Assets deployed during IMPROVE2	
UW Convair-580 research aircraft	White Dashed Line
NOAA P-3 research aircraft	Solid Red Line
NCAR S-Pol Radar	SPL
ETL S-band Profiler	IB
Special mobile rawindsondes	UW
Special NWS rawindsondes	SLE
Little Meadows Rain Gauge	LF
NCAR Scanning Microwave Radiometer	SJ

and above the windward foothills (Win 2 in Fig. 2.1). An accelerometer and associated static pressure port measurements aboard the P-3 provided continuous measurements of vertical air motions and horizontal winds. In addition, onboard the P-3 were Particle Measuring System (PMS) 2D-C and 2D-P grayscale imagery probes and two CLW measuring devices (a PMS Commonwealth Scientific and Industrial Organization (CSIRO) King probe (King et al., 1978) and a Johnson-Williams (J-W) probe (Baumgardner, 1983).

The P-3 was also equipped with airborne Doppler radar to gather kinematic information over the complex terrain of the Cascades. Using the fore- and aft-scanning technique (Frush et al., 1986; Jorgensen and Smull, 1993; Hildebrand, 1998), 3D-reflectivity and radial velocity data were gathered within five overlapping ~40 km wide volumes centered along each of five N-S oriented flight legs (Fig.2.1). The regular spacing of these five legs provided continuous, overlapping dual-Doppler coverage over the sizable IMPROVE-2 study area, and is thus extremely well suited for evaluation of mesoscale simulations of terrain-modified airflow and precipitation processes.
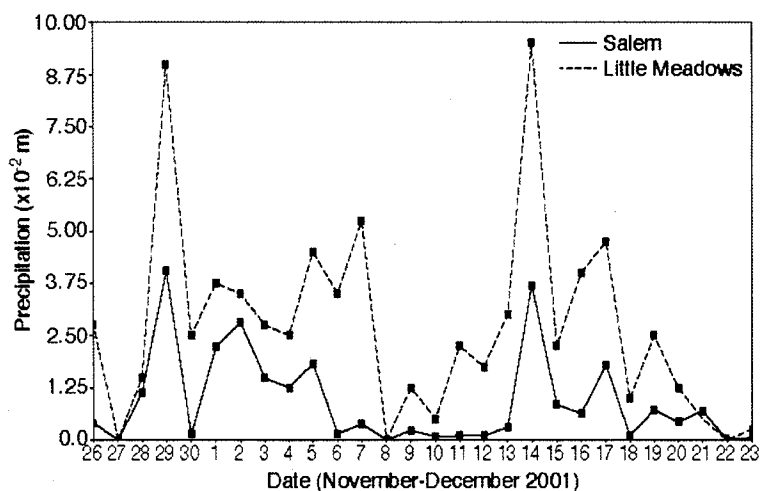
Figure 2.2: IMPROVE-2 time series of daily precipitation from Salem and Little Meadows rain gauges from Houze and Medina (2005).

2.2 13-14 December 2001 Event

During the IMPROVE-2 field campaign, which took place from 26 November 2001 to 22 December 2001, 16 shortwave troughs passed over central Oregon. Stations in the study area generally received half a standard deviation above the normal precipitation for the month of December as onshore flow and troughing persisted over the eastern Pacific (Stoelinga et al., 2003). A time series of daily precipitation amounts from two stations, Salem, located over the relatively flat Willamette Valley (SLE in Fig. 2.1) and Little Meadows, located over the windward slopes of the Cascades (LF in Fig. 2.1), depicts the intensity of precipitation events, which occurred over the 28 days of the field project (Fig. 2.2).

Two especially noteworthy days with heavy precipitation amounts occurred on November 29th and December 14th. Precipitation on both these days was associated with the passage of intense baroclinic zones and strong prefrontal west-southwesterly flow. As this flow ascended the higher terrain of the Cascades, a significant enhancement in the precip-

itation amounts was seen at Little Meadows compared to Salem. In fact over the entire time period of the IMPROVE-2 study, Little Meadows consistently received significantly higher precipitation amounts than Salem, exemplifying how orographic lifting can enhance precipitation totals over relatively small distances.

The major storm, which crossed over the IMPROVE study area on 13-14 December 2001 was ideally suited for the thesis goals outlined in Chapter 1. The storm was characterized by the passage of a forward-tilted baroclinic zone and associated area of heavy stratiform precipitation. The large stratiform precipitation shield and steady-state nature of the prefrontal flow provided an ideal environment for examining how frontal precipitation interacts with terrain. The majority of the observational platforms were successfully operating (including in the Convair microphysical measurements, airborne dual-Doppler radar, S-Pol radar, profilers, and soundings) allowing a detailed analysis of the event.

2.3   Description of Mesoscale Model

The PSU-NCAR Mesoscale Model (MM5) version 3.5, was employed in non-hydrostatic mode to simulate the 13-14 December 2001 system. A 36-km outer domain with a 12-km nest was run for 36 hours to capture the large-scale synoptic features of the storm. The domains covered a large area of the eastern Pacific and Pacific Northwest (Fig. 2.3). The model was initialized on 0000 UTC 13 December 2001 by interpolating a modified National Center for Environmental Prediction (NCEP) Aviation Model (AVN[1]) initialization for 0000 UTC 13 December 2001 to the MM5 grid. The 0000 UTC 13 December AVN grid was improved by incorporating surface and upper-air observations using a Cressman-type analysis scheme (Benjamin and Seaman, 1985). Additional analyses were generated every six hours using similarly modified gridded AVN forecasts and then linearly interpolating in time to provide continuous lateral boundary conditions for the 36-km domain.

To ensure the most accurate simulation, four-dimension data assimilation (FDDA) was

---

[1]The AVN is currently known as the Global Forecast System Model (GFS).
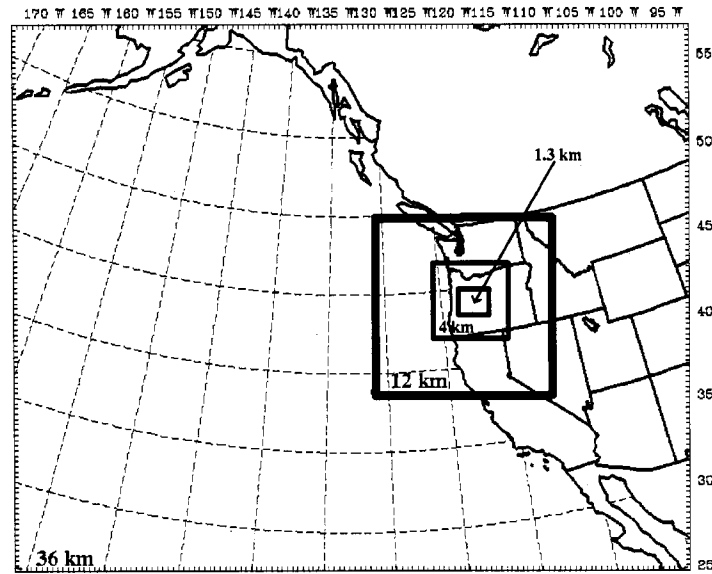
Figure 2.3: The 36 km, 12 km, 4 km, and 1.33 km MM5 domains used in this study.

employed during the first 12-hours of the forecast. The FDDA scheme (Stauffer and Seaman, 1990; Stauffer et al., 1991) applied a Newtonian relaxation technique to nudge the model's wind, temperature, and moisture fields towards modified AVN surface and upper-air grids at 0600 UTC and 1200 UTC 13 December 2001. Thirty-two unevenly spaced full-sigma levels were used in the vertical, with maximum resolution in the boundary layer. The simulation used the updated (version 3.6) explicit moisture scheme of Reisner 2 (Thompson et al., 2004), Grell cumulus parameterization (Grell, 1993) and the MRF planetary boundary layer scheme (Hong and Pan, 1996).

In addition to the 36 and 12 km domains, a separate 4-km simulation with a 1.33-km nest centered over the central Oregon Cascades was run for 30 hours initialized at 0600 UTC 13 December 2001. The 4-km grid was initialized by linearly interpolating forecasts from the 12-km MM5 simulation. The dimensions and terrain of the 4 and 1.33 km simulations are shown in Fig. 2.3. These inner domains did not use nudging or cumulus parameterizations.

Chapter 3

SYNOPTIC EVOLUTION

This chapter describes the large-scale synoptic evolution of the major precipitation event, which affected the IMPROVE-2 study area on 13-14 December 2001. The MM5 was used to simulate the storm and will be extensively verified against the wealth of observational assets available, including radiosondes, radar data, and surface observations. The verification is necessary in order to isolate errors in the microphysics from problems with the simulated synoptic-scale fields.

3.1 Upper Level and Surface Fields

At 1200 UTC 13 December 2001, prior to the arrival of precipitation over the IMPROVE-2 domain, a 300-hPa jet streak with winds over 150 knots was positioned over the eastern Pacific along $45°$ N and south of a 500-hPa short wave trough (Figure 3.1a). At 850 hPa a weak short-wave ridge was evident over the Oregon Coast with a trough located to the west (Figure 3.1c). The NCEP surface analysis (Figure 3.1e) showed a 988-hPa surface low near the Queen Charlotte Islands with an associated occluded front extending southward to a triple point at $48°$ N $133°$ W. Infrared satellite images at 1200 UTC 13 December 2001 (Figure 3.2a) indicated a large area of clouds extending southwestward offshore of the Pacific Northwest coast.

The 12-h model forecasts for 1200 UTC 13 December 2001 over the 36-km domain are shown in Fig. 3.1b,d,f. The model was able to accurately capture the location and intensity of the jet-streak and its position south of the 500-hPa short wave (Fig. 3.1b). At the 850-hPa level (Fig. 3.1d), the model correctly portrayed the short-wave ridge over the coast with prevailing southwest flow and weak warm air advection. Sea level pressure was also

well simulated, with a 996-hPa contour located in the observed position as was the trough axis extending to the southwest (Fig. 3.1f).

Model 24-h upper level forecasts and the corresponding NCEP analyses for 0000 UTC 14 December 2001 are shown in Fig. 3.3. The 500-hPa trough had amplified considerably since 1200 UTC 13 December 2001 and was positioned just offshore of the West Coast (Fig. 3.3a). The 850-hPa map for 0000 UTC December 14, 2001 (Fig. 3.3c) shows the lowest heights over Vancouver Island, collocated with the minimum in sea level pressure (Fig. 3.3e). A trough with strong 850-hPa height gradients had replaced the short-wave ridge over Oregon with a wind of 70 knots (35 m s^{-1}) at Salem, Oregon. The simulated height fields at these levels (Fig. 3.3b and 3.3d) indicated that the model accurately portrayed these upper-level features.

The NCEP surface analysis for 0000 UTC 14 December 2001 shows the front had continued to occlude and extended south from a 984-hPa surface low pressure center over central Vancouver Island to just offshore of the Oregon coast (Fig. 3.3e). Infrared imagery for 0000 UTC 14 December 2001 (Fig. 3.2b) shows a large area of high clouds over the Pacific Northwest with a distinct back edge coinciding with the position of the surface front. The 24-h forecast sea level pressure field (Fig. 3.3f) related well to the observed surface analysis at this time, with a 983-hPa low pressure center over northwest Washington, slightly south of the observed position. The model-predicted surface fields also indicated the presence of a temperature gradient and wind shift extending southwest of the simulated low pressure center.

By 1200 UTC 14 December 2001, the NCEP upper-level analysis showed the 500-hPa trough had continued to amplify and was now centered over the study area (Fig. 3.4a). The 300-hPa jet streak lay to the west of the 500-hPa trough axis, with the leading edge of the higher winds reaching the northern California coast. At the 850-hPa level, the trough had moved eastward to Idaho (Fig. 3.4c). The surface front had passed through Oregon, high pressure was building offshore, and the surface low had continued to deepen, with the 982-hPa closed contour located north of Idaho (Fig. 3.4e). Infrared satellite images (Fig. 3.2c)
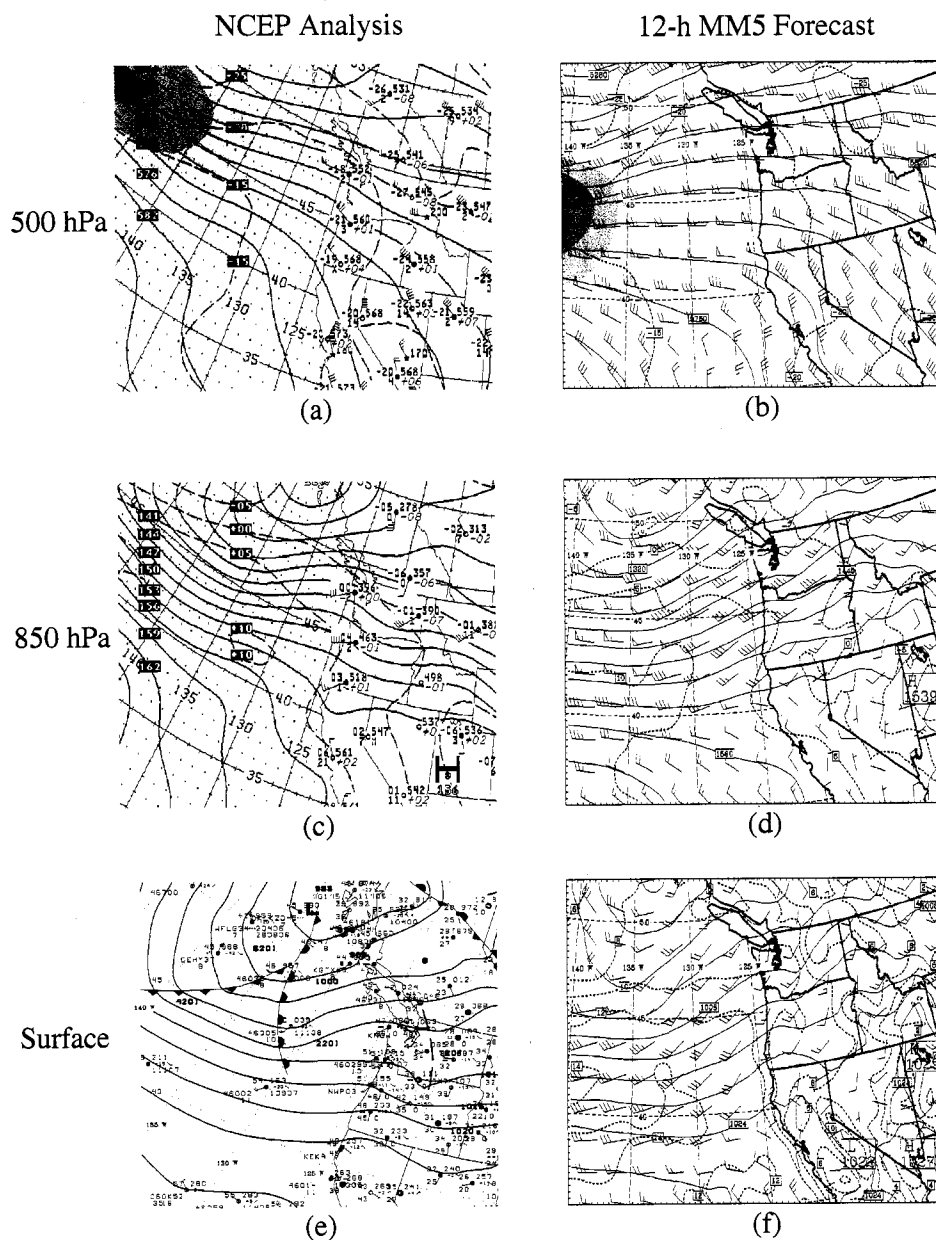
Figure 3.1: (a) NCEP 500-hPa analysis with 300-hPa winds greater than 110 knots shaded at intervals of 20 knots, (b) MM5 500-hPa 12-h forecast with 300-hPa winds shaded every 20 knots, (c) NCEP 850-hPa analysis, (d) MM5 850-hPa 12-h forecast, (e) NCEP sea level pressure analysis, and (f) MM5 12-h forecast of sea level pressure. All for 1200 UTC 13 December 2001.
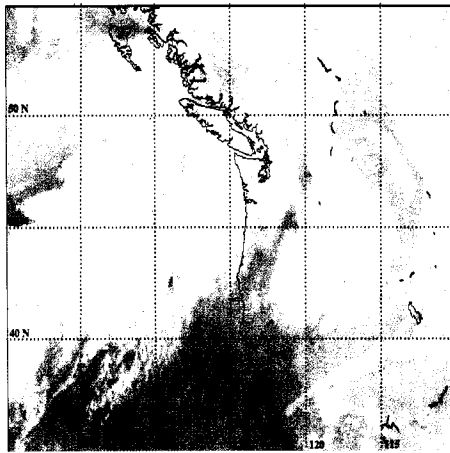
(a)
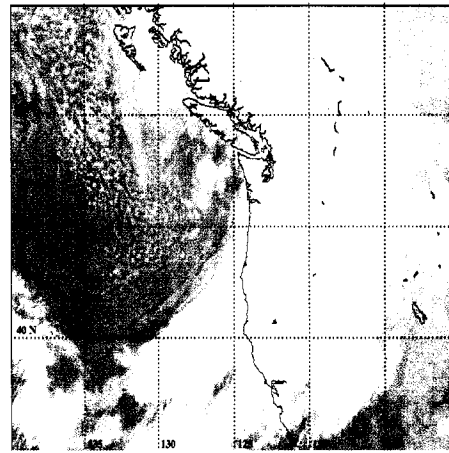
(b)
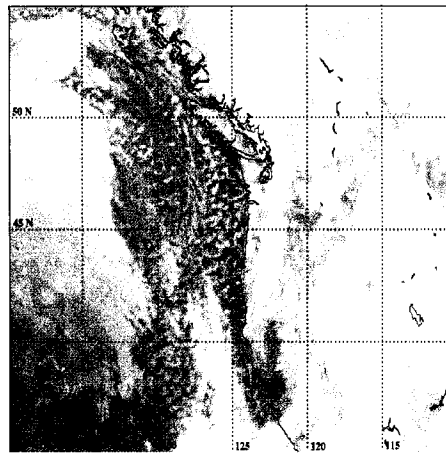
(c)

Figure 3.2: GOES 4-km infrared satellite images over the Pacific Northwest for (a) 1200 UTC 13 December 2001, (b) 0000 UTC 14 December 2001, and (c) 1200 UTC 14 December 2001.

17

NCEP Analysis   24-h MM5 Forecast

500 hPa

(a)   (b)

850 hPa

(c)   (d)

Surface

(e)   (f)
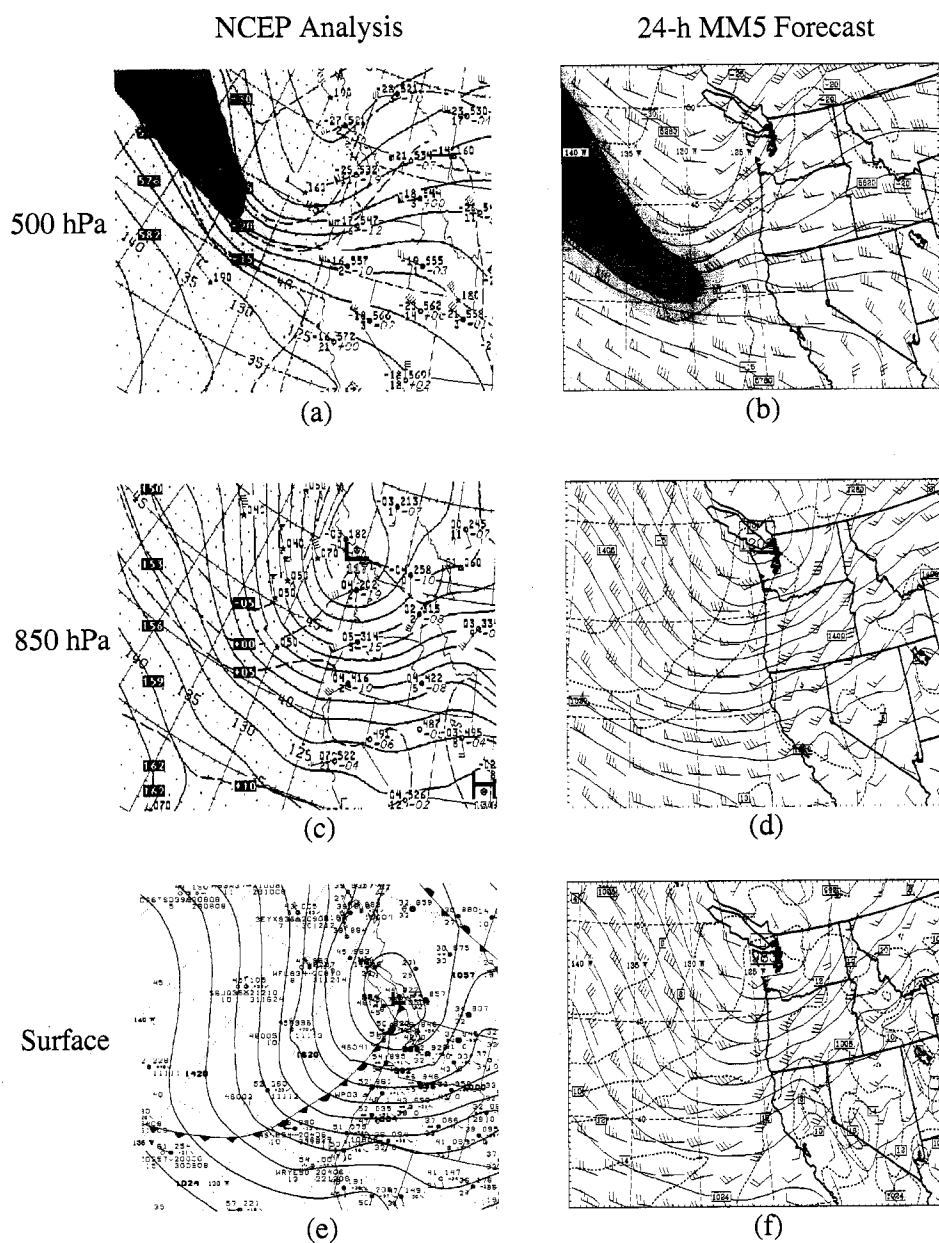
Figure 3.3: (a) NCEP 500-hPa analysis with 300-hPa winds greater than 110 knots shaded at intervals of 20 knots, (b) MM5 24-h 500-hPa forecast with 300-hPa winds shaded every 20 knots, (c) NCEP 850-hPa analysis, (d) MM5 24-h 850-hPa forecast, (e) NCEP sea level pressure analysis, and (f) MM5 24-h forecast of sea level pressure. All for 0000 UTC 14 December 2001.

18

500 hPa

(a)   (b)

850 hPa

(c)   (d)

Surface

(e)   (f)
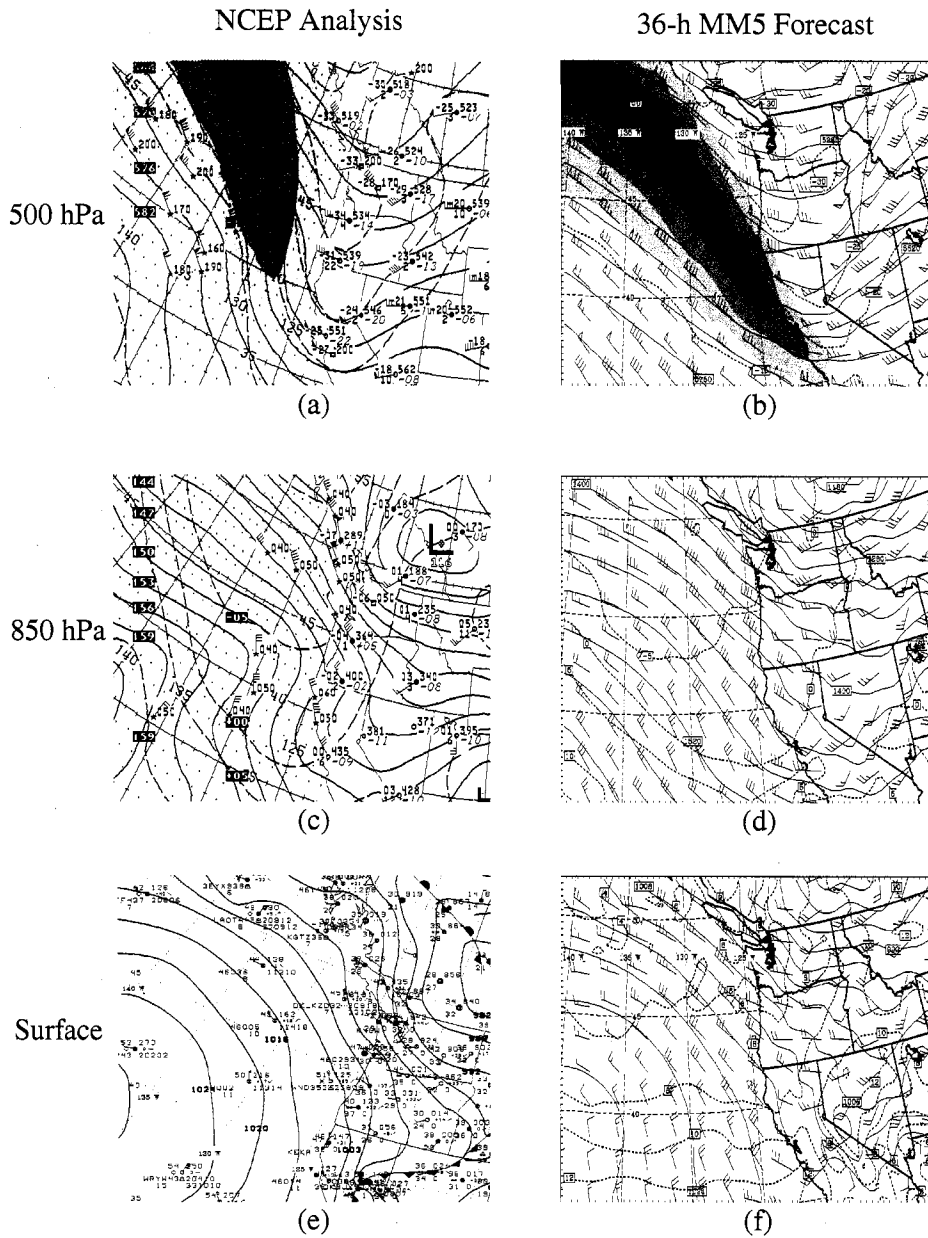
Figure 3.4: (a) NCEP 500-hPa analysis with 300-hPa winds greater than 110 knots shaded at intervals of 20 knots, (b) MM5 500-hPa 36-h forecast with 300-hPa winds shaded every 20 knots, (c) NCEP 850-hPa analysis, (d) MM5 850-hPa 36-h forecast, (e) NCEP sea level pressure analysis, and (f) MM5 36-h forecast of sea level pressure. All for 1200 UTC 14 December 2001.

indicated the colder clouds were well east of the study area, with residual low-level clouds along the Cascades and coastal mountains. The model's 36-h forecast for 1200 UTC 14 December 2001 shows upper level (Fig. 3.4 b,d) and surface (Fig. 3.4f) features consistent with observations, with the exception of the model's predicted jet-streak at 300 hPa having progressed farther south and east than analyzed.

3.2 Frontal Structure

To determine the vertical structure of the baroclinic zone as it crossed the area, a time-height cross section of potential temperature (θ) from 1200 UTC 13 December 2001 through 1200 UTC 14 December 2001 was constructed (Fig. 3.5a) using six consecutive soundings taken at Salem, OR. Prior to 2200 UTC 13 December 2001, warm advection was occurring at all levels as suggested by the veering of wind direction with height. At approximately 2200 UTC 13 December 2001, the leading edge of a strong baroclinic zone, depicted by a solid gray line, crossed Salem between 650-700 hPa. The front was tilted forward from the surface to approximately 650 hPa, and tilted backward with height above.

Coincident with and immediately preceding the passage of the mid-level front, there was an area of strong southwest winds reaching approximately 40 m s^{-1} (shaded region in Fig. 3.5a). Following the front, the winds weakened and veered to westerly. The θ gradient was strongest between 400 and 700 hPa, with θ decreasing by 10K in eight hours at 650 hPa. The passage of the baroclinic zone aloft and associated cold air advection were reflected at the surface by a decrease in the rate of the sea level pressure fall (see in Fig. 5 of Woods et al. 2005). The forward-tilted structure of the θ gradient is similar to the type of split cold front described in Browning and Roberts (1996). These types of fronts have been observed in the Pacific Northwest previously, as discussed in Locatelli et al. (2005).

A corresponding model-derived time-height cross section of θ is shown in Fig. 3.5b. The model resolved the frontal structure of the baroclinic zone with the gradient in θ sloping forward with height from the surface. The leading edge of the baroclinic zone at 650 hPa was simulated to cross Salem at 2200 UTC 13 December 2001, which compared well
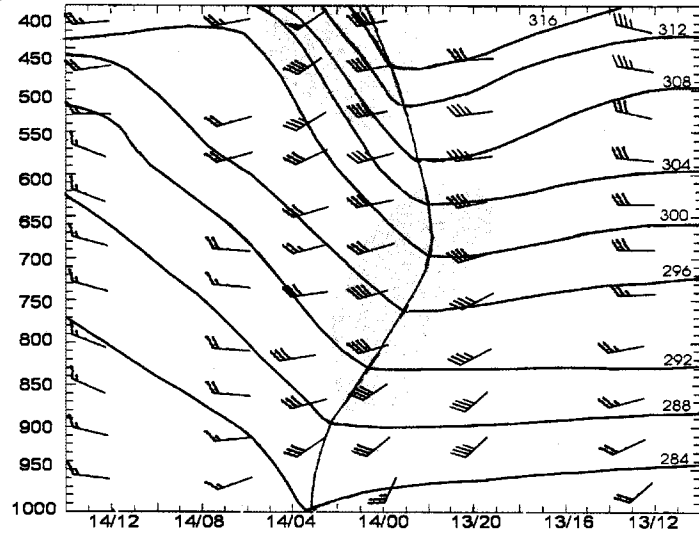
(a)
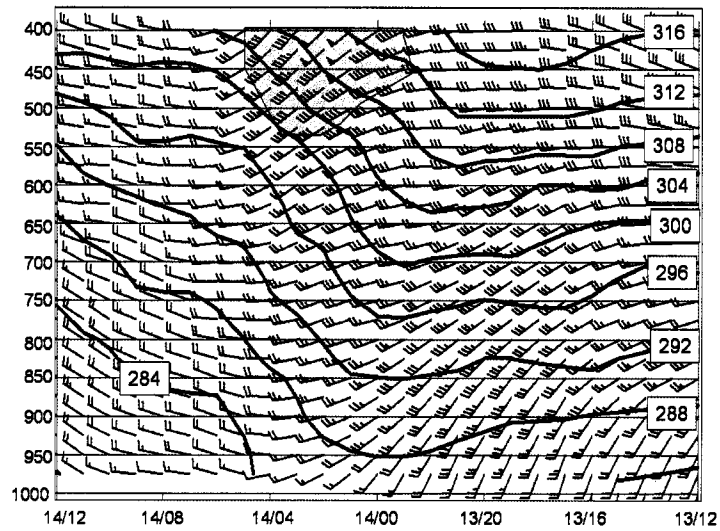
(b)

Figure 3.5: Time-pressure cross sections for the time period from 1200 UTC 13 December to 1200 UTC 14 December at Salem (SLE), Oregon. Solid lines are contours of potential temperature every 4 °K. Time increases from right to left on the x-axis. The observed front is represented by a solid gray line. Wind barbs in m s^{-1} with the shaded region indicating wind speeds exceeding 40 m s^{-1}. (a) Observed and (b) 1.33-km MM5 forecast

with observations. The gradient in θ was also well simulated, decreasing by 10K in eight hours at 650 hPa. The model was not able to capture the 40 m s^{-1} winds associated with the baroclinic zone between 700 and 850 hPa, being weaker by approximately 10 m s^{-1} over a two hour period encompassing frontal passage. Outside of this area, the model accurately portrayed the observed wind speeds to within 5 m s^{-1}. Above 650 hPa the model's baroclinic zone did not tilt backwards with height as observed. Similar to observations, model wind speeds increased to 40 m s^{-1} in the layer above 500 hPa.

Special soundings (location indicated by the UW on Fig. 2.1) provided measurements of the environment upstream of the elevated topography of the study area. Figure 3.6a presents a profile from a sounding taken at 2100 UTC 13 December 2001, just before the mid-level frontal passage. The observed sounding indicated veering of winds between 1000-600 hPa, with a wind speed of 40 m s^{-1} in a layer between 700-650 hPa. A saturated layer was present between 900-550 hPa and the freezing level was at approximately 780 hPa, or slightly above 2 km MSL. The model sounding for 2100 UTC 13 December (Fig. 3.6b) verified well, depicting a saturated stable layer between 900 and 550 hPa with the freezing level at approximately 790 hPa.

Three hours later at 0000 UTC 14 December 2001, the UW sounding (Fig. 3.6c) showed cooling of 3-7 °C between 700-450 hPa, signaling the passage of the frontal feature at mid-levels. Above and below this level the temperature remained nearly constant. Winds veered between 800-1000 hPa indicating warm air advection at lower levels. The model sounding for 0000 UTC 14 December 2001 (Fig. 3.6d) captured the amplitude and location of the cooling between 700 and 400 hPa behind the baroclinic zone at mid-levels. As previously noted, the model failed to resolve the stronger 40 m s^{-1} winds at around 750 hPa. Instead model winds were 10-15 m s^{-1} lower than observed at this level. The model profile was saturated with respect to water between 900-400 hPa. This was different from observations, which only had a layer saturated with respect to water between 900-650 hPa and was close to saturation between 650-400 hPa. The differences between the model and observed dewpoint temperatures between 650-400 hPa are within with the expected

22
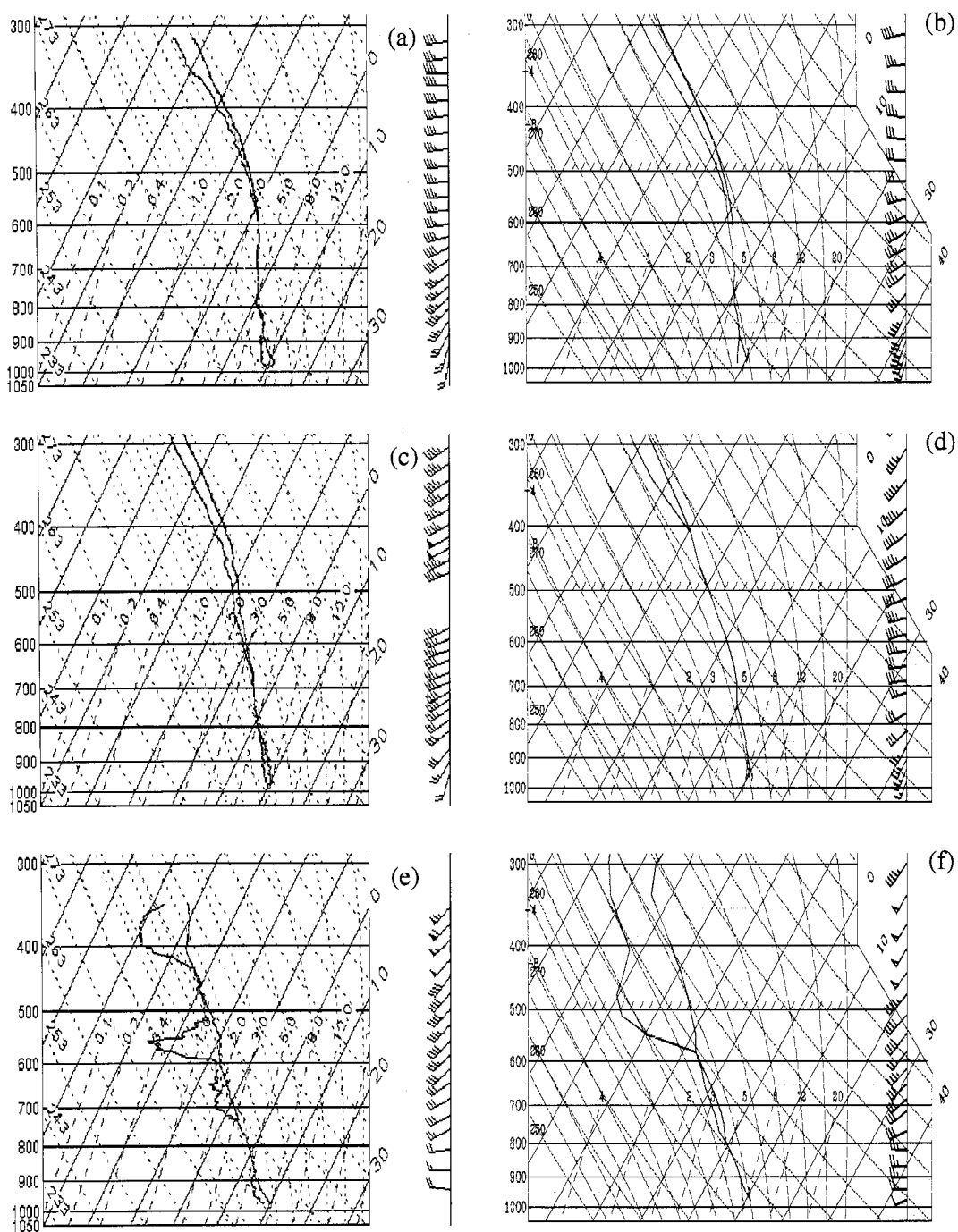
Figure 3.6: (a) 2100 UTC 13 December 2001, (b) 15-h 1.33-km MM5 forecast, (c) 0000 UTC 14 December 2001 (d) 18-h 1.33-km MM5 forecast (e) 0400 UTC 14 December 2001, and (f) 22-h 1.33-km MM5 forecast profiles from the UW sounding site.

error bounds of the sounding measurements, which are known to have a dry-bias at low temperatures (Wang et al., 2003). Overall the upstream moisture profiles during this period are well represented in the model.

After passage of the surface front, cold air advection occurred at all levels. The UW special sounding at 0400 UTC 14 December 2001 (Fig. 3.6d) indicated a decrease in temperature between 1000 and 400 hPa with the freezing level dropping to approximately 820 hPa or 1.8 km during the four hours starting at 0000 UTC 14 December 2001. The 0400 UTC sounding indicated that the model correctly simulated the magnitude of the cold air advection (Fig. 3.6e) and the drop of the freezing level behind the front. The moisture field was well depicted with the exception of a layer between 425-500 hPa where the model's dewpoint was much lower than observed.

3.3 Radar Verification

Associated with the passage of the upper-level baroclinic zone was a large elongated area of moderate to heavy stratiform precipitation that was oriented southwest-northeast. The Portland WSR-88D radar (located north of the study area) shows the expansive area of stratiform precipitation spreading over the study area from the northwest at 1830 UTC 13 December 2001 (Fig. 3.7a). Prefrontal showers were present ahead of this stratiform precipitation shield. After passage of the stratiform precipitation band, there was a distinct break in the precipitation as shown Fig. 3.7b. The transition from widespread radar echos to areas of more sporadic reflectivities was associated with an area of subsidence and drying aloft coinciding with the passage of the mid-level baroclinic zone in the layer between 600-400 hPa (Fig. 3.5a).

The surface front passed Salem, OR at approximately 0300 UTC 14 December 2001, almost 5 hours after mid-level frontal passage. A narrow band of high reflectivity (> 30 dBZ) crossed Portland (PDX) at 0130 UTC 14 December 2001 (Fig. 3.7b), accompanying passage of the surface front. This precipitation band was more convective and shallower than the preceding stratiform precipitation shield. After passage of the surface frontal band,
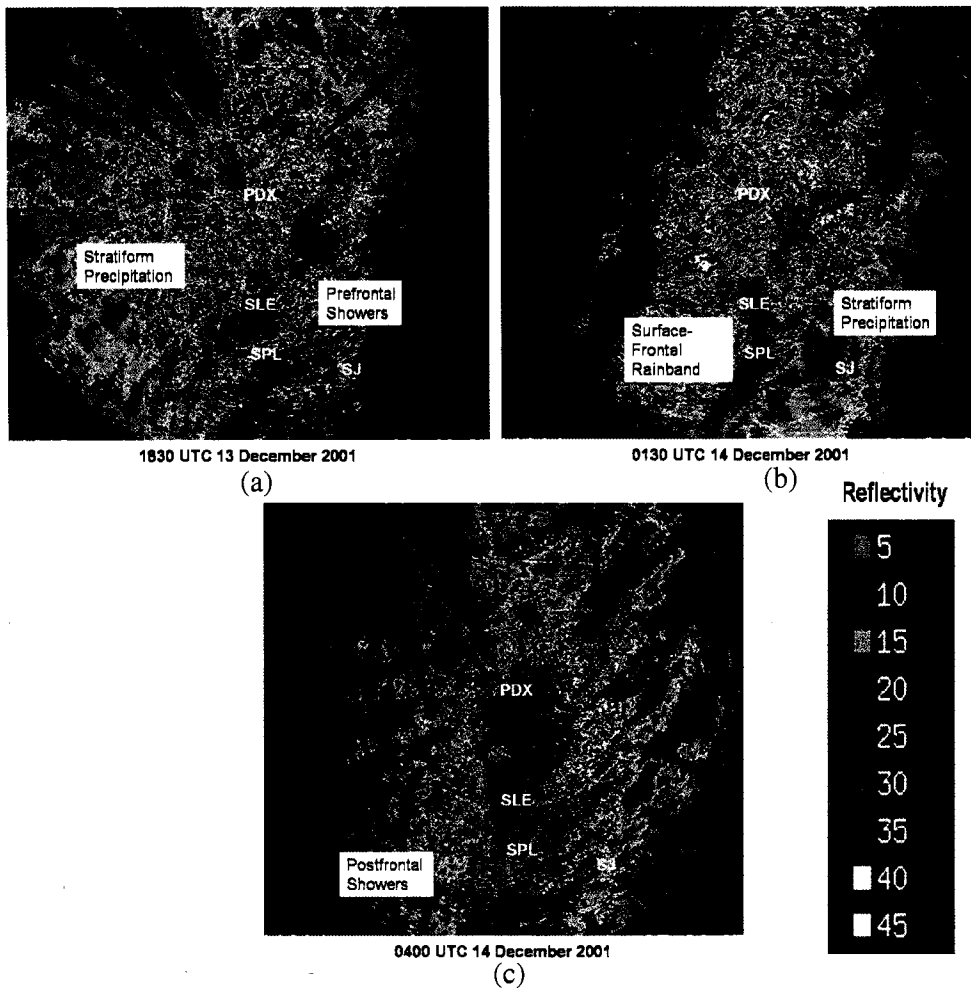
Figure 3.7: Reflectivities from the Portland (PDX) WSR-88D radar at an elevation angle of 0.5 degrees at (a) 1830 UTC 13 December 2001, (b) 0130 UTC and (c) 0400 UTC 14 December 2001.The positions of Salem, Oregon (SLE), the S-Pol site (SPL), and Santiam Junction (SJ) are also identified.

the precipitation became more sporadic and showery in the post-frontal air mass (Fig. 3.7c).

Figure 3.8a shows reflectivity from the NCAR S-Pol radar (located at SPL in Fig. 1b) for a 1.5 degree elevation angle at 1921 UTC 13 December 2001. The transition from

prefrontal showers to stratiform precipitation was evident, with the leading edge of the heavier precipitation (greater than 17 dBZ) just west of the S-Pol site. Figure 3.8b is a depiction of a model-based reflectivity at 700 hPa for 1900 UTC 13 December 2001 (13-h forecast). The 700 hPa level is approximately the mean elevation of the S-Pol 1.5 degree radar scan displayed in Fig. 3.8a. The model reflectivity values were computed using an algorithm relating effective reflectivity to the assumed precipitation number distribution of the model (Fovell and Ogura, 1988). The algorithm uses the updated intercept parameters for snow and graupel (Thompson et al., 2004) from the model BMP.

The timing and orientation of the modeled precipitation (Fig. 3.8b) was similar to the observed patterns but did not show the change in character from prefrontal showers to steady stratiform precipitation. To the east, lower reflectivity values were present over the crest of the Cascades, with no precipitation evident in the lee. At 0042 UTC 14 December radar images indicated a back edge to the organized precipitation band with the highest dBZ values to the east of the S-Pol site (Fig. 3.8c). To the west of the precipitation band, dBZ values were smaller and echoes less widespread. The model reflectivity at 0045 UTC 14 December 2001 (Fig. 3.8d) was consistent with observations, depicting the most intense dBZ values to the east of the S-Pol site.

Although the model indicated a surface pressure rise and wind shift over the Willamette Valley with the passage of the surface front, it did not produce an organized band of precipitation as observed (Fig. 3.9a). Instead, the model produced scattered areas of higher dBZ values over the coast and the Willamette Valley with an enhancement of the echos over the Cascades (Fig. 3.9b). After frontal passage the precipitation was less organized, with the presence of a more convective and showery regime at 0600 UTC 14 December 2001 (Fig. 3.9c). The model also simulated a change to a shallow convective regime (Fig. 3.9d).

3.4 Summary and Conclusions

This chapter describes the synoptic evolution of a major precipitation event, which affected the IMPROVE-2 study area on 13-14 December 2001. The Fifth Generation Penn State

(a)   (b)

(c)   (d)
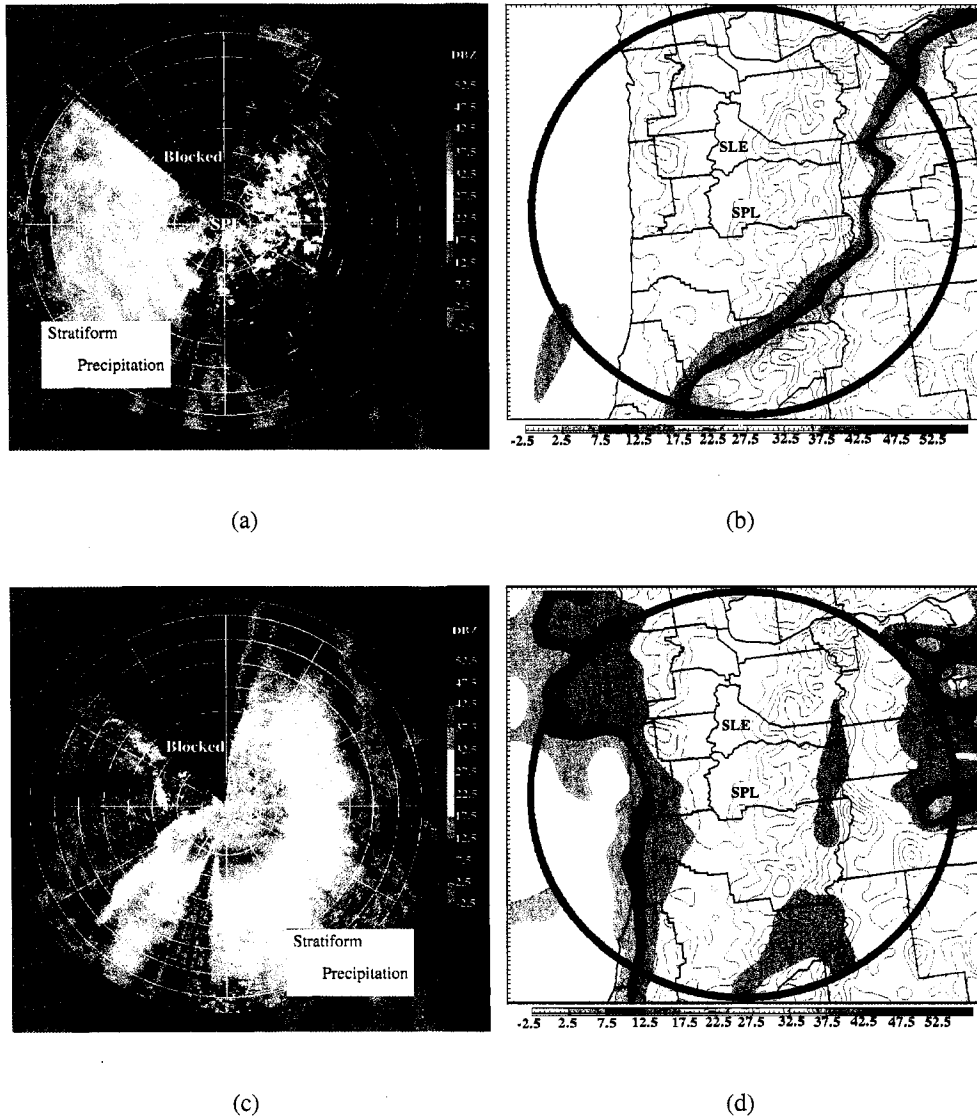
Figure 3.8: Reflectivity patterns at an elevation angle of 1.5 degrees from the NCAR S-Pol radar for (a) 1921 UTC 13 December 2001 and (c) 0042 UTC 14 December 2001. Circles at a 20 km interval away from S-Pol site are shown with; the outer circle is at 180 km. Model-depicted radar reflectivity at 700 hPa from the 4-km MM5 simulation at (b) 1900 UTC 13 December 2001 (13-h forecast), and (d) 0045 UTC 14 December 2001 (18.75-h forecast). The black circle is 180 km from the SPL site.

(a)

(b)

(c)

(d)
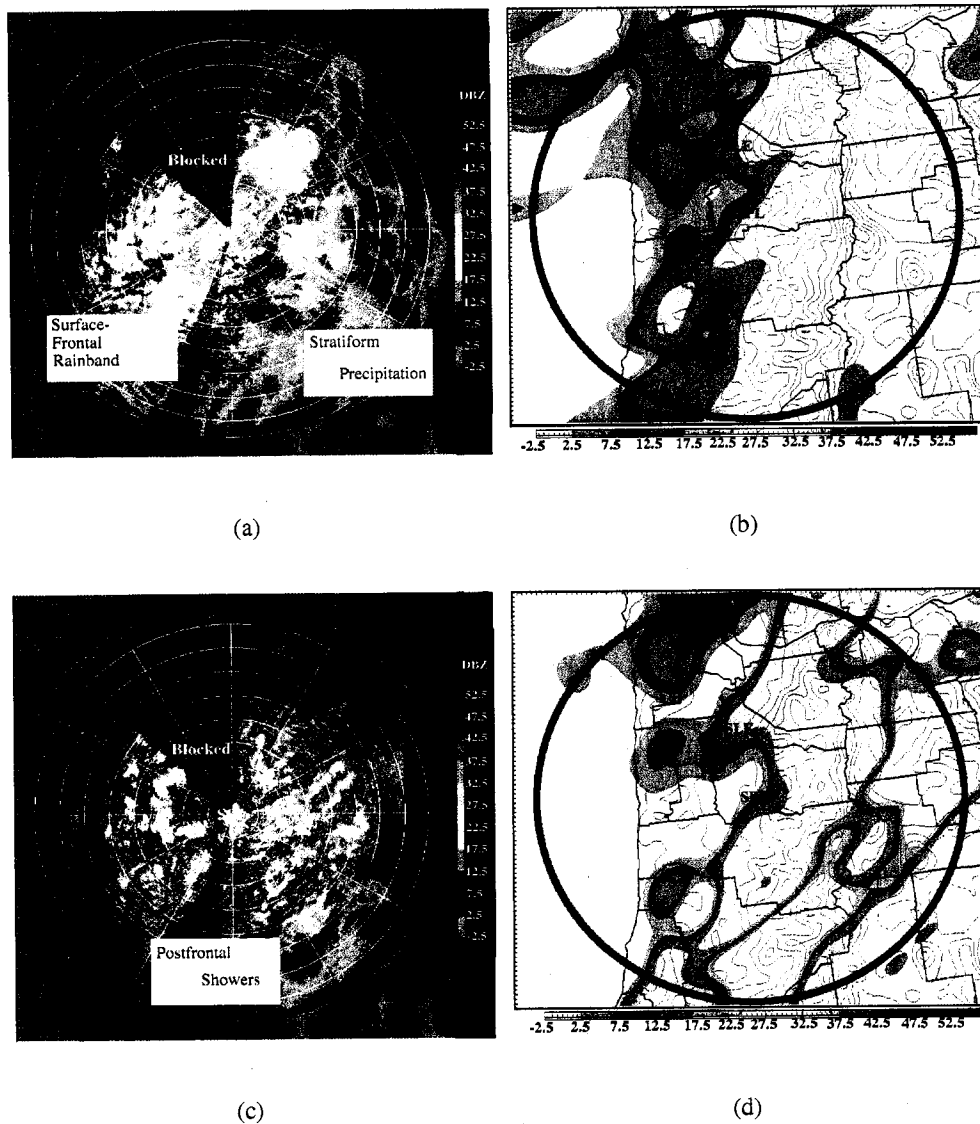
Figure 3.9: Reflectivity patterns at an elevation angle of 1.5 degrees from the NCAR S-Pol radar for (a) 0300 UTC and (c) 0523 UTC 14 December 2001. Circles at a 20 km interval away from S-Pol site are shown with outer circle at 180 km. Model-depicted radar reflectivity at 700 hPa from the 4-km MM5 simulation at (b) 0300 UTC (21-h forecast) and (d) 0500 UTC 14 December 2001 (23-h forecast). The black circle is 180 km from the SPL site.

/ NCAR Mesoscale Model (MM5) was utilized to simulate the system and run at various resolutions to evaluate the model's ability to simulate the synoptic and mesoscale features associated with the storm. Extensive model verification was performed utilizing the wealth of observational assets available during the field project, including upper air radiosonde measurements, radar data, and surface observations.

The 13-14 December 2001 event featured the passage of a strong forward-tilting frontal system. The front extended southward from an intensifying surface low that deepened to 984 hPa as it passed north of the study area. The MM5 was able to represent accurately the synoptic-scale features associated with the storm system, including the rapid intensification of the surface low, amplification of the 500-hPa trough, and the position and strength of the 300-hPa jet-streak.

Ahead of the front, winds over the study area were from the southwest and warm advection was occurring at all levels. The front tilted forward with height to 650 hPa above, which it tilted backward. Wind speeds approached 40 m s^{-1} concurrent with and immediately preceding the passage of the front between 650 and 850 hPa. After the front, θ rapidly decreased and winds backed with height. The model was shown to accurately depict the tipped-forward structure of the front as well as the strength of the associated baroclinic zone. Despite the accurate portrayal of the frontal structure, modeled winds were 5-10 m s^{-1} too weak preceding the mid-level baroclinic zone between 850 and 650 hPa for a three-hour period. A comparison of soundings indicate the upstream moisture profile was well represented in the model.

Radar analysis indicated a broad area of precipitation extending well ahead of the middle-level front. After frontal passage aloft, a distinct back edge to the precipitation shield was observed. The model was able to represent accurately the orientation and timing of the precipitation band and subsequent subsidence. Radar analysis also indicated the presence of a well-defined convective precipitation band associated with the surface front. The model was able to capture the presence of a surface baroclinic feature, but did not simulate the precipitation band associated with it.

The performance of the model in simulating the synoptic features associated with the 13-14 December 2001 storm system was sufficiently accurate to permit future comparisons of mesoscale and microphysical data with the model. Errors in the model simulation regarding the speed of the low-level jet and slope of the front above 650 hPa though must be taken into account when performing the verification.

Chapter 4

MESOSCALE FEATURES

This chapter will utilize P-3 in situ measurements and a comprehensive airborne dual-Doppler dataset to examine mesoscale features associated with the 13-14 December 2001 event. Specifically, the amplitude and strength of mountain waves over both the windward and lee slopes of the central Oregon Cascades will be explored from a fully three-dimensional perspective. The MM5 simulation will be evaluated alongside the observations and then employed to examine the evolution of these stationary waves. Ground-based radar, soundings, and wind profiler measurements will also be used to evaluate the model's performance. Model sensitivity studies will assist in analyzing the complex interaction between the upstream flow field and the mountain wave over the crest.

4.1 Upstream Conditions

4.1.1 Synoptic Overview

Chapter 3 presented a detailed account of the evolution of the synoptic fields for the duration of 13-14 December 2001 storm system, with the evolution validated against the MM5 simulation. Although this mesoscale analysis will predominately focus on a two-hour period from 2300 UTC 13 December through 0100 UTC 14 December, when precipitation over the study area was heaviest, a brief overview of the kinematic and thermodynamic evolution of the storm provides a context for the mesoscale features described in the subsequent sections.

At 2000 UTC 13 December 2001, a large area of high potential temperature (θ), was located offshore of the West Coast at heights of 1 and 3 km (Fig. 4.1a,b). East of the high θ region, lay a weak gradient in θ, with values over western Oregon being 3-4 K lower

than those offshore. Coincident with this gradient was a transition in wind direction from westerly offshore to more south-southwesterly near the coast. A second stronger gradient in θ was evident entering the domain from the northwest, and was associated with the forward-tilted cold front as described in Chapter 3.

An 800-km long E-W cross section (location shown in Fig. 4.1) was constructed to illustrate the vertical structure and evolution of the large-scale thermodynamic and kinematic fields (Fig. 4.2). The cross section showed that at 2000 UTC, a cold front (position indicated by dashed gray line) was well offshore (Fig. 4.2a). West of the front, the contours of θ were negatively sloped and cold advection was occurring. To the east of the front, a relatively broad and uniform area of warm air advection was present, with a constant positive slope in the θ contours and veering of wind direction with height. There was no indication in this cross section of enhanced southerly flow below crest level over the windward slopes (barrier-parallel jet), as would be expected in a case of significant terrain-induced blocking. A mountain wave above and to the lee of the Cascade crest was also evident, with a sharp descent and subsequent downstream rebound of the θ contours persisting during the entire 6-h period displayed in Fig 4.2. Radar measurements at this time showed a large shield of stratiform precipitation over the study area (Fig. 3.8c).

Three hours later at 2300 UTC, the gradient in θ near the coast had intensified and progressed onshore with lower θ values and southwesterly flow persisting over the study area at 1-km (Fig. 4.1c). The leading edge of the cold advection had moved eastward but still was about 150-km west of the study area at 1-km and near the coast at 3-km (Fig. 4.1c,d). The E-W vertical cross section at this time (Fig. 4.2b) shows that east of the cold front the slope of the θ contours had increased significantly. Additionally, over the windward slopes of the Cascades, enhanced vertical gradients in θ (gray shading in Fig. 4.2b) and equivalent potential temperature (θ_e) were present between 2-and 4 km, extending upward with proximity to the crest. Substantial directional shear was present within this zone, with winds veering from southerly at low levels to a more westerly direction above the enhanced thermal (θ and θ_e) gradient.
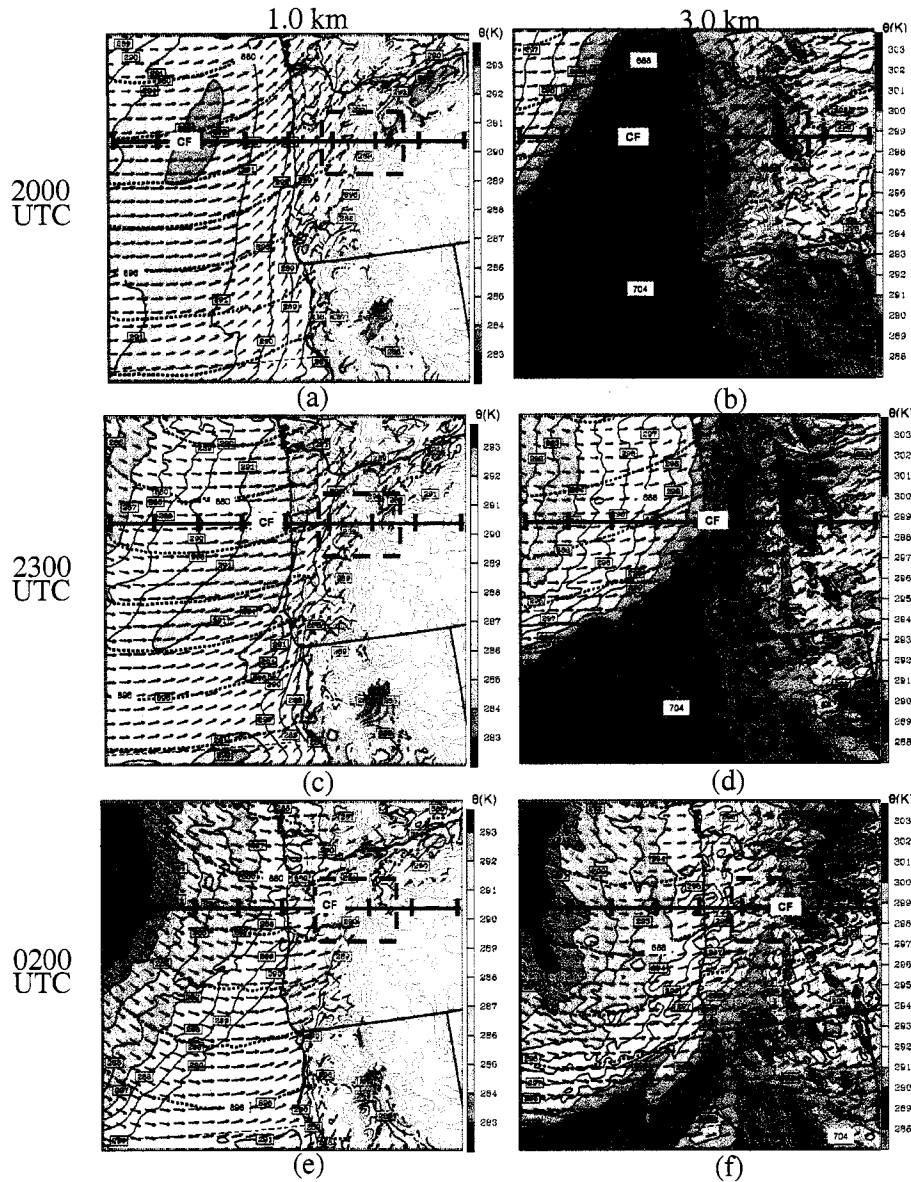
Figure 4.1: MM5 wind vectors (black arrows), potential temperature (color shaded), pressure (blue dashed contours), and topography (gray contours) from the 4-km domain simulation. Images are at heights of 1 km and 3 km MSL, respectively, at (a,b) 2000 UTC 13 December, (c,d) 2300 UTC 13 December and (e,f) 0200 UTC 14 December 2001. Blue dashed box represents the region where airborne P-3 dual-Doppler measurements were taken. Black line shows position of E-W cross-section in Fig. 4.2. The leading edge of the cold front along the cross-section is indicated by CF.
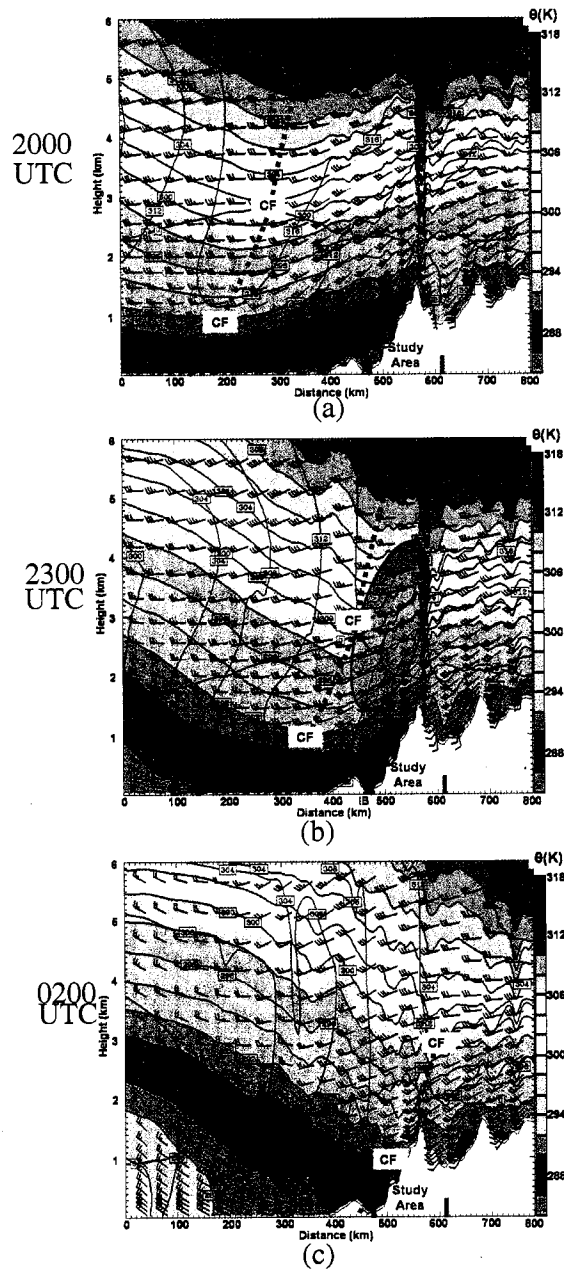
Figure 4.2: East-west cross section (position shown Fig 4.1) of MM5 4-km grid resolution simulated θ (colored shading), θ_e (solid blue lines) and wind barbs (in m s^{-1}) for (a) 2000 UTC 13 December, (b) 2300 UTC 13 December and (c) 0200 UTC 14 December 2001. Solid brown contour indicates 0^0C isotherm. Location of cold front given by gray dashed line with the shaded region in (b) showing a region of enhanced vertical gradients of θ and θ_e.

34
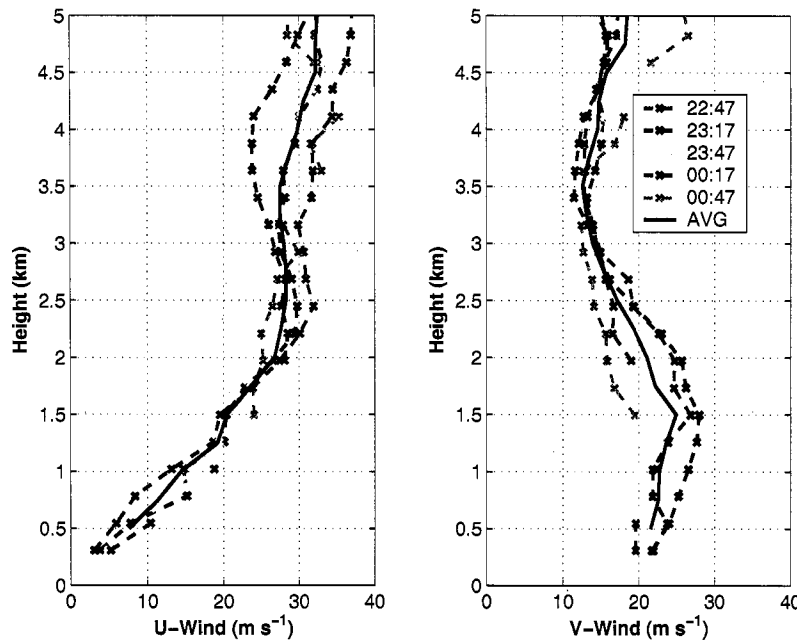
Figure 4.3: U and V-component winds from the NCAR Integrated Sounding System (ISS) profiler (located at IB in Fig. 2.1) at 30 minute intervals (dashed color lines) from 2247 to 0047 UTC 13-14 December 2001. The solid black lines represent the average of the five individual profiles.

Measurements of the observed upstream flow profile, provided by the NCAR Integrated Sounding System (ISS) profiler located at Irish Bend (IB in Fig. 2.1 and Fig. 4.2b), support the MM5's depiction of substantial veering of winds at low-levels during the prefrontal time period. Figure 4.3 displays profiles of U- and V-wind components at IB at 15-minute intervals from 2247 UTC 13 December through 0047 UTC 14 December 2001, as well as an average profile for the entire 2-hour period. Although there was some variance in the U- and V-components, these profiles remained relatively unchanged over the two-hour period. Consistent with the simulated veering at low-level winds, the U-component at IB increased from about 5 m s^{-1} near the surface to an average of 30 m s^{-1} at 2.5 km, while the V-component reached a maximum speed of $\sim$23 m s^{-1} at 1.5 km before reducing in strength aloft. Above 2.5 km both the U- and V- components were relatively uniform with

a modest 4-5 m s $^{-1}$ increase in the 2.5-5 km layer.

By 0200 UTC the cold front had entered the study area (Fig. 4.1e,f). The vertical cross section shows that winds throughout the lowest 6-km were from the west behind the front (Fig. 4.2c). Due to the modification of the θ and θ_e gradients by mountain waves over the Cascades, the position of the cold front at upper levels is difficult to ascertain.

4.1.2   Calculation of non-linearity parameter

The basic structure of mountain waves is determined by the size and shape of the underlying terrain and by the vertical profiles of temperature, cross-barrier speed, and moisture of the impinging flow. A special sounding (located at UW in Fig. 2.1) taken at 0000 UTC 14 December 2001 measured environmental conditions just upstream of the Cascade crest (Fig. 4.4). Although this sounding was likely somewhat modified by the barrier (Medina et al., 2005), it provides the best source of information on the thermodynamic structure directly upstream of the elevated terrain of the Cascades.

The U-component increased significantly from the surface to a height of 2.9-km, reaching peak speed of approximately 38 m s^{-1}. Above this strongly sheared layer, U was relatively uniform up to 4.5-km, above which it again began to increase with height. The MM5 1.33-km simulation essentially replicated this structure, but slightly over-predicted the strength of U within the shear layer below 2-km, while under-predicting the magnitude of U above.

The calculated dry Brunt-Väisälä frequency (N_d^2) from the sounding indicates the profile was stable throughout the lowest 6-km (Fig. 4.4). An additional calculation of the moist Brunt-Väisälä frequency (N_m^2) (Einaudi and Lalas, 1973; Durran and Klemp, 1982) was also performed, since the atmosphere was saturated below 600-hPa (Fig. 3.6c). The inclusion of moisture in the moist Brunt-Väisälä calculation accounts for the latent heat of condensation and thus provides a better indication of the stability of the upstream flow in a saturated environment (Durran and Klemp, 1982). Throughout most of the profile, N_m^2 remained weakly positive, indicating neutral to stable flow. A layer of increased stability near

U-Obs ——
U-MM5 ······

Height (km)

6

5

4

3

2

1

0

0   20   40
U-Wind (m s⁻¹)

6

5

4

3

2

1

0

0   2   4
N² (x10⁻⁴s⁻¹)

6

5

4

3

2

1

0

0   0.5   1   1.5
Nh/U

Moist ——
Moist-MM5 ······
Dry ——
Dry-MM5 ······
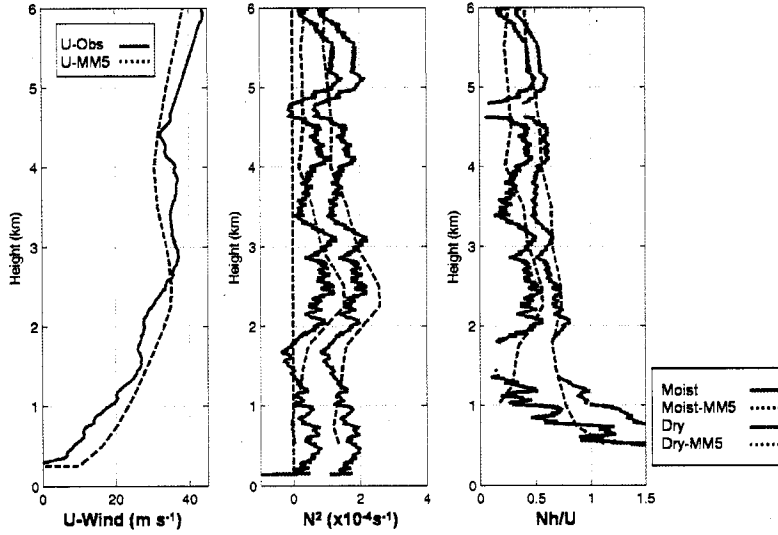
Figure 4.4: U-component speed, dry and moist squared Brunt-Väisälä Frequency (N_d^2, and N_m^2), and inverse Froude number (Nh/U) where h is the mean height of the Cascade crest (h=1.68km) from the special UW sounding location (UW in Fig. 2.1a) at 0000 UTC 14 December 2001 and the MM5 1.33-km simulation.

the top of the U-shear layer was present between 2 and 3 km, where the N^2 values peaked near $2 \times 10^{-1}s^{-2}$ (Fig 4.4). The 1.33-km MM5 simulation also reproduced the observed stratification, including the enhanced stability between 2-3 km.

Linear theory can be used to predict the character of mountain waves provided that the barrier height is small compared with the vertical wavelength of the resulting wave (Durran, 2003). The "non-linearity parameter" or inverse Froude number [Nh/U, where N is the dry or moist Brunt-Väisälä frequency, h is the average height of the mountain (assumed here to be 1.68 km) and U is the cross-barrier wind] was calculated for the sounding in Fig. 4.4. In the surface layer below 0.75 km where frictional effects are important, $N_m h/U$ was greater than unity while above this layer the non-linearity parameter profile was close to 0.5 for both moist and dry N^2 values. Theory predicts that a non-linearity parameter value of 0.5 is associated with a linear (i.e. "flow-over") mountain wave regime (Smith, 1989).

(a)   (b)
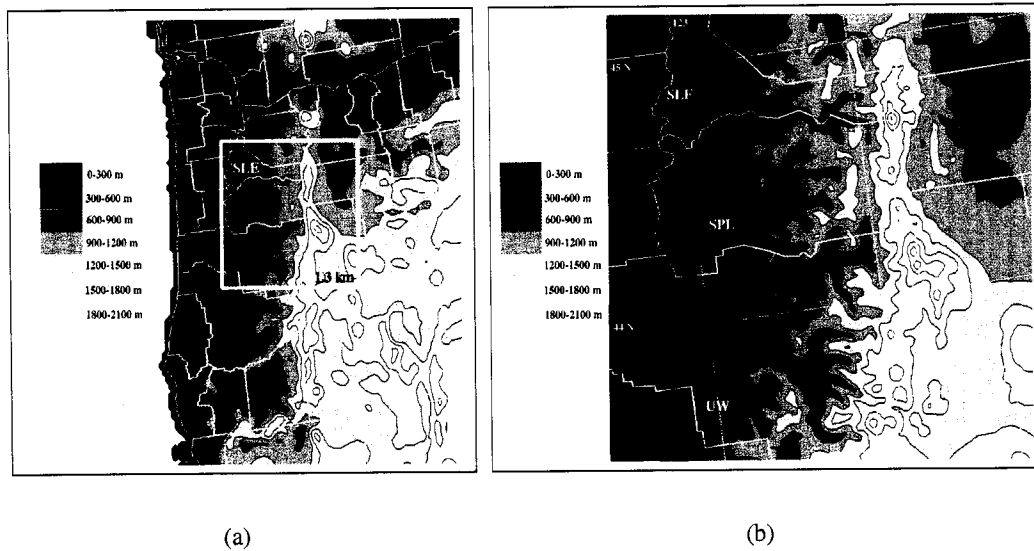
Figure 4.5: Terrain elevations (meters) for the (a) 4-km and (b) 1.33-km inner domains. The elevation is contoured every 300 m, decreasing in shade with height.

4.2 In situ Measurements

High-resolution 4-km and nested 1.33-km model grids were used to simulate the mesoscale structures associated with the 13-14 December 2001 storm system. The model topography was obtained by interpolating a 30-s topography data set to the grid using a Cressmen scheme and then filtering using a two pass smoother-desmoother. The 1.33-km domain's terrain (Fig. 4.5b) is substantially more complex than that of the 4-km domain (Fig. 4.5a), especially in resolving the windward ridges and valleys. The implications of the difference in terrain resolution are assessed below using in situ measurements from the P-3.

The NOAA P-3 performed five north-south legs from the Willamette Valley to the lee as seen in Fig. 2.1, permitting in situ sampling of thermodynamic and kinematic fields over a large portion of the study area. Vertical velocity was derived using in situ measurements from the P-3. First, the acceleration of the aircraft was computed from the inertial navigation system and integrated in time to derive the vertical speed of the aircraft. Then the
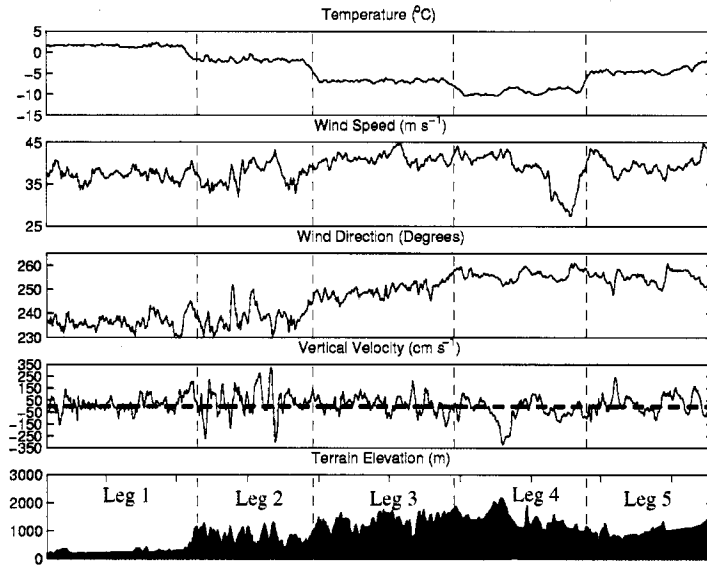
Figure 4.6: P-3 in situ meteorological variables from 2302 UTC 13 December 2001 through 0100 UTC 14 December 2001. Last panel is underlying elevation of terrain. Vertical dashed lines delineate the different N-S legs flown.

vertical wind relative to the aircraft was estimated from an array of static pressure sensors at various points on the air frame. The addition of the vertical speed of the aircraft and the relative vertical wind yielded an estimate of atmospheric vertical velocity. Errors in the vertical velocity are estimated to be roughly 30-50 cm s^{-1} (Bond, 2003).

Figure 4.6 shows a time series of four in situ meteorological variables measured by the P-3 during the five legs from 2302 UTC 13 December through 0055 UTC 14 December 2001. The period of these legs coincided with the passage of the large precipitation band associated with the middle-level front. A depiction of the observed and simulated vertical velocities along the P-3 flight track overlaid on elevation data, is displayed in Fig. 4.7. The model values were linearly interpolated in time and space from 15 minute model output. The first P-3 north-south leg over the Willamette Valley showed minor fluctuations in the meteorological variables. Winds were relatively uniform at 234 degrees and 35-40 m s^{-1}

and temperatures averaged around 2 °C (Fig. 4.6). Vertical velocity measurements also indicated minimal vertical forcing at flight level with most of the leg showing vertical velocity perturbations of less than 50 cm s^{-1} (Fig. 4.6, 4.7a). Along leg 1 of the P-3 flight track both the 4-km and 1.33-km nests (Fig. 4.7b,c) simulated relatively weak vertical velocities, as found in observations (Fig. 4.7a). The simulated values had less variance than the observed but the differences remained within the 30-50 cm s^{-1} errors of the observations.

Over the foothills of the Cascades during the second leg, there was larger variability in the terrain and meteorological variables compared to the other legs (Fig. 4.6). Figure 4.8 provides more details of the meteorological variables and underlying terrain along leg 2. Along this leg, there are a system of ridges and valleys extending west from the crest of the Cascades (Fig. 4.7a). The ridges rise upward to 1000 m and are on average about 10-15 km wide while the valleys' mean elevation was about 500 m and the valleys varied in width from 10 to 15 km along the south-north oriented flight track. The significant elevation gradient between these valleys and ridges (in some cases a 700 m rise over 10 km) and the stable stratification of the airflow provided an environment favorable for the generation of gravity waves.

In situ observations along leg 2 indicate the wind speeds were approximately 34-40 m s^{-1}, fluctuating in direction between 230-240 degrees. As this strong southwesterly wind impinged on the east-west oriented ridges it was forced upward. Evidence of this is found in Fig. 4.8 where positive vertical velocity perturbations are generally collocated with the windward sides of the ridges. In some areas vertical velocity reached sustained values of 200-300 cm s^{-1} over 10 km sections of the flight track. In contrast, on the lee side of the ridges, areas of pronounced subsidence were present. In some areas along leg 2 vertical velocity measurements varied by 400 cm s^{-1} along a 10 km segment of the flight track.

The 1.33-km model realistically simulated (to within 50 cm s^{-1}) the the general characteristics of the vertical velocity variations along leg 2, as seen by the dashed red line in Fig. 4.8, although the amplitude of the simulated vertical velocities are often too small. This is much improved from the 4-km simulation (green line in Fig. 4.8 and Fig. 4.7b), which
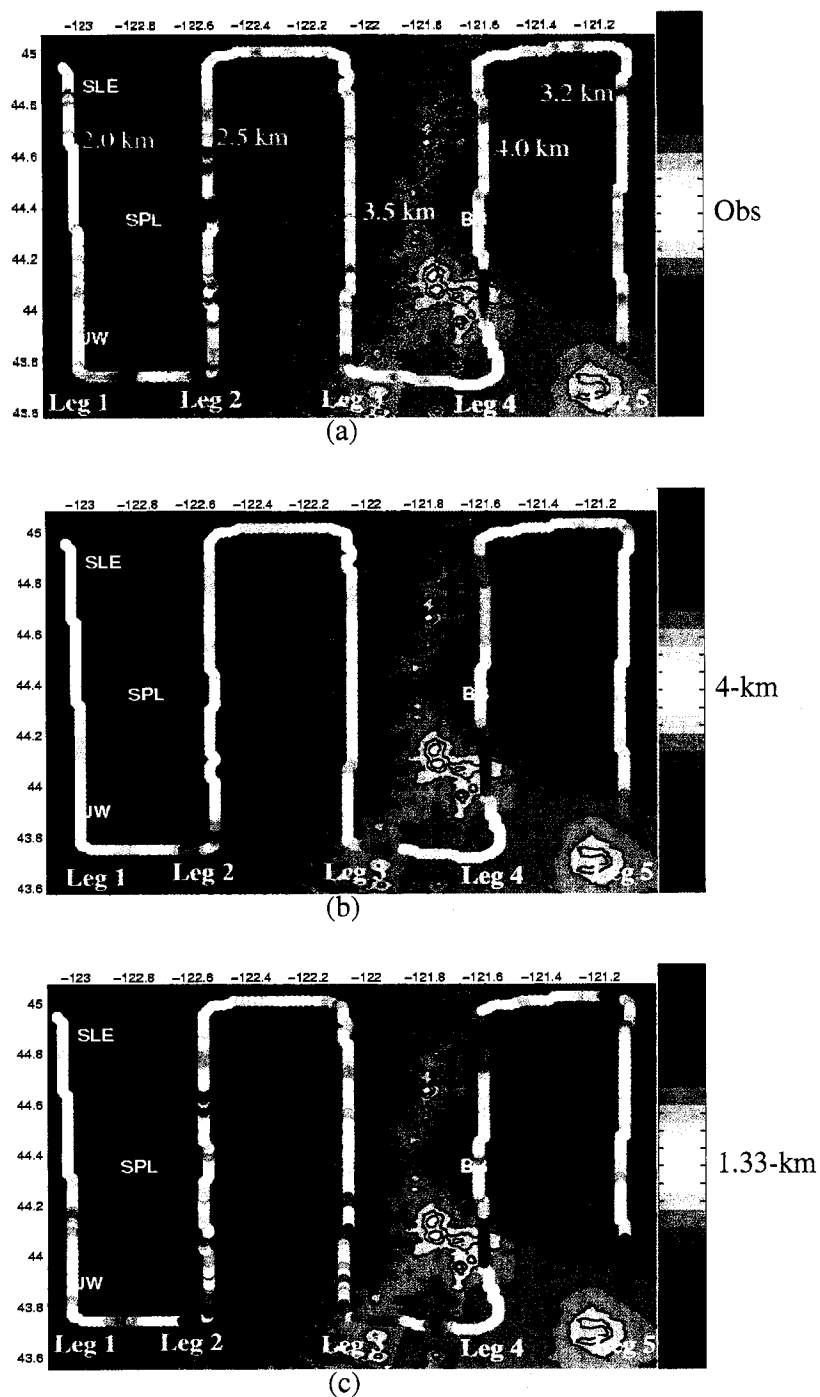
Figure 4.7: (a) Observed, (b) MM5 4-km model, and (c) MM5 1.33-km model vertical velocity (cm s^{-1}) along P-3 flight track from 2302 UTC 13 December 2001 through 0100 UTC 14 December 2001. Elevation shading lightens with height at intervals of 300 m. Heights of flight legs are also listed. Darkest blue colors along leg 5 in (c) depict areas outside the 1.33-km model domain.
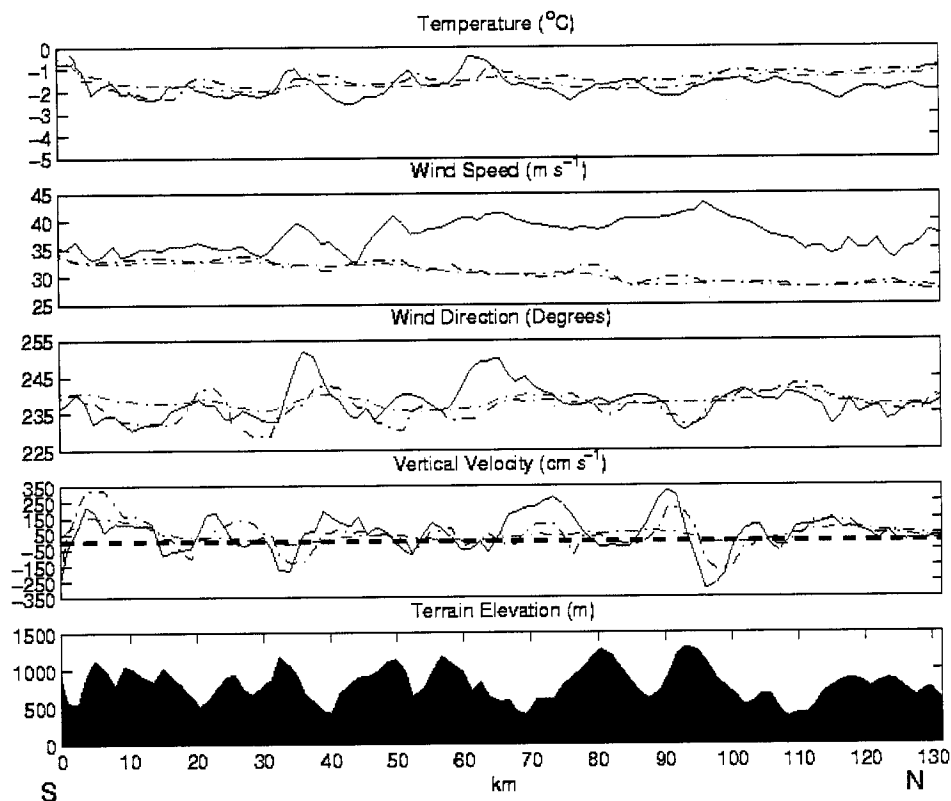
Figure 4.8: Comparison of meteorological variables for leg 2 of the P-3 flight track from 2330 UTC through 2345 UTC 13 December 2001. The lower panel shows the terrain under the flight track. Solid blue line is observed. Dashed green lines are values from 4-km model simulation. Dashed red lines are from 1.33-km model simulation.

indicated vertical velocity errors of almost 250 cm s^{-1} in places. Despite the more accurate vertical velocity of the 1.33-km simulation, flight level winds for leg 2 were still 10 m s^{-1} weaker than observed. With weaker winds, it might be expected the modeled vertical velocities would be lower since the flow would not be forced up the barrier as rapidly. However, the strength of wind field in the layer below the flight level of 2.5 km were slightly overpredicted by the model as indicated by radial velocity scans from the SPOL radar (Colle et al., 2004), which may account for the reasonable strength of the simulated vertical velocity.

Vertical velocity oscillations along leg 2 were responsible for temperature fluctuations

as large as 2°C (Fig. 4.8). The complex terrain also appeared to modify the direction of the horizontal flow. At various points throughout leg 2, the wind direction had a more westerly component, in some cases being deflected by as much as 20 degrees. This directional change generally coincided with valley locations, where winds accelerated eastward. The calculated non-linearity parameter from the UW sounding was around 0.5 and radar measurements showed low-level flow contained a significant cross barrier component indicating blocking was not an important feature with this storm (Colle et al., 2004). The origins of the perturbations in the wind field will be explored by the more extensive Doppler data set in the next section. The 4-km model simulation did not appear to capture the modification of the temperature and wind direction as well as the 1.33 km.

Leg 3 was flown at 3.5 km about 20 km west of the Cascade crest. The observed in situ winds increased to 40 m s^{-1} and veered to a more westerly direction of around 250 degrees (Fig. 4.6). Similar to leg 2, alternating areas of subsidence and rising motions occurred along the flight track. The amplitude of fluctuations in vertical velocity diminished compared to leg 2, despite the fact the underlying terrain remained complex. To properly interpret this observation, it should be noted that the height of the terrain along leg 3 had a mean altitude of 1.5 km, which was 2.0 km below the flight level of 3.5 km. Therefore the impact caused by orographic forcing was less compared to leg 2, which was flown closer to ground level. Additionally, the gradient of the terrain was not as large as in leg 2. A comparison of the observed vertical velocity along leg 3 (Fig. 4.7a) with model simulations indicated that the 4-km model grid (Fig. 4.7b) was not able to resolve the wavelengths and amplitudes of the terrain-induced gravity waves while the 1.33-km simulation (Fig. 4.7c) was more successful in this regard.

Leg 4 and 5 were flown to the lee of the Cascade crest. The horizontal wavelength of the vertical velocity oscillations along these legs was considerably larger than for the windward legs (Fig. 4.7a). Two noteworthy areas of subsidence were located around 44 °N and 44.8 °N along leg 4. These areas of downward vertical velocity resulted from large-amplitude mountain waves downwind of the major volcanic peaks of the Cascades. For leg 4, both

the 4-km and 1.33-km nests (Fig. 4.7 b,c) were able to depict the larger-scale downward vertical velocities to the lee of the volcanic peaks. However, the 4 km simulation had errors depicting the upward vertical velocity centered over Black Butte (BB).

4.3 Dual-Doppler Analyses

Although the in situ measurements provide useful thermodynamic and kinematic information at flight level, a more comprehensive three-dimensional picture is necessary for the verification of the model simulation. The P-3 was equipped with a helically-scanning Doppler radar, which provided a three-dimensional view of the flow structures during the 13-14 December 2001 case from the windward slopes extending to the lee.

The capability of airborne dual-Doppler radar to map 3D wind fields over complex terrain is well established (Colle and Mass, 1996; Yu and Smull, 2000; Bousquet and Smull, 2003a,b). Using the fore- and aft-scanning technique (Frush et al., 1986; Jorgensen and Smull, 1993; Hildebrand, 1998), 3D-reflectivity and radial velocity data for the 2-hour period from 2300 UTC 13 December through 0100 UTC 14 December 2001 were gathered within five overlapping ~40 km wide volumes centered along each of five N-S oriented flight legs (Fig.2.1). Each N-S leg took approximately 30 minutes to complete. The regular spacing of these five legs provided continuous, overlapping dual-Doppler coverage over the sizable IMPROVE-2 study area, and is thus extremely well suited for evaluation of mesoscale simulations of terrain-modified airflow and precipitation processes.

While airborne Doppler measurements are generally regarded as quantitatively useful to a range of ~40 km, the relatively tight spacing of the P-3 legs allowed restriction of analyzed data to a zone within ~20 km on either side (i.e. east and west) of each track, assuring a high-fidelity analysis. Prior to interpolation, radial velocity and reflectivity measurements were subjected to a combination of automated and manual editing as described by Bousquet and Smull (2003a) to remove ground clutter contamination, noise and other artifacts. Radial data were then interpolated to a composite Cartesian grid measuring 240 km x 170 km in the horizontal with 1 km resolution in east-west and north-south directions,

and 0.25 km resolution in the vertical from immediately above the terrain to a maximum height of 10 km MSL (or echo top, if lower). Multiple radial views from subsequent 'fore' and 'aft' scans were synthesized following Jorgensen and Smull (1993) to yield continuous fields of horizontal airflow (U,V) and reflectivity (dBZ) in regions of detectable echo. Synthesized reflectivity and component airflow fields were subjected to a two-pass Liese filter to eliminate poorly-resolved smaller-scale features and to assure smooth, continuous transitions across "seams" separating data from individual flight legs. The absence of notable discontinuities at these locations speaks to the success of this approach.

Rudimentary estimates of vertical air motion were performed by downward integration of the anelastic continuity equation. Downward integration serves to minimize error growth (Ray et al., 1980) and these vertical velocity estimates remained bounded and well-behaved at the lowest levels. The resulting composite analysis utilized in this study provides a uniquely expansive and largely uninterrupted view of kinematic and precipitation fields fully spanning the Cascade crest extending from the Willamette Valley (located >100 km upstream) eastward to the lee-side desert plateau in central Oregon. Due to the relatively slow evolution of flow and precipitation structures during this period of prefrontal P-3 sampling (Fig. 4.3), the composite analysis may be viewed as a steady-state depiction of the precipitation and flow pattern characterizing the entire 2-hour period.

4.3.1 Mesoscale Model Setup and Description

The configuration of the model simulation used for comparison with the Doppler analyses was identical to the original MM5 simulation presented in Chapter 2 except that the nudging on the outer domains was extended to twenty-four hours (from 0000 UTC 13 December to 0000 UTC 14 December) as opposed to the 12-hours (0000 UTC to 1200 UTC 13 December) used in the original simulation. As a result, there was an improvement in the strength of the mid-level wind speeds and the timing of the surface front. In addition to the 36 and 12 km domains, a separate 4-km simulation with a 1.33-km nest centered over the central Oregon Cascades was run for 24-hours initialized at 1200 UTC 13 December

2001. The 1.33-km domain was expanded from the original dimensions in Chapter 2 to encompass a larger area to the east (leeside) of the crest as well as the coastal mountains to the west. The inner domains did not employ nudging or a cumulus parameterization.

4.3.2 Windward Slopes

At a height of 1.5-km MSL, airborne Doppler measurements showed southwesterly flow over the Willamette Valley (Fig. 4.9a). As this flow encountered the elevated terrain of the Cascade foothills, frictional effects decreased the wind speeds. Observed reflectivity showed relatively heavy precipitation over the entire study area, with pockets of enhanced reflectivity reaching 40 dBZ over the windward slopes, with a significant reduction of values on the lee slopes (Fig. 4.9b). Winds at 3-km (i.e., above crest level) were more westerly (Fig. 4.9c), with a pronounced maximum in wind speeds to the lee of the Cascade crest. The observed veering of winds between 3.0 and 4.5-km (c.f. Fig. 4.9c and e) was consistent with warm advection ahead of the frontal system, as previously seen in Fig 4.1b. Reflectivity patterns seen in Fig 4.9b,d,f, will be extensively discussed in Chapter 5.

Averaged E-W cross sections of the radar-observed U- and V-component flow provide a general view of kinematic fields across the Cascades (Fig. 4.10 a,c). These sections were constructed by meridionally averaging the gridded 1-km dual-Doppler data over the 140-km north-south region between 44.0 and 45.0 °N (boxed region in Fig. 4.9e). Analogous mean cross sections of simulated flow (Fig. 4.10b,d) were created using the U- and V-fields from the MM5-1.33-km simulation. The MM5 cross-sections were averaged for the time period of the P-3 flight, from 2300 UTC through 0100 UTC 13-14 December 2001 (forecast hours 11-13) using model output at 15 minute intervals.

As initially suggested by the UW sounding and IB profiler, airborne dual-Doppler data indicate that the incoming flow was strongly sheared upwind of the crest, with the U-component increasing more than 20 m s^{-1} from the surface to the top of the shear layer at approximately 2-km MSL (Fig. 4.10a). The depth of this shear layer remained relatively constant as flow ascended the windward slopes. Above the shear layer, a jet of stronger

46
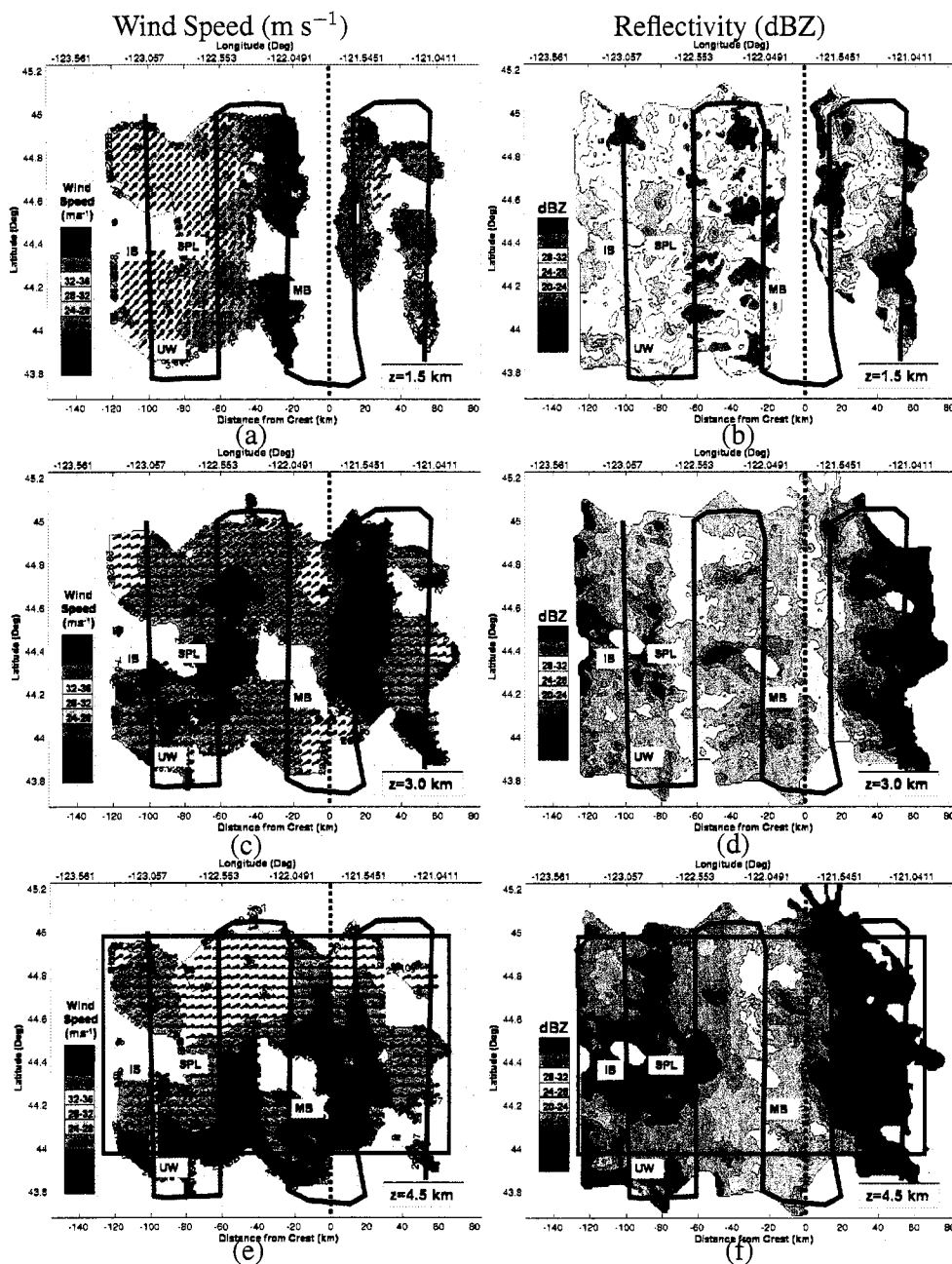
Figure 4.9: Composite grid of P-3 dual-Doppler wind speed (m s^{-1} color shading) and wind vectors (a,c,e) and corresponding radar reflectivity (b,d,f) at elevations of 1.5-km, 3-km and 4.5-km AGL. Red line indicates flight track of P-3 over the two hour period from 2300-0100 UTC 13-14 December 2001. Black box in (e) and (f) outlines region over which data were averaged to create the mean E-W cross sections in Fig. 4.10 and Fig. 5.5, respectively. Dotted lines depicts N-S mean crest line.

($>$36 m s^{-1}) cross-barrier flow centered at 3-4 km began approximately 90-km upstream of the mean crest. This jet strengthened as it approached the crest, reaching speeds greater than 40 m s^{-1}. The U-wind (cross-barrier) flow structure over the windward Cascade slopes differs appreciably from cases of profoundly blocked flow observed adjacent to taller mountain ranges such as the Sierras (Marwitz, 1987a) and Alps (Bousquet and Smull, 2003a,b). In those events, radar and in situ measurements depicted the U-shear layer as being concentrated below the crest level, with the depth and strength of the shear layer decreasing with proximity to the crest. (cf. Fig3c in Marwitz 1987a and Fig 8c of Bousquet and Smull 2003b).

In the present case, strong V-component (along-barrier) flow was concentrated within the U-shear and decreased with height above this layer (Fig. 4.10c). There was a $\sim$4 m s^{-1} enhancement in the V-flow over the Willamette Valley ($\sim$100-km upstream of the crest), but the absence of a clearly defined V-maximum (or "barrier jet") below crest level further distinguishes this IMPROVE-2 case from aforementioned examples of profoundly blocked flow.

To illustrate better the alteration of the wind components by terrain, "upstream" U and V profiles were created by averaging the dual-Doppler wind fields over a section of the the Willamette valley between -123.30 and -123.06°W (dashed boxed region at left edge of Fig 4.10a). Since the terrain elevation of the Willamette Valley is near sea-level, the upstream profile's wind values in MSL are roughly equal to those above the ground level (or AGL). The "upstream" U (and V) AGL profiles were subtracted from the corresponding U (and V) values AGL over the rest of the cross section in Fig. 4.10 to create the U (and V) prime (') plots (Fig 4.11)[1]. Using this methodology, the frictional deceleration of the U-flow following the sloping terrain would be eliminated so that other terrain influences (such as blocking) are better illuminated.

---

[1]For example, over the windward slopes where the average terrain height was 0.75 km, a height of 2.00 km MSL would be equal to 1.25 km AGL (A in Fig 4.10a). The U-value at A located over the windward slopes at 1.25 AGL ($\sim$22 m s^{-1}) would then be subtracted from the "upstream" U-value at B of ($\sim$18 m s^{-1}) resulting in a U$'$ value of 4 m s^{-1} (C=A$-$B) shown in Fig 4.11a.
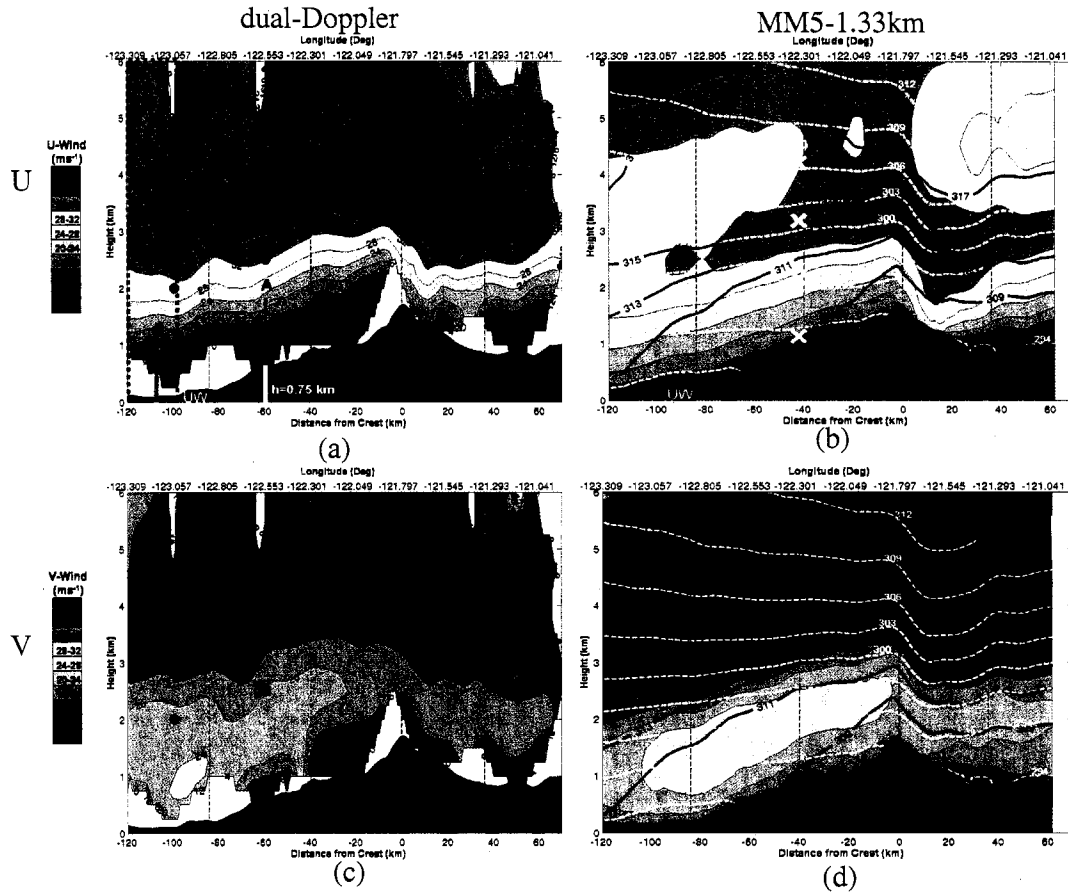
Figure 4.10: Average E-W cross section from airborne dual-Doppler composite grid of (a) U-component and (c) V-component flow (color shading, m s^{-1}). Black dots in represent the position of P-3 north-south leg. Dashed lines delineate the boundaries separating individual Doppler analysis grids included in the composite. Dashed black box (a) shows region averaged to create the "upstream" profile used to calculate Fig 4.11. Averaged E-W cross section of MM5 1.33-km simulated (b) U-component and (d) V-component with contours of simulated equivalent potential temperature (θ_e - black contours) and potential temperature (θ - dashed white contours). Model fields were averaged in time from 2300 UTC-0100 UTC 13-14 December 2001 (forecast hours 10-13) using model output at 15 minute intervals. White x marks in (b) are the ending locations of the trajectories shown in Fig. 4.12.
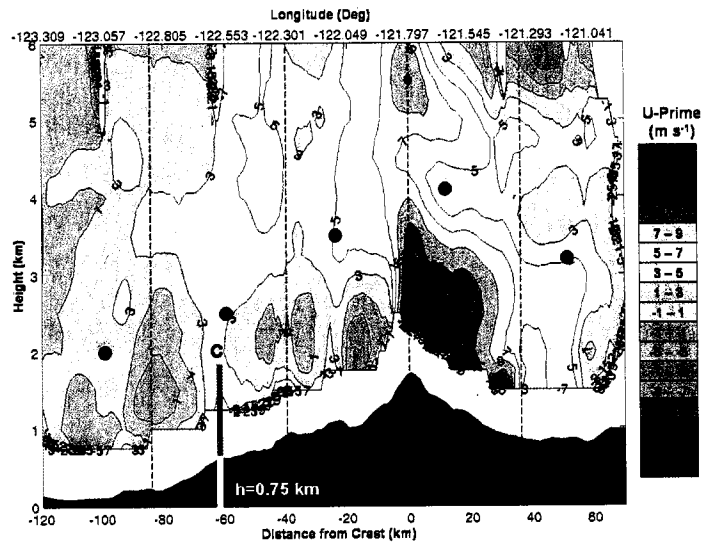
(a)
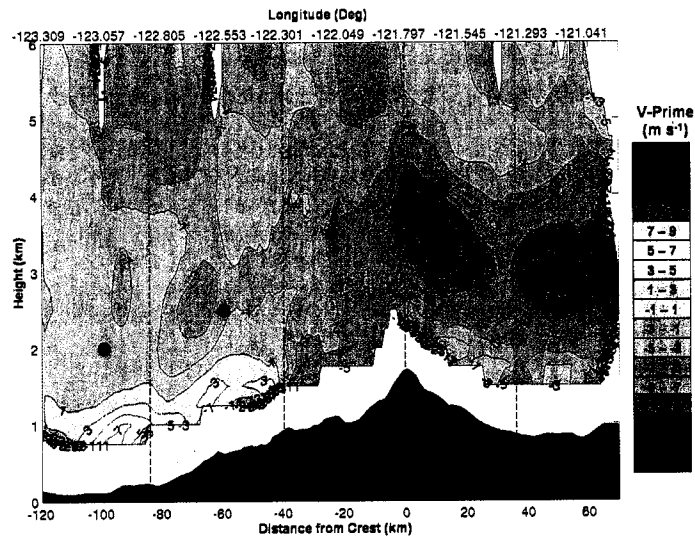
(b)

Figure 4.11: Dual-Doppler (a) U′ and (b) V′ in E-W cross section derived from Fig. 4.10a and c. Black dots in represent the position of P-3 north-south leg. Dashed lines delineate the boundaries separating individual Doppler analysis grids included in the composite. White areas indicate areas where not prime values could not be calculated.

Immediately above the foothills, U' values were predominantly between -1 and 1 m s^{-1}, indicating that excluding height dependent frictional effects and warm advectional veering the cross-barrier flow at the lowest radar-sampled levels was relatively unperturbed by the terrain (Fig. 4.11a). By contrast, large positive U' values were concentrated over the lower lee slopes, and extended westward to a height of 6-km over the crest. This pattern can be attributed to a vertically propagating mountain wave over the crest, which will be discussed in more detail in the next section. For the along-barrier flow, there was a small area of positive V' values of 5-7 m s^{-1} centered 100-km upstream of the crest below 2.0-km (Fig. 4.11b). Otherwise the V' values over the windward slope were close to zero, corroborating the observations in Fig. 4.10c which failed to indicate a pronounced barrier jet or other signs of pronounced blocking. The observed flow patterns and computed flow perturbations thus support the calculations of the non-linearity parameter in Fig 4.4, which predicted a "flow over" regime in which blocking effects are minimal.

Corresponding MM5-averaged E-W cross sections of U and V are displayed in Fig. 4.10b,d. The MM5 successfully simulated the broad characteristics of the flow, including the low-level shear in the U-component and core of stronger U above the shear layer. The model also correctly simulated the strong V-component at low levels rising over the windward slope, as well as the observed decrease of V with height above 2-3 km. The strong V-winds at low-levels were associated with the warm air advection taking place during this time. Yet there were also problems with the simulation's representation of the flow kinematics over the windward slopes. The strength of the U-shear was underpredicted, with low-level U-values being too strong while those above 2-km were 5-8 m s^{-1} too weak. Additionally, the height of the modeled U-wind shear layer over the windward slopes was about 0.5 km less than observed. Low-level V-component values were 4-6 m s^{-1} stronger than observed, with the elevated core of maximum V values extending farther east toward the lee than observed. The implications of these errors on the structure and strength of mountain waves within this region will be explored in the next sub-section.

In addition to the MM5 U and V-values, simulated θ and θ_e contours are also plotted

in Fig. 4.10b,d. Since the environment during the 13-14 December case was close to saturation up to 4-km (Fig 3.6c), θ_e can be treated as a tracer of the steady-state flow, except in areas where diabatic processes (such as melting) are active. Enhanced vertical gradients of θ (dashed white lines) and especially θ_e (solid black lines) were found surmounting the zone of weaker low-level U-winds and within the zone of enhanced U aloft (Fig. 4.10b). This corresponds well with the UW sounding shown in Fig. 4.4 (position of UW labeled in Fig. 4.10a,b), which shows the strongest N^2 values (and increased stability) between 2-3 km coinciding with the top of the shear layer. Stronger V-component flow was centered below the θ_e gradient and rapidly decreased with height above (Fig. 4.10d). Lowering values of θ towards the crest are consistent with reflectivity observations from the P-3 radar, which showed a tendency for the bright-band (and associated 0°C level) to descend towards the Cascade crest (as will be shown in Chapter 5). An MM5-simulation in which diabatic effects of melting were excluded (not shown) indicated that melting had a minimal influence on θ values on the windward slopes.

Trajectories were calculated to determine the origin of the θ_e and θ gradient present in Fig. 4.10 b,d using the 4-km domain MM5 simulation. Figure 4.12a shows the paths of four trajectories ending at 2300 UTC 13 December (forecast hour 12). All terminate at the same horizontal location (44.3 °N, -122.3 °W) but at heights ranging from 1 to 4 km (Fig. 4.10b). These trajectories were calculated using 600s time-steps from MM5 4-km hourly output. Lagrangian values of pressure, θ, θ_e, and relative humidity for each of the four trajectories are displayed in Fig. 4.12b.

The parcel ending at 1-km moved northward nearly parallel to the Cascades, at a relatively constant pressure-level of 910-hPa from 1200-2300 UTC 13 December. This parcel was sub-saturated from 1200-1800 UTC 13 December, although relative humidities increased from 75 to 90% along its northward track. After 1800 UTC, the parcel's relative humidity remained close to 100% as it neared the zone of enhanced orographic precipitation over the IMPROVE-2 study area. The values of θ_e and θ for this parcel showed a 5-6 K increase during its northward trajectory, probably as a result of vertical mixing. The

parcel ending at 2-km followed a similar course, originating to the south-southwest off the coast of California. This parcel remained at a pressure level of around 950-hPa between 1200 and 2000 UTC, but then rose to level of 784-hPa as it encountered the higher terrain of the Cascade foothills. The θ and θ_e values along this trajectory also experienced a 5°K increase during the 4-hour interval plotted, again indicative of warming induced by mixing. The two parcels that ended at 3 and 4-km both originated within a distinctly different air mass and region than the lower trajectories. Both originated to the west-southwest of the study area over the open water of the Pacific, in a nearly saturated air mass characterized by higher θ_e values. The 3- and 4-km parcels experienced significantly more ascent than the lower parcels, rising over 225-hPa in less than five hours. These elevated parcels' θ_e values remained relatively steady, while θ dramatically warmed due to release of latent heat of condensation.

4.3.3 Smaller scale waves (< 20-km) along windward slopes

Thus far this chapter has examined the kinematics along a meridionally-averaged E-W cross section spanning across the Cascade crest. Yet as the in situ data indicated, the strong southerly component of flow at low-levels had significant impacts on vertical velocity at smaller scales (horizontal scales < 20 km) over the complex terrain of the windward slopes. The top three panels of Fig. 4.13 show in situ, model-predicted and dual-Doppler-derived U,V, and W-components at a height of 2.5-km along leg-2 of the P-3's composite flight track (as shown in Fig. 2.1). At a height of 2.5-km this flight track was positioned near the top of the U-shear layer with (U,V) components averaging near 32 m s^{-1} and 20 m s^{-1}, respectively (P-3 position indicated by black dot 60-km upstream of mean-crest in Fig. 4.10a,b). The in situ and Doppler-derived U and V components along leg-2 indicated that the winds varied by 5-7 m s^{-1} over horizontal distances of 10-15 km in this region. As mentioned earlier, these variations of the wind fields can be directly linked to details of the underlying terrain, as positive V-component perturbations were collocated with local peaks in the windward foothills while stronger U-flow occurred above valley locations. The MM5
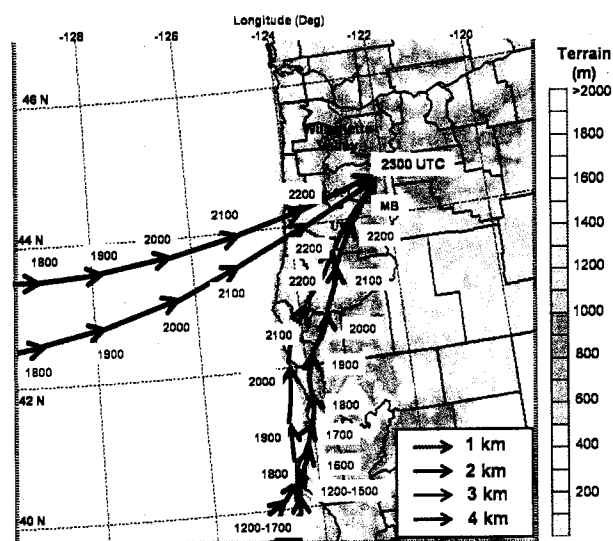
(a)
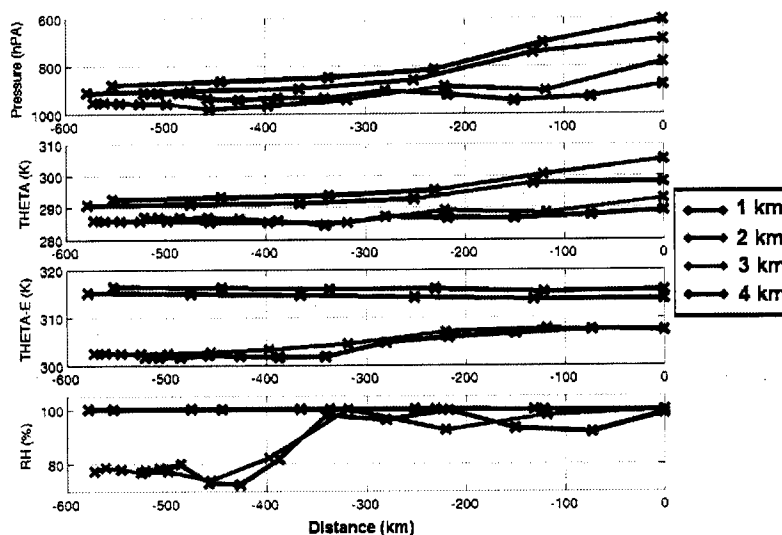
(b)

Figure 4.12: (a) Map of backward trajectories terminating over the windward slopes of the Cascades (at -122.8 °N and 44.5 °W) at 2300 UTC 13 December 2001 at four different heights (key lower right) as shown in Fig. 4.10c. (b) Lagrangian traces of pressure (hPa), potential temperature(K), equivalent potential temperature (K), and relative humidity (in percent) following the parcel tracks shown in (a), plotted against distance (km) from endpoint.

correctly simulated the presence of the wind perturbations along this flight-track, except for over-predicting the amplitude of the V responses and underpredicting the U variations relative to those observed.

In situ measured vertical velocities along leg-2 show significant terrain-induced perturbations. As discussed previously, positive vertical velocities coincided with areas in which the strong V-component flow impinged on higher terrain and was forced upward. Meanwhile, negative vertical velocity perturbations were preferentially located on the lee (north) side of these ridges coincident with the stronger V-components. The model was also shown to accurately predict the magnitude and positions of these vertical velocity oscillations but over-predict the amount of CLW (Fig 4.13). Such perturbations in CLW will be more fully explored in the next chapter.

Dual-Doppler estimates of vertical air motion (w) were derived by downward integration of the anelastic continuity equation subject to a boundary condition of $w=0$ immediately above echo top. In the presence of large-amplitude, vertically-propagating waves, this assumption may be violated and constitute one important source of error. Nonetheless, corroboration of these w estimates by independent observational measures (and as will be seen, simulation results as well) lends increased confidence in their veracity. In keeping with their inherently coarser spatial resolution, the interpolated Doppler-derived vertical velocities were significantly smoother than the in situ aircraft data yet still showed close agreement with the phase and sign of longer-wavelength features of the flow (Fig. 4.13). The Doppler-derived vertical velocities therefore can provide rudimentary, yet useful information on the amplitude and phase of these smaller-scale features.

Doppler-derived vertical velocities were overlaid on the Doppler U- and V-component fields along the north-south cross section of leg-2 (Fig. 4.14a,c). The strongly sheared U-flow was clearly present below 3 km, with near surface U-winds of greater than 8 m s^{-1} increasing to 36-40 m s^{-1} at a height of 3.5 km. Within this strongly sheared layer of U, V-values reached greater than 28 m s^{-1} below 3 km. As this strong V-flow impinged upon the underlying foothill terrain, the strong vertical velocity perturbations seen in the in situ
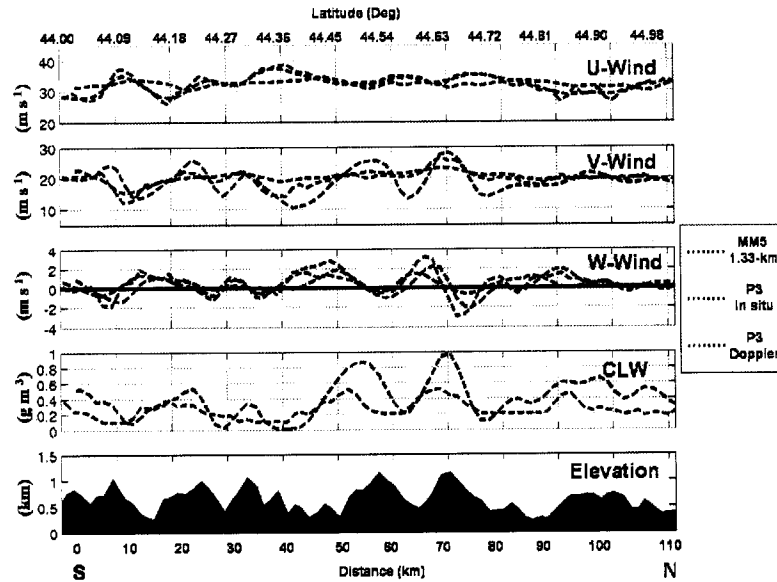
Figure 4.13: U, V, and W components (m s^{-1}) at 2.5 km MSL along leg-2 of the P-3 flight track (location shown Fig. 2.1) from the MM5-1.33-km model simulation, P-3 in situ measurements, and as derived from dual-Doppler measurements (key at right). The fourth panel shows CLW measurements along leg-2 as measured by the PMS-KING probe aboard the P-3 and as predicted by the MM5-1.33-km simulations. The lowest panel is the underlying terrain along the flight track.

data were clearly evident in the Doppler-derived w-field. Due to the rudimentary boundary conditions applied to derive the vertical velocity, the w-values can only be viewed qualitatively. Yet despite the boundary condition of $w=0$ at echo top, positive w values of greater than 0.2 m s^{-1} were registered at heights of 5 km, indicating the significant upward penetration of these small-scale mountain waves generated over the Cascade foothills. There was some evidence (located near 30-40 km and 70-80 km in the cross section) of acceleration of the V-flow in the lee of steeper and wider ridges (Fig. 4.14c), corroborating the in situ perturbations measured in Fig. 4.13. The presence of acceleration on the lee side of these localized barriers that are collocated with negative w perturbations, is consistent with theoretical depictions of vertically propagating wave behavior (Durran, 2003).

dual-Doppler   MM5-1.33km

U-Wind

(a)

(b)

V-Wind

(c)

(d)
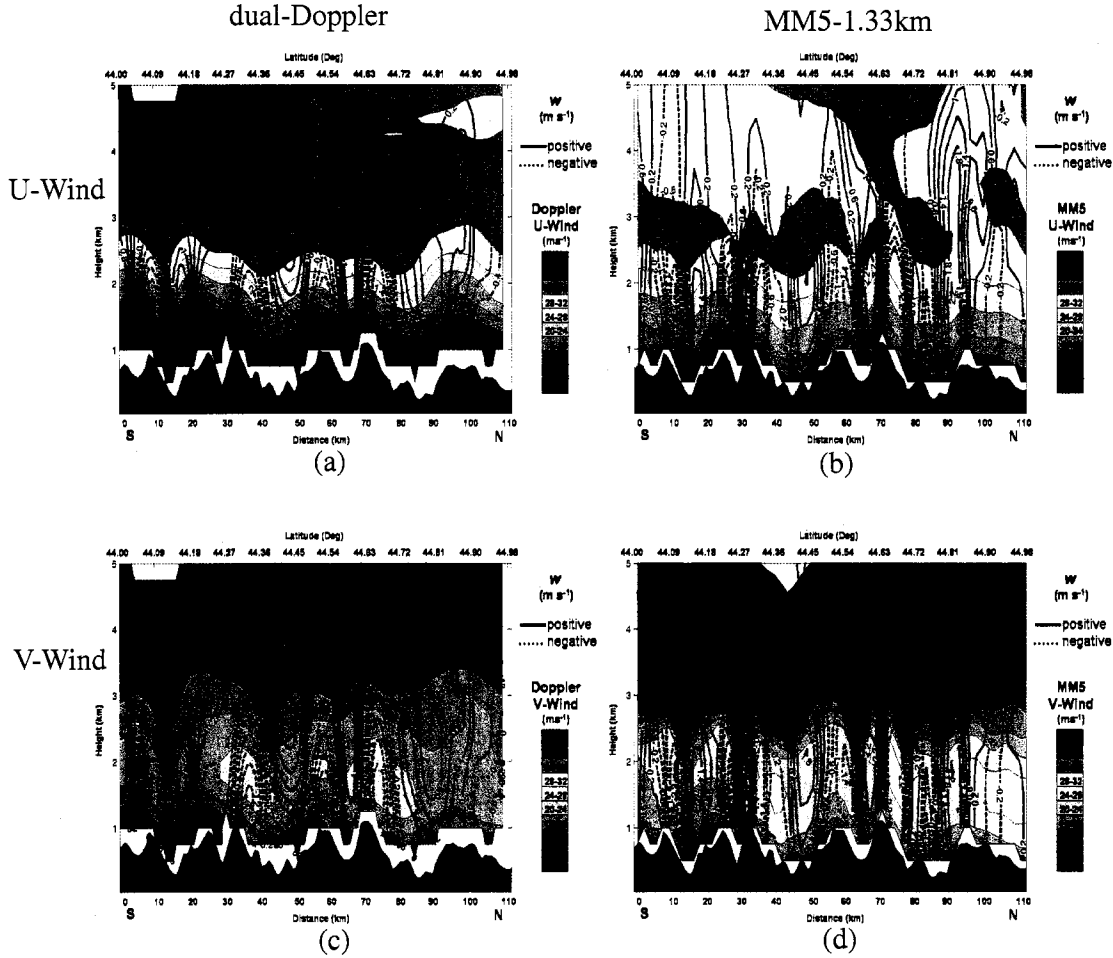
Figure 4.14: N-S cross-section of airborne dual-Doppler and MM5-predicted U- and V-component flow along leg-2 of the P-3 flight track (cf. Fig 2.1a). Contours of Doppler-derived vertical velocity are displayed at intervals of 0.2 m s^{-1} in (a) and (c) while contours of model predicted vertical velocity are displayed in intervals of 0.3 m s^{-1} in (b) and (d). Negative contour values are dashed.

The MM5 U-and V-component flow fields along leg-2 (Fig. 4.14b,d) were in generally good agreement with observations, showing significant shear both in U and V below 3-km. As mentioned previously, the model simulation exhibited notable errors in this layer, with the shear layer in U-winds being shallower and weaker than observed and low-level

V-winds being 4-8 m s^{-1} too strong below 3-km. Despite these errors, the model's vertical velocity field compared well with the observations, simulating the dramatic oscillations associated with the strong V-values interacting with the complex terrain along leg-2. The model vertical velocity oscillations were stronger than the smoothed Doppler-derived w, consistent with in situ data analysis in Fig. 4.13. These simulated w-oscillations also showed greater vertical penetration than the Doppler data, which was probably closer to reality given the artificial boundary conditions $w=0$ at echo top imposed on the dual-Doppler analysis.

4.3.4 Leeside Region

The extension of radar-detectable precipitation to the lee of the Cascade crest presents an unique opportunity to examine the strength and amplitude of a stationary wave on a mountain barrier. In association with strong flow surmounting the Cascades, dual-Doppler observations showed this high momentum air plunging downward in the immediate lee of the crest (Fig. 4.10a). The observed 32 m s^{-1} contour, which approximately delineates the top of the U-shear layer, dropped from a maximum height of 3.0 km just upstream of the crest to 2.1 km [1.0 km above ground level (AGL)] approximately 10 km downstream (Fig. 4.10a). The 32 m s^{-1} contour then rebounded slightly, before remaining steady at about 2.2 km. Independent ground-based observations around this time indicated strong winds reaching the surface, with reports of downed trees in the immediate lee of the crest (Medina et al., 2005). The positive perturbations of the U-flow in the lee of the mountain crest (Fig. 4.11a) are consistent with the presence of a vertically-propagating mountain wave (Durran, 2003).

The MM5 also depicted a core of strong U-momentum air ascending the windward slopes and plunging downward in the lee of the Cascades (Fig. 4.10b). The modeled 32 m s^{-1} contour line dropped by approximately 1.2-km over a horizontal distance of 10-km from the crest to the lee, which is comparable in amplitude to the radar-observed displacement. However, the simulated core of strong U-momentum reached much closer to the ground

and spanned a larger horizontal downstream distance than was observed. Such errors in the model depiction of the mountain wave can increase the amount of precipitation spillover that reaches the ground and may contribute to an overprediction of precipitation in the lee as discussed in Garvert et al. (2005).

Previous research has shown that the structure and amplitude of mountain waves are sensitive to the boundary layer height and the depth of the shear layer (Smith, 1979; Peng and Thompson, 2003). As noted previously, the model underpredicted the strength and depth of the shear layer over the windward slopes of the Cascades. The top of the shear layer delineates the rapid change in θ_e (and θ) between the warmer θ_e (and θ) air aloft and the lower θ_e (and θ) air close to the surface. Since the depth of the modeled shear-layer was less than that observed, this upstream effect might account for subsequent errors in the depiction of the model's mountain wave over and leeward of the crest.

To assess the impact of the boundary layer and associated shear on the mountain wave over the crest, sensitivity tests were conducted using different planetary boundary layer parameterization (PBL) schemes available in MM5. As noted previously the control simulation was run with the MRF-PBL parameterization, which utilizes the Troen-Mahrt representation of the countergradient term (Hong and Pan, 1996). A second run was performed identical to the control but using the Eta-PBL parameterizations on the inner 4- and 1.33-km domains. The Eta-PBL, which is used in the operational Eta-model (Janjic, 1990, 1994), is a 1.5 order closure scheme in which turbulent kinetic energy (TKE) is predicted with a prognostic energy equation, as adapted from the Mellor-Yamada scheme.

The height of the low θ_e air and shear layer over the windward slopes in the Eta-PBL simulation was significantly less than the control run (Fig. 4.15 a,c). Yet the resulting gradient in the windward shear layer was stronger than that in the control simulation, better matching observations. In contrast to the dual-Doppler observations, the Eta-PBL simulation incorrectly brought stronger U-momentum values closer to the surface and over a wider area to the lee of the Cascade-crest. Additionally, the wave structures as depicted by vertical velocity in the Eta-simulation were significantly different than those in the control,
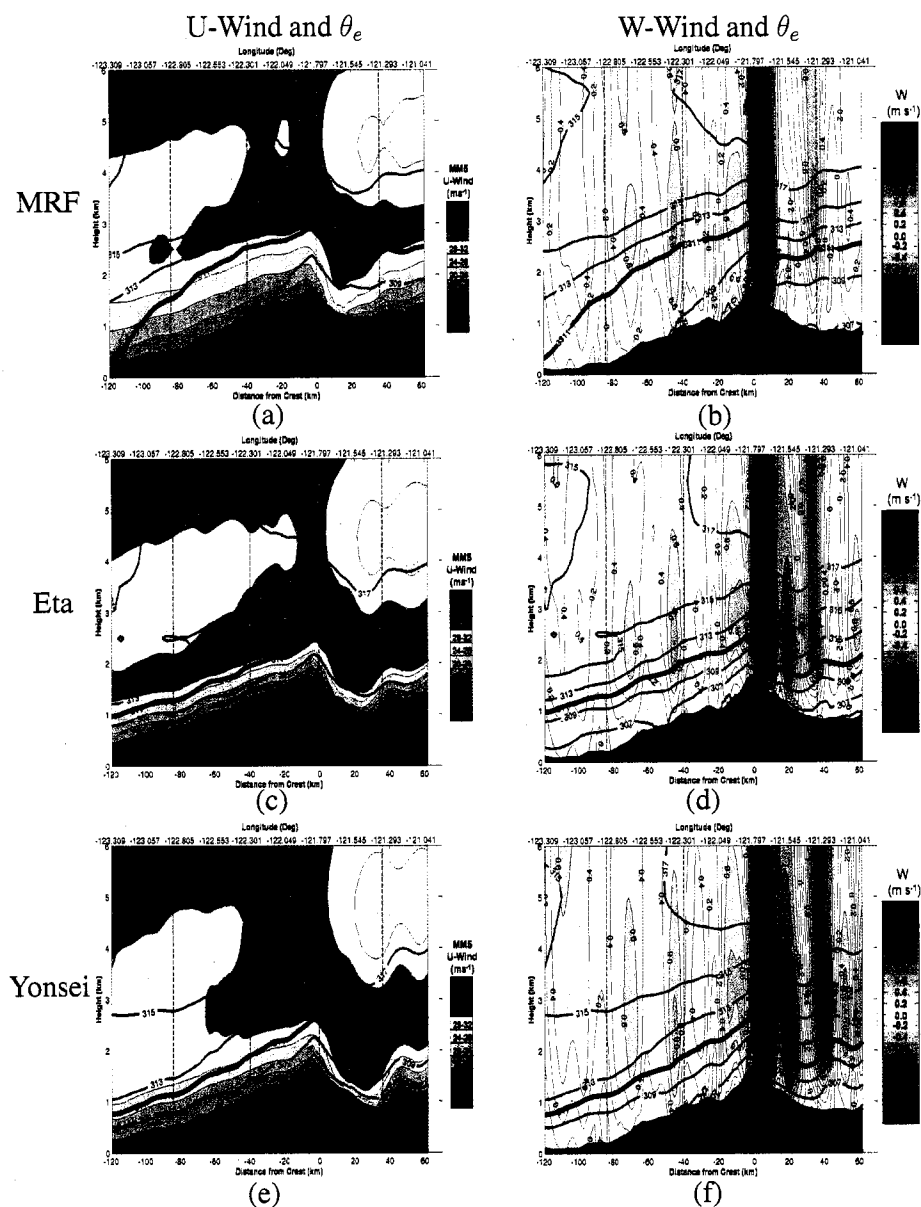
Figure 4.15: Average E-W cross sections of MM5-generated equivalent potential temperature (θ_e) overlaid on U-component flow (a,c,e) and vertical velocity (b,d,f) for three different 1.33-km MM5 simulations using the MRF-PBL, ETA-PBL and Yonsei PBL (top, middle, and bottom paired panels, respectively). Model fields were averaged in time from 2300 UTC-0100 UTC 13-14 December 2001 (forecast hours 10-13) using model output at 15 minute intervals

with higher amplitude vertical motions evident in the lee (Figs. 4.15b,d). It is interesting to note that the strongest vertical motions over the windward slopes were displaced downward in the Eta-PBL simulation. These areas of enhanced vertical motions in Fig. 4.15b are caused by perturbations in the slope of the underlying terrain and will be further examined in the next section.

A third simulation was performed using a modified version of the MRF-PBL (referred to an Yonsei-PBL) as outlined in Noh et al. (2003). The Yonsei-PBL produced results similar to the Eta-PBL simulation, reducing the depth of the upstream shear layer and increasing the amplitude of the lee wave response (Fig. 4.15e,f). The Yonsei-PBL, however, did not increase the strength of the shear layer as significantly as the Eta-simulation.

4.4 *Summary and Conclusions*

Two high-resolution simulations using 4-km and 1.33-km grid spacing were compared against in situ and airborne Doppler observations that were systematically collected by the P-3 during the 13-14 December event. The spatial coverage of the in situ and Doppler data provided a unique opportunity to obtain detailed descriptions of terrain-induced perturbations over complex terrain on a variety of scales. The Doppler observations greatly supplemented the in situ measurements by providing a fully three-dimensional, uninterrupted view of reflectivity and kinematic fields spanning the complex terrain of the Cascades extending from the Willamette Valley to the lee slopes.

It was seen that short-wavelength perturbations in the meteorological variables were present along the N-S legs of the P-3 flight track especially over the windward slopes of the Cascades. These variations in vertical velocity, temperature, wind direction, and wind speed were directly related to small-scale mountain waves caused by the southerly flow component interacting with small-scale ridges and valleys oriented normal to the larger N-S Cascade barrier. The 1.33-km model's vertical velocity field compared well with the Doppler and in situ observations, simulating the dramatic oscillations associated with the strong V-values interacting with the complex terrain. The model vertical velocity oscil-

lations were stronger than the smoothed Doppler-derived w, consistent with in situ data analysis. The simulated w-oscillations also showed greater vertical penetration than the Doppler data, which was probably closer to reality given the artificial boundary conditions $w=0$ at echo top imposed on the dual-Doppler analysis. It was found the model required 1.33 km grid spacing to capture the small scale oscillations.

The MM5 depicted a layer of low θ and θ_e air associated with strong low-level V-flow. The low θ values were consistent with reflectivity observations from the P-3 dual-Doppler showing the bright band sloping downward to the Cascade crest. Trajectory analysis indicates that the low-θ air originated to the south of the study area in a region of sub-saturation. A strong vertical gradient in θ (and θ_e) atop the U-shear zone was coincident with a decrease in the V-component and was surmounted by a core of enhanced U. Parcels within the strong U-component airstream originated well west of the study area over the Pacific in an area of high-θ and saturation. As this high-θ_e air approached the mountainous study area, it experienced acceleration and lifting, rising over the low-θ_e air. The kinematic structure of the 13-14 December 2001 case, with low-level V flow and a strong cross-barrier jet atop a sloping shear-layer, was also present in other IMPROVE and MAP cases (Medina et al., 2005). It would useful to further examine these cases to document the repeatability and generality of the phenomenon established in this chapter.

As the strong U-flow surmounted the barrier, dual-Doppler observations showed the high U-momentum air plunging downward in the immediate lee of the Cascade crest in a vertically propagating mountain wave. The MM5 also simulated the stronger U-momentum air over the windward slopes plunging downward to the lee of the Cascade crest, but the simulated strong U-momentum air clearly reached closer to the ground and over a larger horizontal distance than observed.

To assess the impact of the upstream shear profile and boundary layer on the simulated mountain wave, sensitivity tests were completed using three different planetary boundary layer parameterization (PBL) schemes available in MM5: the MRF-PBL, ETA-PBL, and a modified version of the MRF-PBL referred to as the Yonsei-PBL. It was shown that

all of the PBL-schemes underpredicted the vertical depth of the U-component shear layer and produced U-values that were too strong near the surface. The ETA- and Yonsei- PBL schemes produced significantly shallower windward U-component shear layers than the MRF, and also produced a stronger amplitude mountain wave over the mean crest. The PBL tests clearly indicate that the amplitude and strength of the mountain wave are sensitive to the upstream shear layer and choice of PBL-parameterization with none of the PBL schemes used correctly reproducing the observed structure. The incorrect depiction of the upstream shear layer in the simulation could be an important source of errors in the strength and amplitude of the modeled mountain wave anchored to the Cascade crest. It is therefore imperative that errors in the model depiction of the upstream shear layer and boundary layer parameterizations be corrected in order to further improve quantitative precipitation forecasts over complex terrain.

Chapter 5

PRECIPITATION DISTRIBUTION AND ASSOCIATED MICROPHYSICAL PROCESSES

This chapter applies a combination of high-resolution mesoscale model simulations and a uniquely comprehensive airborne Doppler radar observations to examine the mesoscale distribution of precipitation and associated microphysical processes characterizing the period of heavy prefrontal orographic rainfall over the Oregon Cascades on 13-14 December 2001 during IMPROVE-2. A analysis and verification of the model QPF is also presented and compared against past studies.

5.1   Verification of the Quantitative Precipitation Forecast

Observed precipitation totals from 1400 UTC 13 December 2001 through 0800 UTC 14 December 2001 over the 4-km domain are displayed in Fig. 5.1a. The precipitation totals were compiled from a variety of National Weather Service and Federal Aviation Administration locations, National Climatic Data Center cooperative observer sites, and special precipitation gauges deployed over the Oregon Cascades for IMPROVE-2 (Stoelinga et al., 2003). Observed precipitation over the coast and the Willamette Valley was between 10-50 mm during the 18-h period, with the majority of the precipitation occurring within the stratiform precipitation band associated with the middle-level front. Over the more elevated terrain of the coastal mountains and Cascades, precipitation totals were over 50 mm, while in the lee of the Cascades most stations recorded less than 10 mm.

There is a substantial gradient in observed precipitation over the study area especially along the crest and lee slopes of the Cascades, with precipitation decreasing rapidly from around 61 mm at Corbett (see CO in Fig 5.2) to less then 10 mm at the PARSL site (PAR)

64
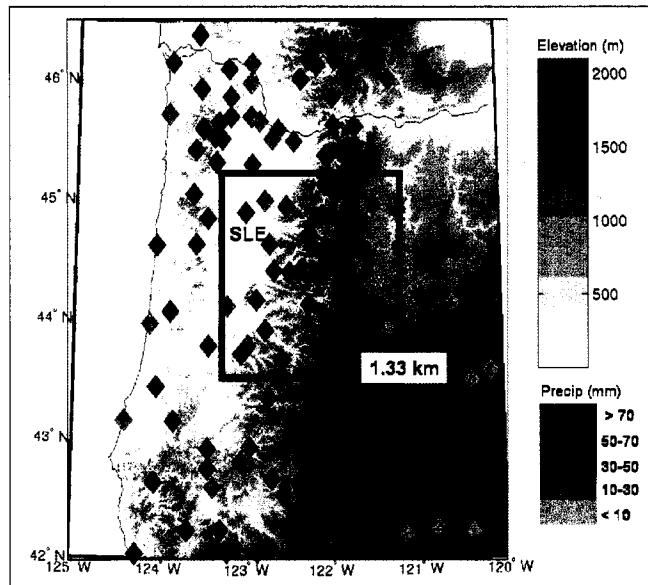
(a)
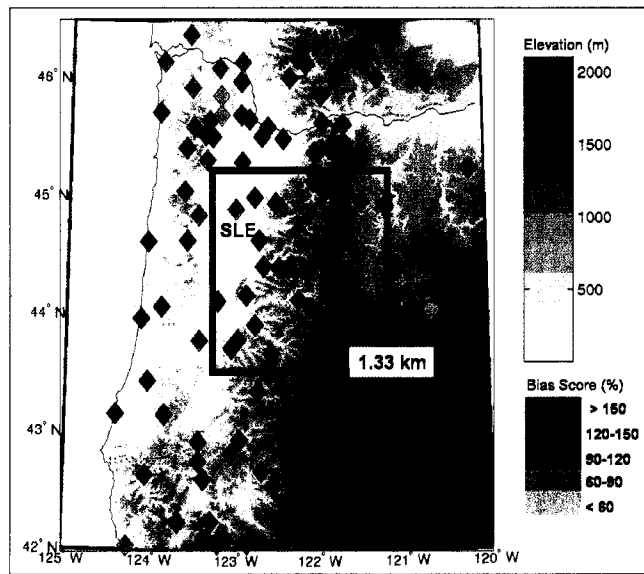
(b)

Figure 5.1: (a) Observed precipitation totals and (b) bias scores for 1400 UTC 13 December
2001 through 0800 UTC 14 December 2001 for the 4-km domain simulation.
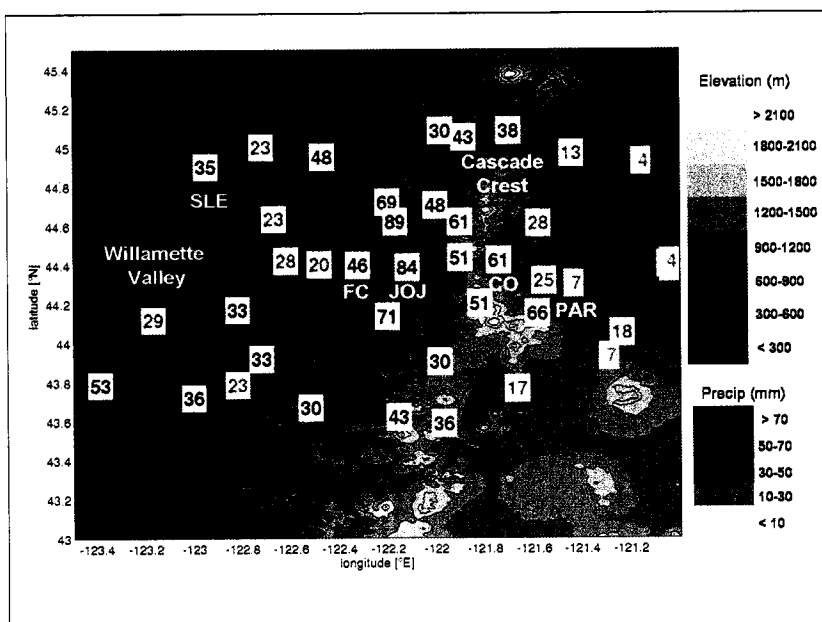
Figure 5.2: Observed precipitation totals over the 1.33-km domain for 1400 UTC 13 December 2001 through 0800 UTC 14 December 2001.

less than 25 km away. Additionally, there was significant spatial variability in precipitation totals over the windward slopes, with the Falls Creek site (FC) at an elevation of approximately 530 m recording 46 mm of precipitation, while a short distance to the east Jump Off Joe (JOJ) at 1067 m recorded 84 mm of precipitation (Fig. 5.2). The variability in precipitation amounts over small distance demonstrates the sensitivity of precipitation processes to the complex terrain.

In order to verify the model precipitation, totals from the model were interpolated to each observation site using the method outlined in Colle et al. (1999). The modeled precipitation was then divided by the observed precipitation and multiplied by 100 to give a percentage bias score. Figure 5.1b displays the 4-km domain bias scores for the 18-h period from 1400 UTC 13 December 2001 through 0800 UTC 14 December 2001. A bias score between 90-120 percent was considered an accurate precipitation forecast since undercatchment is expected at most observation sites (Colle et al., 1999).

Areas with accurate (bias scores of 90-120 percent) quantitative precipitation forecasts (QPF) occurred where orographic forcing was less pronounced, such as along the coast and within the Willamette Valley. A slight underprediction was evident to the lee of the coastal mountains and in parts of the Willamette Valley. Over the windward slopes and crest of the Cascades, there was substantial variability in the bias scores over short distances with a tendency toward overprediction. A large area of overprediction (bias scores > 150 percent) was present to the lee of the Cascades. However considering the low values of precipitation in these areas, the magnitude of these errors were generally less than 1 cm.

The 1.33-km bias scores indicated substantial variability over relatively short distances along the windward slopes (Fig. 5.3b). Nineteen precipitation sites were examined along the windward slopes and placed into two categories: windward hill and windward valley. For example JOJ was considered to be a hill location while FC was classified as a valley site. Sixteen of the windward gauges were located in valleys with eleven of those sites having bias scores of over 120 percent and only two underpredicting precipitation amounts. The valley sites had a mean bias score of 154 percent and bias scores varying between 61-250 percent. Of the three hill sites examined, the bias scores were between 92-110 percent with a mean bias score of 101 percent. Thus there appears to be tendency for high bias scores to be present at the valley sites while over the ridges bias scores appear to be lower. Yet, due to the relatively small number of measurements, possible errors in precipitation gauges, and sparse distribution of precipitation sites, analysis of additional storms is needed to validate this trend.

The bias scores for the 13-14 December 2001 storm, in which there is a great variability in bias on the windward slopes, contrast with past studies, which indicated a model tendency of broad overprediction of precipitation on the windward slopes of mountainous terrain at a grid resolution of 4-km (Colle et al., 1999, 2000; Colle and Mass, 2000). In addition, the overprediction over the lee slopes was not consistent with these studies, which had indicated underprediction downwind of terrain. At a number of locations the 1.33-km domain bias score's were different compared to the 4-km (Fig. 5.3a and b) due to the fact
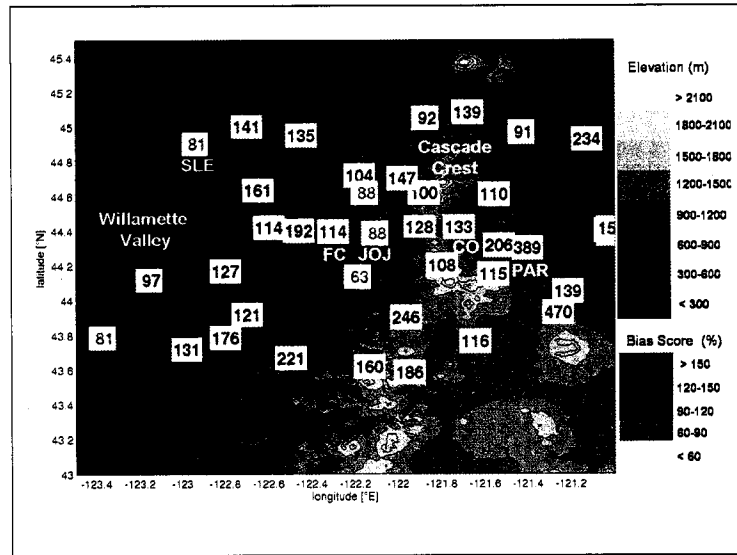
(a)
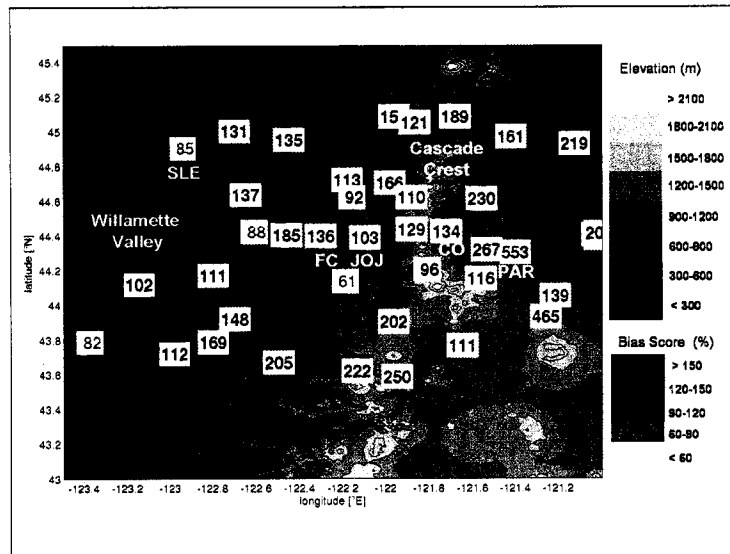
(b)

Figure 5.3: Bias scores for the (a) 4-km and (b) 1.33-km model simulations for 1400 UTC 13 December 2001 through 0800 UTC 14 December 2001.
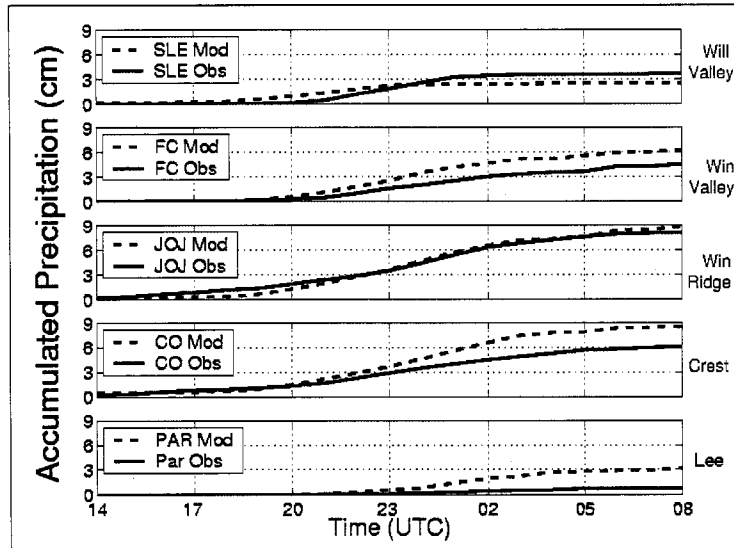
Figure 5.4: Time series of the 1.33-km model forecast and observed hourly accumulated precipitation (cm) at Salem (SLE), Falls Creek (FC), Jump off Joe (JOJ), Corbett (CO) and Parsl site (PAR) from 1400 UTC 13 December 2001 through 0800 UTC 14 December 2001. Locations of precipitation sites are shown in Fig. 5.2.

that the 1.33-km simulation more accurately represented smaller scale mesoscale structures. Yet overall the bias scores were relatively similar, indicating that errors other than resolution may be causing the QPF problems.

Accumulated precipitation at five sites ranging from the Willamette Valley to the lee of the Cascades is shown in Fig. 5.4. The location of the precipitation sites are shown in Fig. 5.2. At SLE in the Willamette Valley slightly more then 3 cm of precipitation accumulated between 1900 UTC 13 December 2001 and 0100 UTC 14 December 2001 during passage of the stratiform precipitation associated with the middle-level front. The model predicted almost 2 cm of precipitation at this location, which was 1 cm less than observed (Fig. 5.4). After 0100 UTC 15 December 2001 in both the observations and model showed post-frontal precipitation accumulations to be small.

Over the windward slopes (FC-windward valley and JOJ -windward ridge) and the crest (CO) of the Cascades, precipitation prior to 1900 UTC was light and predominately the re-

sult of orographic forcing (Woods et al., 2005). The model appeared to accurately represent this small accumulation in precipitation. The observed precipitation rates increased dramatically after 1900 UTC 13 December 2001 as the precipitation band crossed higher terrain. A large overprediction by the model was recorded at CO and FC during this time period. At the windward ridge site, JOJ, precipitation was well simulated. After 0200 UTC 14 December 2001, both the model and observations showed that the precipitation rate decreased as the back edge of the synoptic band passed over the area. An additional spike in the accumulated precipitation was observed at FC between 0500 and 0600 14 December 2001 associated with the passage of the surface frontal precipitation band, which was not resolved by the model.

Along the lee slopes of the Cascades, precipitation shadowing was clearly evident in the observations as less than 0.5 cm of precipitation accumulated at PAR between 2300 UTC December 2001 and 0300 UTC 14 December 2001. The model produced an excess of precipitation, with almost 3 cm of precipitation prior to 0300 UTC 14 December 2001. PAR did not measure any appreciable precipitation with the surface frontal passage at 0630 UTC 14 December 2001, but did indicate a wind shift to westerly and a rise in surface pressure.

5.2 Precipitation Features in Relation to Mountain Waves

The kinematic and reflectivity fields gathered by the airborne Doppler-data coupled with the simulated model microphysics provide an opportunity to explain the variability of the surface precipitation totals seen in Fig 5.2. The analysis in this section will focus on the time-period from 2300-0100 UTC 13-14 December 2001 when precipitation over the study area was the heaviest (cf. Fig 5.4).

5.2.1   Larger-scale (Horizontal Scales >20-km) Precipitation Features

A meridionally averaged E-W cross section of radar reflectivity was constructed from the composite airborne Doppler analysis (Fig. 4.9b,d,f) and is shown in Fig 5.5a. The observed downward slope of the distinct bright-band indicates that the melting layer decreased in height from 2 km over the Willamette valley to just 1.5 km over the elevated terrain, consistent with the presence of cooler air on the windward side of the Cascades. Radar reflectivities decreased rapidly downstream of the crest, suggestive of large evaporation and/or fallout rates. Locally enhanced reflectivity values were observed over the Willamette valley ($\sim$100 km upstream of the crest), the windward foothills (centered $\sim$70 km upstream of the crest), and within a broad area commencing $\sim$44 km upstream of the crest and extending into the lee. These structures are also clearly evident in the composite grid at 3-km (Fig. 4.9b).

To explore the origins of these prominent reflectivity features, model-predicted cloud liquid water (CLW) and snow (q_s) fields were averaged using 15-minute interval data from 2300-0100 UTC 13-14 December 2001 and overlain on the observed radar-observed Doppler reflectivity fields (Fig. 5.5a,b). By comparing these model-based mixing ratios with the Doppler radar observations, the origins of these precipitation structures can be better ascertained. Remarkably, the time-averaged model fields indicated increases in the amount of CLW at 100 and 70 km upstream of the crest, over virtually the same regions where the reflectivity perturbations occurred (Fig. 5.5a). The fact that these perturbations in CLW remain clearly evident even after averaging over a 2-hour period indicates the stationary and persistent nature of these perturbations. Analysis of contemporaneous ground-based radar observations from S-Pol (not shown) also indicates these features were relatively persistent throughout the airborne Doppler analysis period.

Maximum values in the model snow field ($>$ 0.9 g kg^{-1}) extended from 40-km upstream of the crest to the immediate lee, and were collocated with the higher reflectivity values aloft (Fig. 5.5b). These enhanced snow mixing ratios and corresponding reflectivity maxima
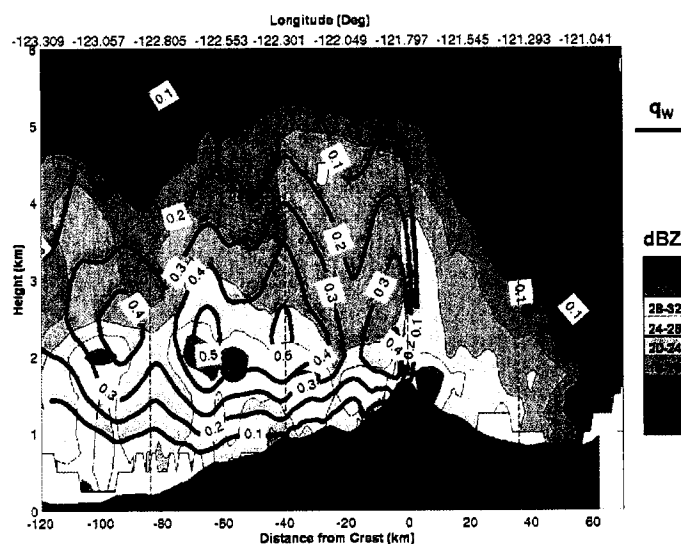
(a)
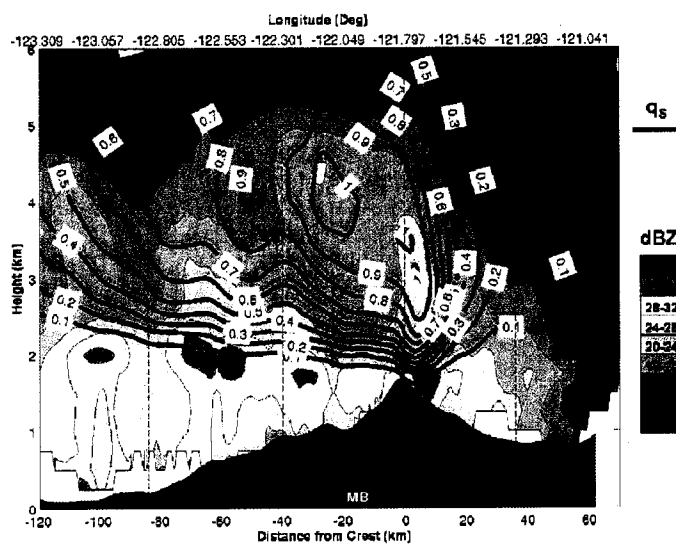
(b)

Figure 5.5: Average E-W cross section of MM5-1.33 km modeled (a) cloud liquid water (CLW) and (b) snow (q_s) in g kg^{-1} overlaid on airborne dual-Doppler derived radar reflectivity (color shading, key right). The modeled CLW and q_s shown were averaged in time from 2300 UTC-0100 UTC 13-14 December 2001 (forecast hours 10-13) using model output at 15 minute intervals.

originated in an area of strong ascent associated with the mountain wave over the crest (cf., Fig. 4.15b). The vertically pointing NOAA/ETL S-band radar (MB in Fig. 2.1), positioned about 20-km upstream of the Cascade-crest, also showed this layer of enhanced reflectivity between 4-5 km that remained relatively stationary over the radar site for the duration of the prefrontal precipitation event (Fig. 6.3). In situ microphysical observations taken by the P3 over the S-band radar site at 0115 UTC 14 December 2001 indicated the presence of newly formed dendrites within this region. These high snow mixing ratios were then advected over the crest by the strong cross-barrier flow before being shunted earthward in the immediate lee of the Cascades (Fig. 5.5b) by the strong downward motion within the deep, vertically-propagating gravity wave. The simulated large gradient of snow mixing ratios in the lee of the Cascades corresponds quite well to the rapid reduction of observed reflectivity values.

To further trace the origins of these observed reflectivity structures, the depictions of the E-W cross section of simulated CLW were expanded westward by 80 km to include the coastal mountains, as shown in Fig. 5.6a. Two additional MM5 1.33-km simulations were also performed, one with the coastal mountains removed (designated as "Noco" in Fig. 5.6c,d), and another employing a lower-resolution version of the topography ("Smooth" in Fig. 5.6e,f). These runs were identical to the control simulation except for the variations in the underlying topography.

Figures 5.6a,b show an enhanced area of CLW and strong upward motion between 180 and 140 km upstream of the Cascade-crest near the coastal mountains. As seen in Fig. 5.6c,d, the strong vertical velocity oscillations apparent between 180 and 140-km (i.e. over the coastal mountain zone) in the control run were predictably absent in the Noco simulation, being replaced by a broad but weaker (0-0.2 ms^{-1}) updraft. Nonetheless, a significant response in the CLW field occurred between 160 and 180-km upstream of the crest, which was likely due to the back edge of the forward titled front (and snow field) consistent with findings of Woods et al. (2005). The lack of observations over this area prevents an independent evaluation of the veracity of this simulated feature.

Doppler dBZ and model CLW   Model W-wind and θ_e

(a)

(b)

(c)

(d)

(e)

(f)
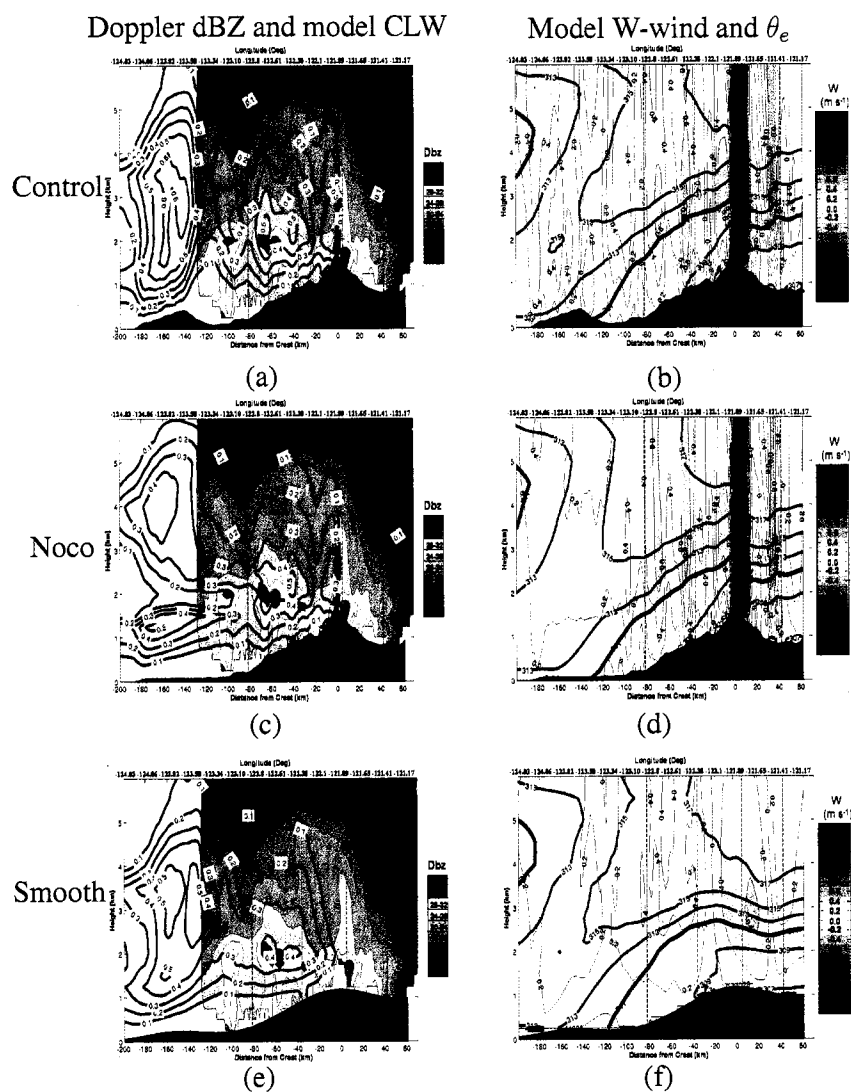
Figure 5.6: Average MM5 E-W cross sections of MM5 cloud liquid water (CLW, g kg^{-1}) overlaid on airborne Doppler reflectivity for three different 1.33-km MM5 simulations; (a) control, (c) no-coastal mountains (Noco) and (e) smoothed terrain (Smooth). Model θ_e overlaid on model vertical velocity for (b) control, (d) no-coastal mountains and (f) smoothed terrain. The modeled fields shown were averaged in time from 2300 UTC-0100 UTC 13-14 December 2001 (forecast hours 10-13) using model output at 15 minute intervals.

An area of descent and reduced model CLW was collocated with the zone of lower re-flectivity values observed in the lee of the coastal mountains (i.e., 120-140 km upstream of the Cascade crest). A significant rebound both in the simulated CLW and observed dBZ fields was evident over the Willamette Valley, centered ~100-km upstream of the Cascade crest collocated with the first rise in the terrain (Fig 5.6a,b). Without the coastal moun-tains, there was an absence of the upward vertical velocity and CLW maximum over the Willamette valley (Fig. 5.6c,d -100-km upstream of crest) when compared to the control simulation. It is also noteworthy that within the the 'Smooth' run, which contains a rudi-mentary representation of the coastal mountains (Fig. 5.6e,f) the enhancement of CLW over the Willamette Valley remained evident. Taken together, these differences indicate the pos-sible presence of a lee wave generated by the coastal mountains that enhanced precipitation over the Willamette Valley.

Over the Cascade foothills, the CLW and vertical velocity fields in the Noco-simulation are almost identical to those in control simulation, indicating that the perturbations in the observed reflectivity fields over these areas cannot be attributed to the coastal mountains (Fig. 5.6c,d). The areas of enhanced model CLW, vertical velocity, and observed reflec-tivity were all collocated with a significant rise in the underlying topography located ap-proximately 70-km upstream from the Cascade crest. The vertical velocity and CLW fields from the smooth-run (Fig. 5.6e,f) were less perturbed than seen in the control simulation (Fig. 5.6a,b). The smoothed-terrain run thus illustrates the sensitivity of windward moun-tain waves and microphysical responses to the local steepness and details of the underlying terrain.

5.2.2 Smaller-scale (Horizontal Scales < 20-km) Precipitation Features

Thus far this chapter has examined the larger-scale (horizontal length scales > 20-km) precipitation perturbations for a meridionally-averaged E-W cross section spanning across the Cascade crest. Yet as the previous chapter indicated, the strong southerly component of flow at low-levels had significant impacts on CLW amounts at smaller scales (< 20 km)

over the complex terrain of the windward slopes.

To illustrate the impact of the vertical perturbations on precipitation processes, Fig.5.7a displays Doppler-derived vertical velocities overlaid on reflectivity along leg-2. Consistently high dBZ values are located near a height of 1.8-km in conjunction with the radar bright band. Shafts of enhanced radar reflectivities extending from the brightband down to the surface repeatedly occurred at distances 5-8 km north (downstream) of strong positive vertical velocities over the windward crests. For example, at a distance of 15-km from the southernmost edge of the cross section and near a height of 2.0-km, a strong vertical velocity maximum ($w > 1.2$ m s^{-1}) is evident where the strong V-component flow impinged upon a 1-km high ridge. At a distance 5-8 km north of this positive vertical velocity perturbation, an enhancement in the dBZ values is observed, implying increased precipitation rates triggered by this ascent.

Model depictions of the precipitation and CLW fields along leg-2 showed the complex microphysical interactions produced by the strong vertical velocity perturbations (Fig. 5.7b). Pockets of high CLW (mixing ratios greater than 0.4 g kg^{-1}) are present over the individual ridges coincident and just upstream of the areas of strong upward vertical velocity. A large snow field above these CLW perturbations is simulated, with some enhancement in the snow mixing ratios appearing above the individual ridges. Where the snow field intersected with the high CLW pockets, riming of the snow particles and graupel formation above the freezing level result. The increased precipitation amounts resulted in an enhancement of the observed bright-band over and immediately leeward of the crests as these particles fell through the melting layer. A corresponding increase in surface precipitation amounts is illustrated by the higher mixing ratios of rain (> 0.4 g kg^{-1}) over the crest and to the immediate lee of several of the ridges along leg-2. The precipitation distribution at the surface was evidently very sensitive to the amount of riming, the fall-speed of the particles, and the phase and amplitude of these small-scale terrain induced waves.
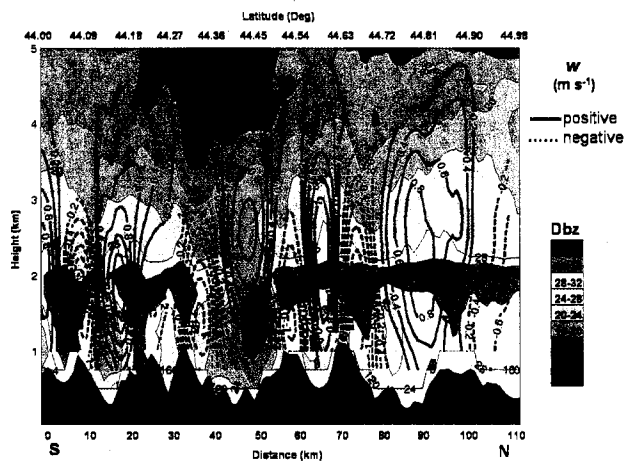
(a)
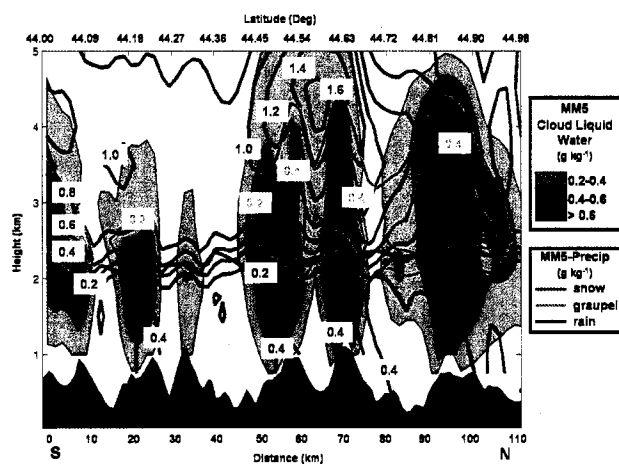
(b)

Figure 5.7: N-S cross-sections along leg 2 of (a) airborne dual-Doppler derived vertical velocity (m s^{-1}) overlaid on reflectivity and (b) contours of modeled snow, graupel, and rain mixing ratios in g kg^{-1}. Shaded regions in (b) denote areas where model-predicted CLW mixing ratios exceeded 0.2 g kg^{-1}.

5.2.3 Surface Precipitation Patterns

To further assess the impact that the mountain waves and associated microphysical processes had on precipitation at the surface, the 1.33-km control simulation's 3-hour QPF for 2200-0100 UTC 13-14 December 2001 is presented in Fig. 5.8a, while a 1.33-km smoothed terrain simulation's QPF for the same 3-hour period is shown in Fig 5.8b. The terrain used for the smoothed 1.33-km model simulation is identical to that used in the 12-km outer domain. By smoothing the terrain and keeping the grid-spacing of both simulations at 1.33-km, variations in precipitation amounts can be attributed to the differences in terrain, not model grid resolution.

The control simulation shows distinct regions of higher precipitation along the coastal mountains at the western edge of the domain, while over the the relatively flat Willamette Valley amounts are reduced and more uniform (Fig. 5.8a). Over the windward slopes of the Cascades, significant precipitation variations are simulated, with totals ranging from > 3.0 cm over the local crests to 1-1.5 cm in some of the windward valleys (Fig 5.8a). The smoothed terrain simulation shows a much broader spatial distribution of precipitation over the windward slopes, with precipitation totals consistently near 1.5-2 cm (Fig 5.8b). A slight reduction in the precipitation is evident 10-20 km upwind of the crest in both the control and smoothed simulations, while in the immediate lee precipitation totals are in excess of 3-cm for the control simulation and 2.5-3-cm for the smoothed simulation. Both model runs showed significant drop-offs in precipitation amounts farther to the lee, with a stronger gradient appearing in the control simulation.

To highlight the differences in the precipitation distributions for these runs, a meridionally averaged E-W cross section of QPF was calculated for the smoothed-terrain and control simulations (Fig. 5.9a). Despite the significant differences in the detailed horizontal distributions of precipitation for these two simulations, integrating precipitation amounts over the entire E-W cross-section resulted in total precipitation amounts that were very similar: 294 cm for the control simulation and 289 cm for the smoothed simulation. This indicates
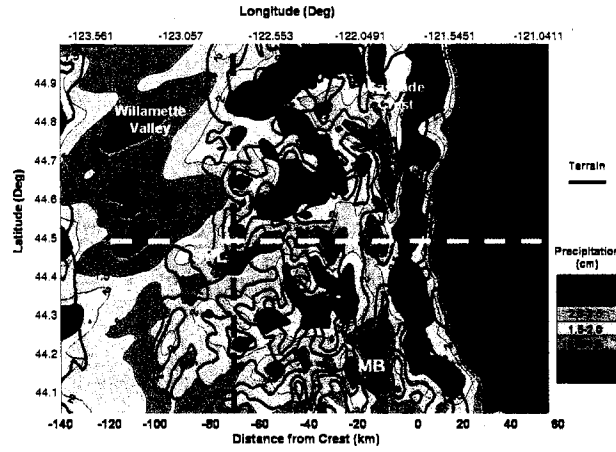
(a)
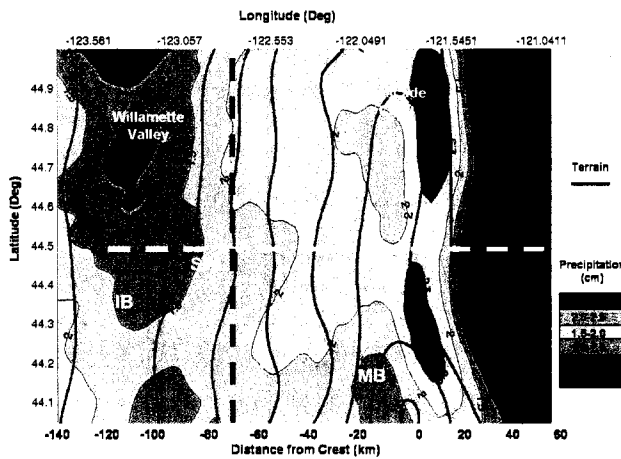
(b)

Figure 5.8: (a) Modeled accumulated precipitation (color shading, key at right) and terrain elevation (black contours at intervals of 250 m) for the 1.33 km resolution MM5 control simulation and (b) for the smoothed terrain version of the 1.33 km resolution MM5 simulation. Black dashed lines in (a) and (b) indicate the position of leg-2 of the P3 flight track and cross section in Fig. 5.9b. White dashed lines represent the orientation of the meridionally averaged E-W cross section displayed in Fig. 5.9a.

that for the three-hour period, the differences in topography did not significantly alter the total amount of precipitation over the domain as a whole, but instead horizontally redistributed this precipitation.

A significant difference in precipitation totals for the two simulations was evident over the windward slopes between 100 and 20 km upstream of the crest, where the control simulation's meridionally averaged precipitation totals were 4-17% higher than those in the smoothed simulation. Integrating over the windward slope region (area delimited in Fig. 5.9a), a 7% increase was observed in the control's precipitation amount when compared with the smoothed terrain simulation.

A S-N cross section of the 3-hour QPF along leg-2 (black dashed-line in Fig. 5.8a,b) as derived from both the control and smoothed simulations is displayed in Fig 5.9b. The control simulation shows significant local variations in QPF, with higher totals over the ridges and lower QPF within the valleys. These precipitation extremes correspond closely to the variations in mixing ratios and Doppler reflectivities seen in Fig 5.7. The smoothed simulation's QPF pattern is much broader since the simulation failed did not produce the smaller scale wave perturbations caused by the complex terrain. When integrating the QPF along leg-2, the accumulated precipitation total for the control simulation was 171 cm, as compared to the smoothed-terrain run's total of 161 cm. This represents a 6% increase in precipitation amounts, which ignoring any large-scale differences in the kinematic fields between the two simulations, may be attributed to the small-scale terrain induced waves and ensuing microphysical processes.

Another interesting feature of the precipitation distribution is the reduction in totals near the crest and the increase to the immediate lee in the control simulation (Fig.5.9a). The reduced precipitation amounts at the crest and increase at the lee are apparently caused by the strong mountain wave and associated acceleration of the cross-barrier flow over the crest that acted to advect precipitation toward the lee-slopes instead of depositing the precipitation over the crest. Although the increased QPF over the lee is within the area where the MM5 simulated the strong U-flow reaching closer to the surface than observed, the QPF
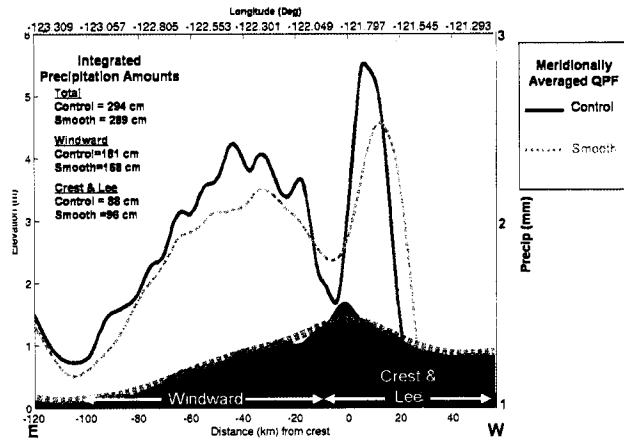
(a)
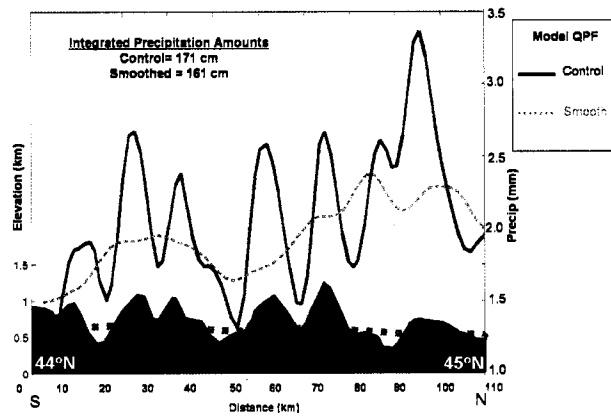
(b)

Figure 5.9: (a) E-W cross section of meridionally averaged QPF from 2200 UTC-0100 UTC 13-14 December 2001 from the control simulation (solid black line) and smoothed run (dashed-gray line) with underlying terrain of the control simulation (black-filled area) and smoothed terrain (thick gray dashed line). Orientation of the cross section is shown by the white dashed line in Fig. 5.8. (b) Same as (a) but with QPF and underlying terrain displayed for the S-N oriented cross-section along leg 2 of the P3 track (cf. Fig. 2.1a). Orientation of cross-section is shown by black dashed line in Fig. 5.8. Thick dashed gray line delineates the mean terrain profile for the smoothed terrain simulation.

minimum near the crest and maximum to the lee is consistent with the Doppler-reflectivity patterns (and model snow mixing ratios) described in Fig. 5.5b. The smoothed run showed a similar pattern in the surface precipitation, with a lessened contrast in precipitation between the crest and the lee (Fig. 5.8b and Fig. 5.9a). This may be due to the wave amplitude near the crest within the smoothed run being less than the control simulation (Fig. 5.6b,f), possibly resulting in reduced precipitation spill-over to the lee. Due to the lack of detailed surface observations with sufficient temporal resolution surrounding the Cascade crest, a detailed verification of this precipitation distribution cannot be performed. Yet an examination of observed precipitation amounts from 1400-0800 UTC 13-14 December 2001 (Fig 5.2) does indicate some tendency for a reduced precipitation totals near the crest as compared to those over the windward slopes and in the immediate lee.

To illustrate the importance of the terrain resolution during the entire duration of the 13-14 December event, Fig. 5.10a shows a E-W cross section of the meridionally average QPF from 1400 UTC-0800 UTC 13-14 December 2001. This extended time period includes prefrontal, frontal, and postfrontal precipitation regimes, and previously compared against observations in Fig 5.3. The integrated precipitation amount over the entire cross section showed a net increase of 8% in the control (987 cm) versus the smoothed simulations (911 cm). This percentage increase in the integrated precipitation amounts differs from that computed for the 3-hour prefrontal period, in which integrated precipitation amounts were roughly equal for both the smoothed and control simulations. Therefore the effect of the increased terrain resolution on precipitation distributions and amounts is most likely sensitive to the thermodynamic and flow properties of the upstream flow. Moreover relatively shallow precipitating features characteristic of post-frontal regimes might be expected to be more sensitive to details of the underlying topography.

Over the windward slopes, the model found a 12 % increase in the control simulation's integrated precipitation (585 cm) versus the smoothed terrain experiment (518 cm), while over the crest and lee minimal differences in the integrated precipitation amounts were seen (322 cm versus 320 cm). Increased precipitation amounts over the windward slopes

82

appear to be tied to the presence of the smaller-scale wave perturbations. For example, along a N-S section (leg-2) the QPF within the control simulation is 17% greater than that in the smoothed terrain simulation (551 cm verse 471 cm) over the entire 18 hour period, indicating the robustness and persistence of the small-scale perturbations identified during leg-2 (Fig. 5.10b). The model's meridionally-averaged precipitation for the period from 1400 UTC-0800 UTC 13-14 December 2001 also exhibited a relative minimum in precipitation at the crest and relative maximum to the lee, but with much less amplitude than found during the 3-hour period from 2200 UTC-0100 UTC when cross-barrier flow speeds and moisture transport were near their maximum. (Fig. 5.10a). The reduced difference between the crest and lee QPF values is consistent with model and observational evidence indicating the mountain wave was strongest from 2300-0100-UTC, resulting in a period of increased spillover of precipitation into the lee compared to fallout over the crest during that 3-hour time period.

5.3 Summary and Conclusions

An examination of simulated precipitation for the 4-km and 1.33-km MM5 simulations, indicated the model was able to predict accurately the precipitation totals over the coast and Willamette Valley. In contrast, over the lee slopes of the Cascades, numerous sites experienced a substantial overprediction with bias scores of greater than 150 percent. The precipitation sites over the windward slopes showed substantial variations in the bias scores with many but not all sites experiencing significant overprediction. A time series of precipitation totals at various sites show the errors were most profound during the passage of the mid-level baroclinic zone when precipitation was the most intense.

An average E-W cross section of reflectivity was constructed from the composited airborne Doppler data to more comprehensively examine precipitation fields over the Oregon Cascades and relate them to the precipitation distributions. A strong Föehnwall-like gradient in the reflectivity was identified over the lee slope of the barrier, with radar reflectivity decreasing rapidly with distance downstream from the crest. Over the windward slopes,
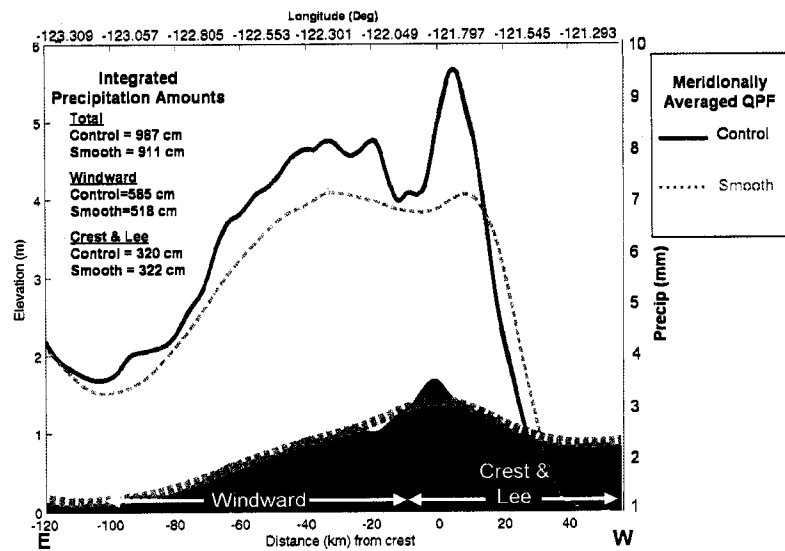
(a)
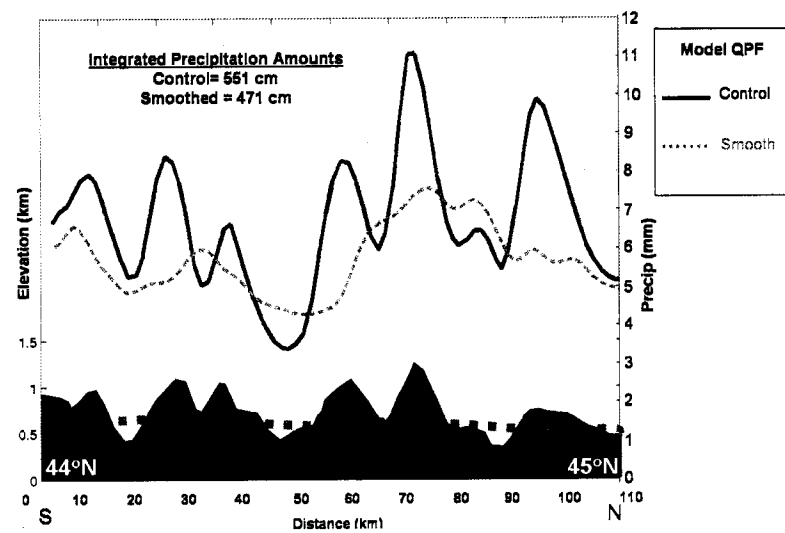
(b)

Figure 5.10: As in Fig 5.9 but over the extended interval 1400 UTC- 13 December - 0800 UTC 14 December 2001.

perturbations in the precipitation intensity were clearly evident within three distinct areas marked by higher reflectivity values: one located over the Willamette valley ($\sim$100-km up-stream of the crest), a second over the windward foothills (centered $\sim$70-km upstream of the crest) and a third larger area of enhanced reflectivity commencing $\sim$40-km upstream of the mean crest and extending into the lee.

To determine the origin and stationary nature of these perturbations, model-predicted microphysical fields were used for comparison with the observed reflectivity. Experiments were also performed to determine the effects of the coastal mountains and terrain resolution on the reflectivity and precipitation patterns over the upstream areas. It was demonstrated that without the coastal mountains (Noco) the modeled CLW maximum centered at 100-km upstream of the crest over the Willamette valley was absent compared to the control simulation. This difference between the Noco and control runs suggest the presence of a lee-wave produced by the coastal mountains, which enhanced precipitation over the Willamette Valley. A smoothed-terrain simulation clearly illustrated the sensitivity of the windward mountain waves and microphysical responses to the steepness of the underlying terrain.

Collocated with the higher reflectivity values over the Cascade-crest, simulated maximum snow mixing ratios (> 0.9 g kg^{-1}) extended from 40-km upstream of the crest to the immediate lee. The enhanced snow mixing ratios and observed reflectivities originated in an area of dendritic growth and strong vertical ascent associated with the the mountain wave over the mean crest. The high snow mixing ratios were subsequently advected beyond (i.e., east) the barrier in the strong cross-barrier flow before being dumped to the immediate lee of the Cascades by the strong downward motion within a high amplitude mountain-induced gravity wave. This precipitation signal resulted in reduced modeled precipitation amounts near the crest and an area of markedly enhanced precipitation amounts in the immediate lee. Although this precipitation distribution could not be extensively verified, an examination of precipitation amounts from 1400-0800 UTC 13-14 December 2001 (cf. Fig 5.2) did indicate some tendency for a reduced precipitation totals near the crest versus over the

windward slopes and immediate lee. The strong gradient in snow mixing ratio to the lee of the Cascades was in very close agreement with an observed reduction of radar reflectivity values. Yet despite this agreement, a significant tendency for overprediction was seen in the model bias scores to the lee of the Cascade crest.

On smaller horizontal scales (< 20 km), significant perturbations in vertical velocity were present over the foothills as the strong low-level V-component flow interacted with the complex terrain of the windward slopes. These perturbations were shown to be responsible for the significant variations in precipitation totals over the windward slopes of the Cascades. Model depictions of the precipitation and CLW fields over leg-2 of the P3 flight-track showed the complex microphysical interactions produced by the strong vertical velocity perturbations. Pockets of high CLW were present over the individual ridges coincident or just downwind of the areas of strong upward vertical velocity. Where the upper level-snow field intersected with the high CLW pockets, riming of the snow particles and graupel formation above the freezing level was simulated by the model. The increased precipitation mass resulted in the enhancement of the bright-band over the crest as the particles fell through the melting layer. The increase in precipitation amounts was illustrated by the higher mixing ratios of rain over the crest and to the immediate lee of several of the ridges. The precipitation distribution at the surface was therefore very sensitive to the amount of riming, the fallspeed of the particles, and the phase and amplitude of the small-scale waves.

An analysis of the model QPF between 2200-0100 UTC showed the small-scale waves increased the modeled precipitation amounts over the windward slopes by 4-14% over a smoothed terrain model simulation. Yet during this same 3-hour period, the smoothed terrain resolution did not significantly alter the total amount of precipitation over the domain, but instead redistributed the precipitation in different areas. When a longer 18-hour period, which included prefrontal, frontal, and postfrontal precipitation regimes, was considered the control simulation's total precipitation amount over the windward slopes showed a net increase of 12% over the smoothed simulation. This increase appeared to be directly tied to an increase in precipitation over the windward slopes caused by the smaller-scale wave

perturbations.

Chapter 6

VERIFICATION OF SIMULATED MICROPHYSICS

This chapter compares in situ observations of cloud microphysical parameters with the MM5 simulated microphysical fields for a 3-hour period of heavy prefrontal precipitation during 13-14 December 2001 storm system. The MM5 simulation used the Reisner-2 microphysical parameterization which contains prognostic equations for cloud water, rain, snow, graupel, cloud ice, water vapor, and the number concentration of cloud ice. Errors in the processes and assumptions of the model BMP are evaluated against the extensive observational data-set and linked to the QPF errors presented in Chapter 5.

6.1 Description of the Bulk Microphysical Parameterization (BMP)

Presently, high-resolution operational forecast models including the MM5 employ bulk microphysical parameterizations (BMPs) in which mass concentrations of the hydrometeor species are predicted and exponential or gamma size distributions are assumed. BMPs differ from bin or explicit models, which include prognostic equations for specific intervals of each hydrometeor size spectrum (Houze, 1993). Although the explicit models are more realistic and allow the size distributions of the hydrometeors to evolve 'naturally' they are also computationally expensive and are not yet viable for real-time forecasts and may not produce realistic precipitation distributions.

Many mesoscale numerical models (including the MM5) offer a choice of BMPs, including warm rain schemes containing only cloud and rain water processes (Fig. 6.1a) (Hsie et al., 1984), and simple ice schemes, which include snow and ice processes, but do not allow for super-cooled water (Fig. 6.1b) (Dudhia, 1989). Over the past decade more advanced BMPs were adapted from cloud models for use in the MM5. These schemes

contain riming processes, super-cooled CLW and graupel (Fig. 6.1c) (Reisner et al., 1998; Thompson et al., 2004). The majority of these BMPs are based upon studies performed over 20 years ago (Lin et al., 1983; Rutledge and Hobbs, 1983, 1984). More recently, double moment schemes, which predict the number concentrations and mixing ratios of certain microphysical species have been developed (Ferrier, 1994).

For the MM5 simulations presented here, the Reisner2 BMP was chosen. It contains prognostic equations for cloud water, rain, snow, graupel, cloud ice, water vapor, and the number concentration of cloud ice (Reisner et al., 1998). The scheme is the most complex microphysics package available to the to the MM5 community with upwards of 30 microphysical processes (Fig. 6.2).The Reisner-2 scheme has recently been updated in previous studies (Thompson et al., 2004) and is presently being used for real time simulations at a variety of institutions, including the University of Washington.

6.2 Methodology

The microphysical analysis presented here focuses on the deep stratiform precipitation band that crossed the study area between 2200 UTC 13 December and 0130 UTC 14 December 2001. The stratiform precipitation was associated with synoptic-scale lifting ahead of and within a middle-level baroclinic zone that interacted with low-level orographic forcing to produce heavy precipitation over the elevated terrain of the Cascades. A deep ice-generating altostratus cloud, which extended up to 8-9 km, dominated the upper levels of the 300-km-wide precipitation band associated with the synoptic baroclinic zone. At lower levels, strong southwest flow that impinged on the elevated terrain of the Oregon Cascades resulted in stratocumulus clouds above the mountain barrier that extended up to the base of the upper altostratus deck (Woods et al., 2005). The combination of a synoptically-forced precipitation band and low-level orographic cloud provides an environment conducive to examine the cloud microphysical processes leading to heavy precipitation over the mountains.
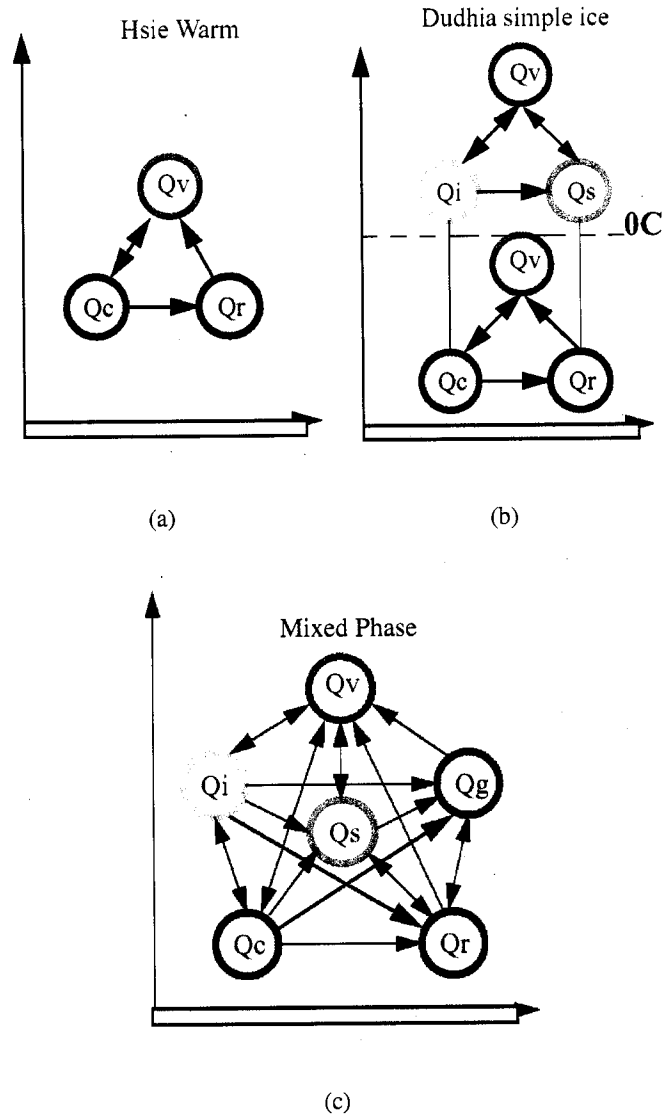
Figure 6.1: Microphysical flowchart for (a) warm rain scheme, (b) simple ice scheme and (c) mixed phase scheme. The circles represent the various water species (water vapor, cloud water, cloud ice, rain, snow, and graupel), and the arrows are the processes that link the species.

Figure 6.2: Microphysical flowchart for the Reisner2 scheme. The circles represent the various water species (water vapor, cloud water, cloud ice, rain, snow, and graupel), and the arrows are the processes that link the species (see Colle and Zeng 2004a for the list of processes.

Woods et al. (2005) showed that the December 13-14 event was different than previous storms systems studied over the Washington Cascades. During the Cascade Project (Hobbs, 1975), storm systems were often characterized by prefrontal low-level easterly flow across the Cascade crest, which inhibited the formation of low-level cloud liquid water (CLW) on the western slopes. In the December 13-14 event over the Oregon Cascades, strong westerly flow persisted throughout the storm with high CLW at low levels and significant amounts of graupel and rimed snow.

A time-height cross-section of vertically pointing S-band radar reflectivity (the location of the radar is denoted by SB in Fig. 2.1) between 2200 UTC 13 December 2001 and 0130 UTC 14 December shows the steady-state and deep nature of the stratiform precipitation band (Fig. 6.3). The S-band image shows reflectivity values > 16 dBZ mainly below 5 km, a well-defined bright band just below 2 km, and some tops reaching 7-8 km. A secondary region of high reflectivity was present between 4-5 km, which was coincident with strong

Figure 6.3: Time-height cross section of reflectivity from the vertically pointing S-band radar (located at SB in Fig. 2.1) from 2200 UTC 13 December through 0130 UTC 14 December 2001.

vertical velocity associated with the vertically propagating mountain wave along the crest as discussed in Chapter 5. During this time period, the wind field was relatively steady-state, with strong (30-40 m s^{-1}) southwesterly flow below 4 km (Fig. 4.3). The relatively steady-state precipitation and low-level wind fields simplified the microphysical analysis and the comparisons of model outputs with observations by reducing complications associated with transient features.

Between 2300-0140 UTC 13-14 December 2001, the Convair-580 and NOAA P-3 measured a variety of basic state parameters and microphysical data including temperature, humidity, wind speed, CLW, ice particle imagery, and ice crystal concentrations throughout the study area. The UW Convair-580 flew multiple vertically-stacked flight legs and gathered microphysical data at a number of altitudes, thereby providing detailed depictions of cloud and precipitation growth within the storm. Three Convair flight legs were flown in the upper levels of the stratiform precipitation band (Fig. 2.1 and Fig. 6.4), and were used to deduce ice microphysical processes in the altostratus cloud. The P-3 also performed a cross-mountain transect at minimum allowable altitudes, providing detailed measurements

92

Convair Leg 1

Leg 1d

Convair Leg 2

Leg 2d

Convair Leg 3

P3 Win1   P3 Lee

P3 Win2

Pressure (hPa)

400
500
600
700
800
900
1000

0 10 20 30 40 50 60 70 80 90 100 110 120 130 140 150 160 170 180 190

A

Distance (km)

B
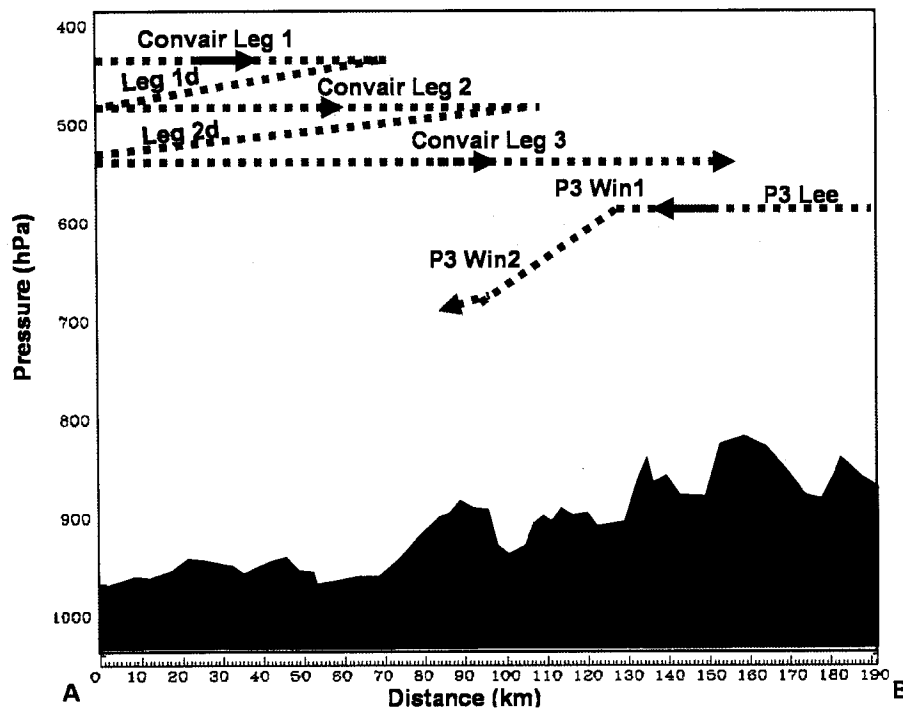
Figure 6.4: Convair and P3 flight tracks plotted in a southwest to northeast cross section from point A to point B shown in Fig. 2.1.

in the lee of the mountain ("Lee" in Fig. 6.4), above the windward slopes ("Win1" in Fig. 6.4), and above the windward foothills (Win2 in Fig. 6.4). In this chapter we will compare the microphysical measurements collected by the two aircraft with those from the 1.33 km MM5 simulations. For comparisons with the observations, the model results presented in this paper were averaged between 2200 UTC 13 December 2001 and 0100 UTC 14 December 2001.

6.3 Comparisons of Observed Hydrometeor Fields and Precipitation Growth Mechanisms with Model Simulations.

The UW Convair-580 and NOAA P-3 aircraft provided 2-D ice particle imagery at both the upper and lower levels of the stratiform precipitation band associated with the middle-level

front. These images provided information on the formation and growth of precipitation particles, and enabled deductions of the amounts of precipitation growth between the various flight levels (see Woods et al. (2005) for a complete description of the flight-level microphysical data). In this section, we compare the observed major precipitation growth mechanisms and hydrometeor fields in the stratiform precipitation band discussed by Woods et al. (2005) with the corresponding model results.

Figure 6.5 presents the observed and modeled distributions of the predominant hydrometeor types and major precipitation production processes for the 13-14 December 2001 event as the stratiform precipitation band passed over the Oregon Cascade Mountains. The cross-section includes the location of the top three legs of the UW Convair-580 flight, which flew from 2315 UTC 13 December 2001 through 0100 UTC 14 December 2001 and closely paralleled the prevailing southwest flow (see Fig. 2.1 for a plan view of the flight pattern). The P-3 flew a similarly orientated northeast-southwest pattern from 0056 through 0128 UTC 14 December 2001 at lower altitudes (Fig. 6.4). While the direct comparison of in-situ observations with the model-derived fields is limited to the locations of the two aircraft, the simultaneous flight missions at different altitudes greatly enhances the opportunity to diagnose the modeled microphysical fields.

Figure 6.5a shows the modeled snow, graupel, rainwater, and cloud liquid water fields, while Fig. 6.5c shows the same hydrometeor fields based on measurements from the two research aircraft and ground-based measurements. Woods et al. (2005) described the techniques used for computing in-situ particle mass concentrations along the Convair-580 and NOAA P-3 flight legs, and the identification methodology for the hydrometeor species at flight and ground level. The ice crystal imagery revealed cold-type crystals (i.e., images consistent with particle habits of assemblages of sectors, sideplanes and plates) along the Convair-580 flight legs. The model replicated quite closely the expansive snow field aloft and upwind of the Cascade Mountains along the Convair flight track (Fig 6.5a). The P-3 data showed a region between 600-700 hPa where a mixture of cold-type crystals from aloft, dendrites that form near the -15°C level, and rimed snow and graupel were present.

94

(a)

(b)

(c)
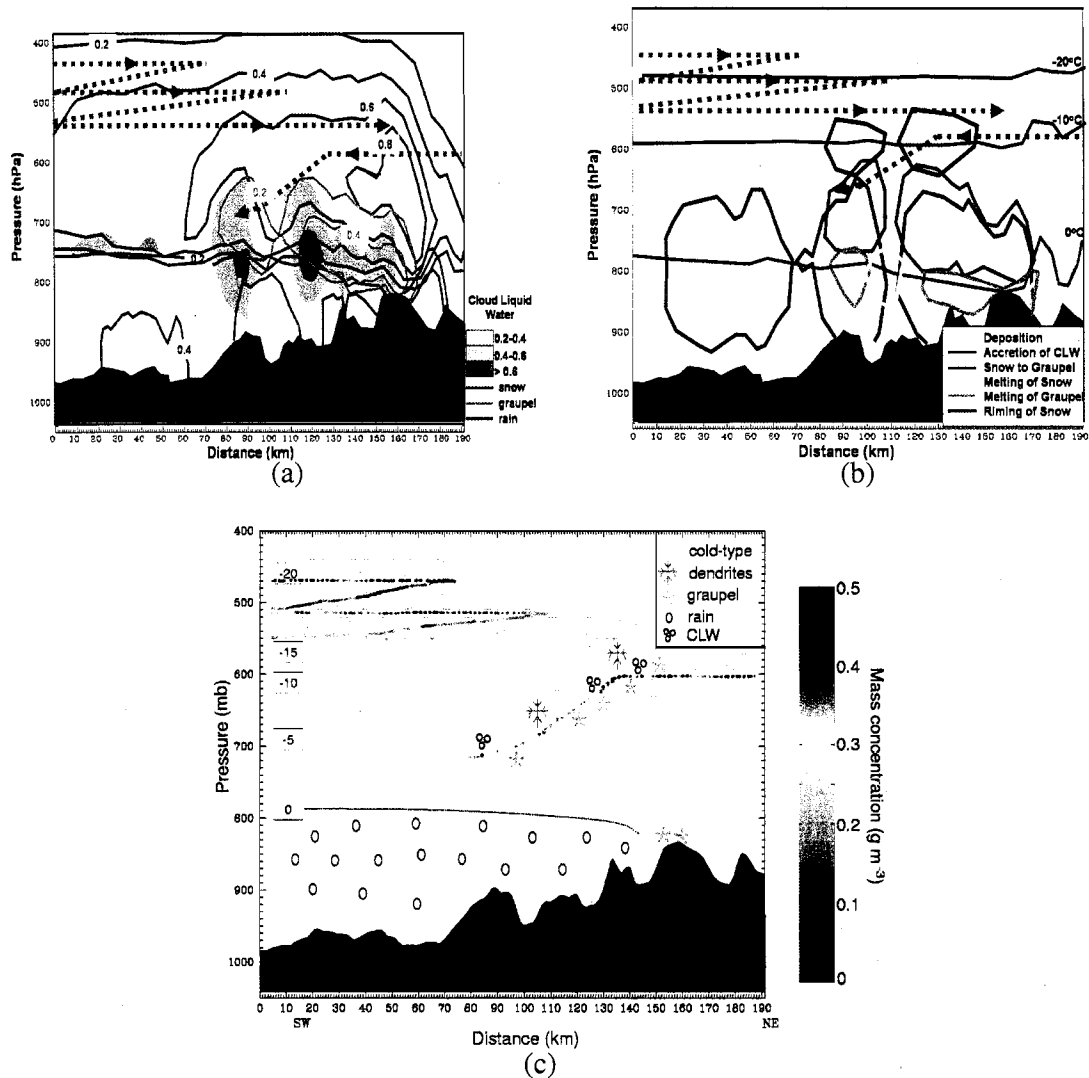
Figure 6.5: Comparison of model-derived versus measured precipitation species and pro-
cesses along the cross section shown in Figure 6.4. (a) Modeled mass concentrations (g
m^{-3}) of snow (blue lines), graupel (green lines), rain (red lines) and cloud liquid water
(gray shading). Convair-580 and P-3 flight legs are indicated by brown dashed lines. (b)
Modeled deposition of snow (light blue lines), riming of snow (purple lines), conversion of
snow to graupel (green lines), melting of snow (yellow lines), melting of graupel (orange
lines) and accretion of cloud water by rain (red lines). Contours indicate areas where each
model process dominates. Temperatures in $^{\circ}$C are by black lines. (c) In-situ observations
of cold type crystals of snow, dendrites, graupel, supercooled cloud liquid water, and rain
are depicted by symbols. Flight level ice particle mass concentrations (g m^{-3}) are also
shown by colored shading along the various flight legs. Temperatures in $^{\circ}$C are indicated at
various discrete levels.

Particle mass concentrations (shown in Fig. 6.5c) were calculated using the in-situ obser-
vations of ice crystal types [classified according to the scheme given by Magono and Lee
(1966)], and size distributions in conjunction with the relationships between masses and
diameters of various crystal types given by Brown (1970), Locatelli and Hobbs (1974), and
Varley (1980) [refer to Table 4 of Woods et al. (2005) for the specific relationships used].
The results showed marked increases (in some cases a factor of two) in the mass concentra-
tions of particles between the Convair legs at higher altitudes and portions of the lower-level
P-3 flight legs. The maximum observed particle mass concentration, which approached 0.5
g m^{-3}, occurred upwind and over the Cascade crest at $\sim$600 hPa, in a region where graupel
was observed. Densely rimed snow and graupel extended to the surface along the mountain
crest (Fig. 6.5c).

The model indicated the presence of graupel along the lower reaches of the P-3 flight
track between 650 and 800 hPa (Fig. 6.5a), which was confirmed by the observations. How-
ever, the absence of significant amounts of graupel (> 0.20 g m^{-3}) immediately upwind and
over the Cascade crest (around 610 hPa) in the model simulation reveals a significant prob-
lem in the simulation. Instead of graupel, the model produced an extensive region of snow,
with mixing ratios >0.80 g m^{-3} (compared to the total maximum observed value of 0.5 g
m^{-3}). A quantitative comparison of the observed and modeled mass concentrations along
the P-3 flight track will be provided in Section 6.5 .

Figure 6.5b is a schematic of the major precipitation growth processes simulated by the
model along the P3 and Convair flight tracks. Figure 6.5b only identifies the areas of the
dominant modeled precipitation processes along the cross section. A more detailed and
quantitative discussion of the model precipitation processes is found in the next section.
It was found that only small amounts of simulated cloud ice mass concentration existed
in areas below 400 hPa, which was confirmed by observations (Woods et al., 2005) and
therefore is not included in the comparisons. Figure 6.5b shows that in the model run,
deposition of water vapor to snow was the predominant growth process between 400 and
700 hPa. Aircraft data collected within this layer showed cold-type crystals, unrimed plates,

and dendrites, which verifies the importance of growth by deposition (Fig. 6.5c).

Between 600-650 hPa, along and just upwind of the crest, the predominant growth process in the model was deposition of water vapor to snow and riming of snow. This differs from the observations along the P-3 flight track, which show that graupel was present at 600-650 hPa. In the model, the initial generation of graupel is determined primarily by the snow-to-graupel autoconversion term, which is initiated when the amount of riming exceeds depositional growth by a factor of 2.5 (Thompson et al., 2004).

The definition of snow versus graupel in the model has important implications on where the precipitation species falls out. The fall speed of snow in the model is based upon the Rutledge and Hobbs (1983) expression, which was derived for unrimed radiating assemblages of plates, side planes, bullets, and columns (Locatelli and Hobbs, 1974) and does not take into account any effects of riming. In the model, graupel has a significantly larger fall speed than snow (Locatelli and Hobbs, 1974), and therefore falls out much more quickly. The simulated strong winds during the 13-14 December case advected much of the snow produced by the model over the barrier, which would have otherwise fallen out on the windward side if it had been defined as graupel. At lower levels between 650-850 hPa, the model indicated that the conversion of snow to graupel and melting of graupel are important especially along the upper ridges of the windward slopes. Melting of snow was present in the valley sites and in the lee of the Cascade Crest where snow from aloft was advected downward in gravity waves. The next chapter further explores the impacts of differences in the parameterizations of particle fall speeds and what is defined as graupel versus snow.

In addition to these processes, the accretion of cloud water by rain was important to the overall precipitation budget in the model along the lower windward slopes of the Cascades below the freezing level. This is seen in Fig. 6.5a where the rainwater mixing ratios are increased by a factor of 2 from 0.2 to 0.4 g m^{-3} in areas where accretion of CLW by rain is present. As described in the next section, comprehensive CLW measurements from both aircraft, as well as from an NCAR ground-based, vertically-pointing radiometer, permit further investigation of the temporal and spatial variations of CLW.

6.4 Cloud Liquid Water

In this section we compare the modeled and measured CLW for the P-3 flight in the lower levels of the precipitation shield, which were most strongly influenced by orographic forcing. We will also compare vertically-integrated cloud liquid water depth (LWD) from the ground based radiometer just west of the Cascade crest with the modeled column-integrated LWD to evaluate temporal variations in CLW during the passage of the storm.

Figure 6.6 shows a time series of observed CLW and vertical air velocity measurements along the P-3 flight track from 2302 UTC 13 December to 0128 UTC 14 December 2001. The vertical velocities were derived from accelerometer measurements. The CLW measurements were obtained from a PMS Commonwealth Scientific and Industrial Organization (CSIRO) King probe (King et al., 1978) and a Johnson-Williams (J-W) probe (Baumgardner, 1983). The CLW measurements from the two probes were in close agreement, and thus provide confidence in the in-situ measurements. Figure 6.7 shows the CLW measured by the King probe and the modeled CLW averaged along each of the five north-south flight legs of the P-3. A 15% error bar is placed on the observed CLW measurements to account for possible errors in the measurements of the King probe (King et al., 1985).

The first P-3 leg was flown at a altitude of 2 km above the relatively flat terrain of the Willamette Valley. Along this flight leg, temperatures were about 2°C [see Fig. 4.6] and vertical velocities were < 150 cm s^{-1}. Cloud liquid water measurements varied between 0-0.3 g m^{-3}, with an average along the leg of 0.15 g m^{-3}. Both the 4-km and 1.33-km resolution model simulations predicted an average CLW of 0.25 g m^{-3} along the flight leg (Fig. 6.7) and thus appeared to modestly overpredict CLW.

As shown in Fig. 6.6, variations in the vertical velocity were most pronounced during the second P-3 leg, which was flown at 2.5 km over the windward Cascades slopes. The largest CLW values, which approached 0.5 g m^{-3}, were measured along this leg, with temperatures ranging between -1 and -2 °C. Figure 6.7 shows that the 1.33-km resolution simulation overpredicted the amount of CLW by almost a factor of two over the windward
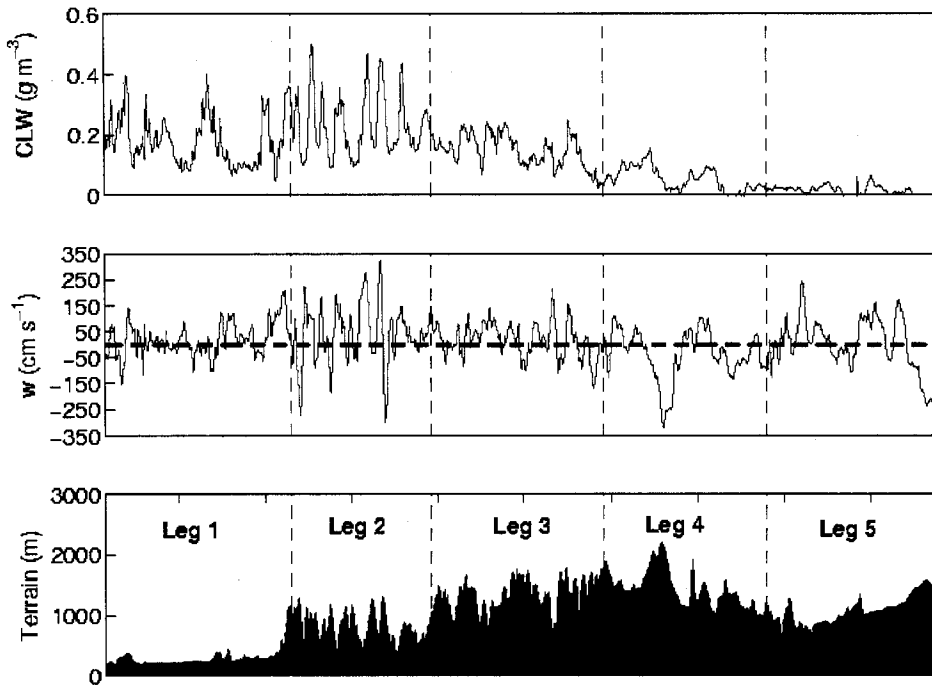
Figure 6.6: In-situ measurements of cloud liquid water (CLW) and vertical velocity (w) along five legs of the P-3 flight track from 2302 UTC 13 December 2001 through 0100 UTC 14 December 2001. The last panel shows the elevation of the underlying terrain in meters. The vertical dashed lines separate the different N-S legs that were flown.

Cascade slopes. However, the 4-km resolution model simulation more accurately reproduced the measured CLW, with a leg average value of 0.25 g m^{-3}.

A north-south cross-section of CLW, vertical velocity, and underlying terrain for leg 2 is shown in Fig. 6.8. As discussed in Chapter 4 large upward vertical velocities occurred where strong low-level southerly winds impinged on the higher terrain of the Cascade foothills. Measurements along leg 2 indicated that the CLW amounts were closely related to the variations in vertical velocity, with areas of high (low) CLW coinciding with or just downwind of upward (downward) vertical air motions. In several areas along this leg, the 1.33-km resolution simulation appeared to depict correctly the perturbations in
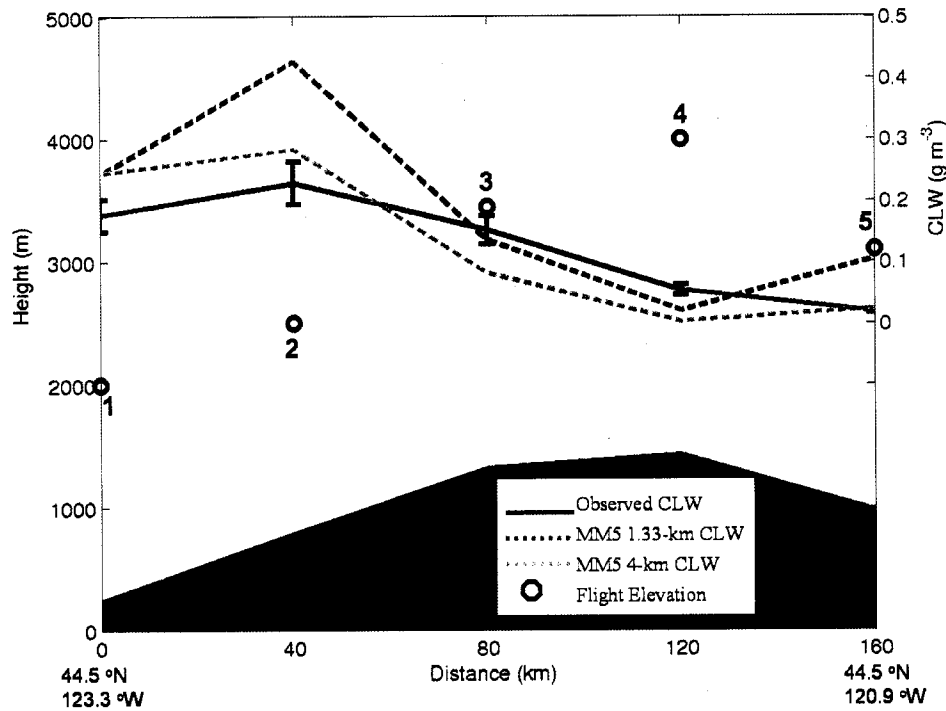
Figure 6.7: Cloud liquid water content (CLW) in g m^{-3} averaged for each of the five P-3 legs. The solid blue line is the observed CLW with error bars, the dashed red line is the 1.33-km resolution MM5 CLW, and the dashed green line is the 4-km resolution MM5 CLW. The black circles show the height of the P-3 aircraft along each of the legs. The averaged underlying terrain is shown shaded in dark blue.

vertical air motion yet it drastically overpredicted the amount of CLW; this suggests the possibility that the model parameterization was unable to transfer CLW to precipitation particles as rapidly as occurred in reality. The 4-km resolution model run better simulated the amount of CLW, but underpredicted the amplitude of the vertical velocity forcing.

Leg 3 of the P-3 track was flown at a height of 3.5 km about 20 km west of the Cascade crest. Substantial variations in vertical velocity and CLW were measured, although the amplitudes of the fluctuations were much less than for leg 2 (Fig. 6.6). The 1.33-km resolution model run accurately predicted the CLW along the crest, with average values of $\sim$0.13 g m^{-3} (Fig. 6.7). An underprediction problem was evident in the 4-km resolution
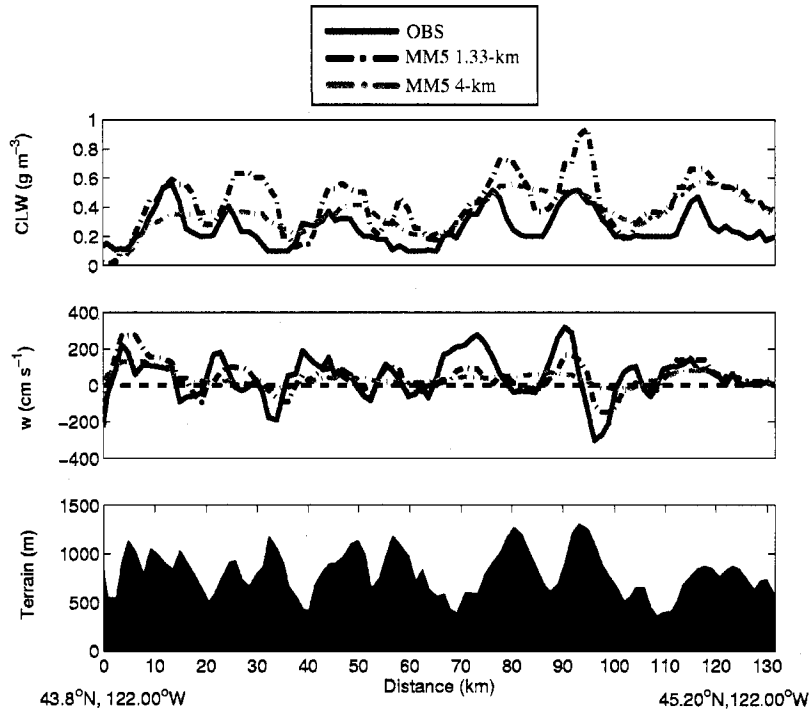
Figure 6.8: Comparison of cloud liquid water (CLW) and vertical velocity (w) for leg 2 of the P3 flight track. The solid blue line shows observed values. Green lines are values from the 4-km resolution MM5 simulation and the red lines are from the 1.33-km resolution MM5 simulation. The last panel shows the elevation of the underlying terrain.

simulation, with the model CLW values lower than the observed by $\sim$0.08 g m^{-3}.

Over the lee slopes of the Cascades, legs 4 and 5 of the P-3 were flown at heights of 4 and 3 km, respectively (Fig. 6.7). Measured CLW values were much lower than those in the earlier legs, averaging <0.05 g m^{-3}. Along leg 4, both the 4-km and 1.33-km resolution model simulations showed almost no CLW, which is a slight underprediction compared to the measurements. Along the final P-3 flight leg (Fig. 6.7), which was flown on the lee side of the Cascade Range, very little CLW was measured. The 4-km resolution model run accurately predicted low CLW (<0.1 g m^{-3}), while the 1.33 km resolution model run overpredicted CLW, averaging 0.1 g m^{-3} over the leg.

In addition to the in-situ flight-level measurements of CLW, a dual-channel radiometer was positioned at Santiam Junction, Oregon (SJ in Fig. 2.1) in close proximity to the Cascade crest and beneath the third P-3 flight leg. The radiometer provided integrated cloud liquid water depth (LWD), as described by Woods et al. (2005). Figure 6.9 shows the measured LWD for the entire 24-h period discussed in this thesis. Although some rain contamination may have occurred, the measured LWD represents a reasonably accurate depiction of the actual cloud LWD, as discussed by Woods et al. (2005). Note that the timing of the prominent peaks and trends in the simulated time series of LWD match quite closely with the observations, and that in the model time series these peaks and trends are dominated by cloud water, not rain (Woods et al., 2005). We continue this comparison under the assumption that the solid and dashed red lines represent the approximate observed and model simulated time series of cloud LWD, respectively.

Prior to 1800 UTC, the model underpredicted LWD, which is consistent with the radar comparison performed in Chapter 2, which showed the model's lack of prefrontal showers over the elevated terrain of the Cascades. Between 1800-0100 UTC 13-14 December the observed LWD was depleted by precipitating ice particles produced by the upper-level pre-cipitation band (Woods et al., 2005). The model prediction of cloud LWD was relatively accurate between 2000 UTC 13 December and 0100 UTC 14 December 2001, paralleling the observed LWD depletion. Immediately after the passage of the upper-level precipitation band, both the modeled and measured cloud LWD showed a sudden rebound (at 0200 UTC 14 December in Fig. 6.9), which was likely a result of the cessation of ice particles falling from above which ended the scavenging of CLW (Woods et al., 2005). After 0400 LWD remained low and precipitation was light.

6.5 Snow Particle Size Distributions

The measured mass concentrations and size distributions of snow particles obtained in the stacked flight legs of the Convair-580 between 4.9 km and 6 km in the upper-level alto-stratus cloud were compared with the model simulations for the three horizontal flight legs
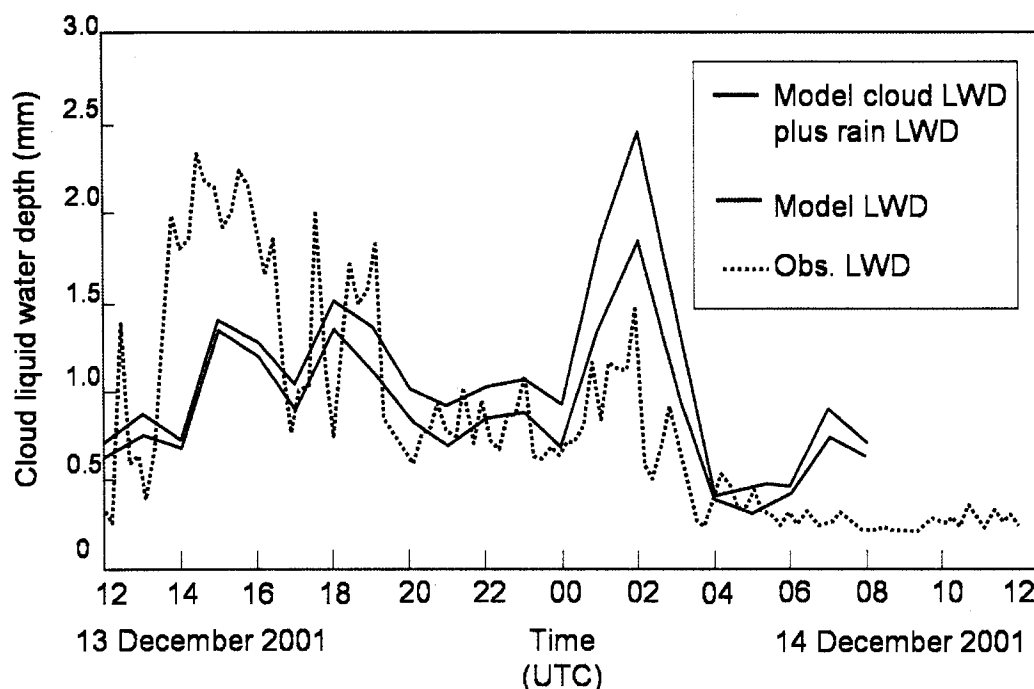
Figure 6.9: Vertically integrated liquid water depth (dashed red line) measured by the microwave radiometer (located at SJ in Fig. 2.1) from 1200 UTC 13 December 2001 through 1200 UTC 14 December 2001. Blue line is the modeled cloud liquid water depth plus rain water depth while solid red line is the modeled liquid water depth.

(legs 1, 2, and 3) and two descending legs (legs 1d and 2d) (Fig. 6.4). The measured mass concentrations were determined using the method described by Woods et al. (2005). The predominant hydrometeor observed along these upper-level flight legs was snow (consisting of cold-type and dendritic snow crystals), with negligible amounts of graupel. The measured snow mass concentrations increased from an average of 0.12 g m^{-3} along the highest leg (6 km) to 0.25 g m^{-3} as the Convair descended to 4.9 km (Table 6.1). In comparison, the model simulations of snow mass concentrations were 2 to 3 times larger than observed at the levels and locations corresponding to the Convair flight legs. Despite the ability of the model to predict accurately the spatial distribution of depositional snow growth aloft

Table 6.1: Comparison between observed and modeled mixing ratios (g m^{-3}) of snow and graupel along the Convair and P-3 flight tracks. See Fig 6.4 for key to flight legs.

Mixing Ratios along Flight Track (g/m^3)					
CONVAIR	Height (km)	q_s observed	q_s modeled	q_g observed	q_g modeled
Leg 1	6	0.12	0.33	0.00	0.00
Leg 1D	5.7	0.13	0.37	0.00	0.00
Leg 2	5.4	0.16	0.45	0.00	0.00
Leg 2D	5.2	0.21	0.49	0.00	0.00
Leg 3	4.9	0.25	0.55	0.00	0.00
P-3					
Lee	4.1	0.06	0.22	0.00	0.00
Win 1	4.1	0.09	0.73	0.31	0.08
Win 2	3.2	0.13	0.60	0.15	0.18

(see Fig. 6.5), the failure of the model to simulate correctly the snow mass concentrations (excessive amounts in the model) contributed to excessive spillover of snow to the lee of the Cascades.

A comparison of modeled versus measured snow particle size distribution also exposed potential errors in the model's BMP. The model assumes an exponential distribution for snow of the form

$$N(D) = N_{0,S}e^{-\lambda_s D} \tag{6.1}$$

with a slope (λ_s) and a temperature-dependent ordinate intercept ($N_{0,S}$) given by

$$N_{0,S} = min(2 \times 10^8, 2 \times 10^6 \times exp[-0.12min(-0.001, (T - T_0)] \tag{6.2}$$

where T_0 = 273.15°K and T is the ambient temperature in °K (Houze et al., 1979). The motivation behind a temperature-dependent value for $N_{0,S}$ is to parameterize the effects of aggregation (Thompson et al., 2004), which increases with temperature. Thus, as temperature increases the value of $N_{0,S}$ given by (2) decreases.

Along the UW Convair-580 flight route, snow size spectra were determined using measurements from a PMS 2D-C probe and a Stratton Park Engineering Company (SPEC)

Table 6.2: Comparison between observed and modeled fitted parameters for the size specta of particles for snow along the level and descending legs of the Convair flight tracks. Values of the slope intercept ($N_{0,S}$ in m^{-4}) and the slope (λ_s in m^{-4}) for snow are given. See Fig 6.4 for key to flight legs.

CONVAIR	Height (km)	$N_{0,S}$ observed	$N_{0,S}$ modeled	λ_s observed	λ_s modeled
Leg 1	6.0	2.78×10^7	2.73×10^7	2670	2251
Leg 1D	5.7	2.18×10^7	2.18×10^7	2462	2075
Leg 2	5.4	2.37×10^7	1.58×10^7	2309	1822
Leg 2D	5.2	3.16×10^7	1.25×10^7	2323	1686
Leg 3	4.9	4.94×10^7	1.06×10^7	2555	1567

high-volume spectrometer (HVPS). The technique used to combine ice crystal measurements from these two imaging probes to produce particle size spectra is described by Woods et al. (2005). Interestingly, the observed values of $N_{0,S}$ increased as the temperature increased from -20 to -17 °C between the first Convair flight leg at 6 km and the third horizontal leg at 4.9 km (Table 6.2). This is in contrast to (6.2), which predicts decreasing $N_{0,S}$ values with increasing temperature. Woods et al. (2005) suggest that the increase in the number of smaller particles with decreasing height along the Convair flight track may be due to an increase in the depositional growth and nucleation rate at these levels. This was inferred by the presence of newly formed unrimed plates along leg 3 at 4.9 km. Total precipitation particle (snow and graupel) size spectra along the P-3 cross-mountain transect [see Fig. 12 of Woods et al. (2005)], flown at elevations of 3.2 to 4 km, show a decrease in $N_{0,s}$ compared to the spectra measured aloft by the Convair, which is consistent with (2). These findings indicate that the value of $N_{0,s}$ depends on factors other than temperature, resulting in a misrepresentation of snow size spectra at low temperatures. The sensitivity of snow production in the MM5 model to $N_{0,s}$ will be shown in the next chapter.

In the MM5, the slope of the assumed snow particle size distribution is given by

$$\lambda_s = (\frac{\pi \rho_s N_{0,S}}{\rho q_S})^{\frac{1}{4}} \tag{6.3}$$

where ρ_S is an assumed density of snow ($100 \ kg \ m^{-3}$), ρ the density of air, and q_S the snow

mixing ratio (Reisner et al., 1998). Table 6.2 shows the variations in the measured and modeled values of λ_s. While the model accurately produced a decrease in the value of λ_s with decreasing altitude (i.e., increasing temperature), the combination of erroneous values for $N_{0,S}$ and λ_s results in marked discrepancies between the measured size distribution curves and those simulated by the model (Fig. 6.10). The measured size distributions are primarily exponential, which supports the assumption of a Marshall-Palmer distribution for snow. However, direct comparison of the measured versus modeled size spectra aloft shows an underprediction of the concentration of small snow crystals and a significant overprediction for snow particles >1.5 mm in diameter.

An analysis of mass spectra for the three legs of the Convair is shown in Fig. 6.11. The solid lines represent the observed mass spectra for the three level legs of the Convair using the best fit lines from Fig. 6.10 and assumed mass-diameter (M-D) relationship for cold type crystals [see Table 4 of Woods et al. (2005)]. There are insignificant differences in the mass spectra for the best fit lines and the actual size distribution. The dashed lines in Figure 6.11a are the modeled mass spectra given the parameterized value of No,s, the predicted value of qs (which together determine λ_s according to Eqn 6.3), and the model assumption of spherical particles with density one tenth that of liquid water. For the first three legs of the Convair the majority of the observed mass is due to snow particles between 0.5 and 1.5 mm. Due to the assumed size distribution and excessive snow amount in the model simulation, the majority of mass from the model comes from snow particles with diameters between 1 and 3 mm.

Figure 6.11b shows the number distributions for snow given a mass concentration (0.25 g m^{-3}) and N$_{0,S}$ value (4.94 × 10^4 m^{-3} mm^{-1}) and a variety of different M-D relationships. The mass concentration of snow and N$_{0,S}$ are the observed values for leg 3 of the Convair flight track. Four of the curves are based upon empirically derived M-D relationships (Woods et al. 2005), and the fifth is based on the model's assumption of spherical particles with constant density equal to one tenth that of liquid water. As seen in Figure 6.11b, dendrites and needles/sheaths would require the largest and most numerous amount of snow
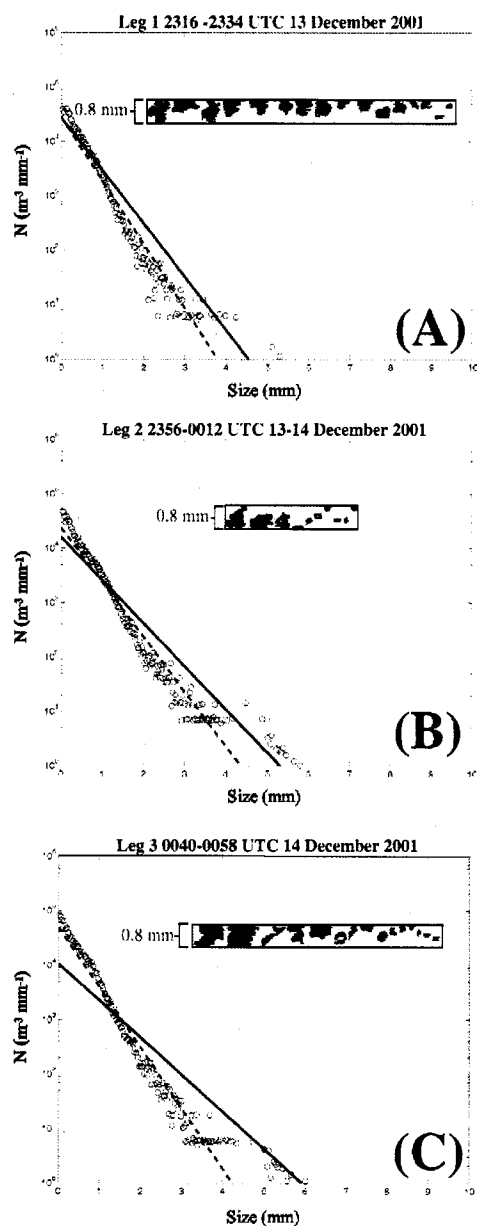
Figure 6.10: Observed and modeled number distributions of snow for (a) leg 1, (b) leg 2, and (c) leg 3 of the Convair flight track. Locations of legs are shown in Figure 6.4. Blue circles are the observed distribution, red dashed lines are best fit to observations, and black lines are 1.33-km resolution MM5 distributions. Sample images of ice crystals from the in-situ 2D-C probe are also shown.
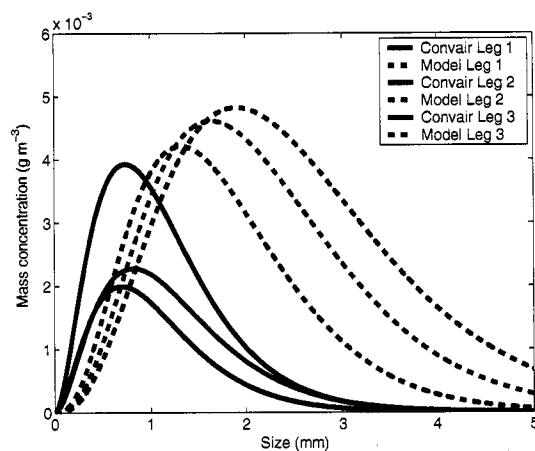
(a)
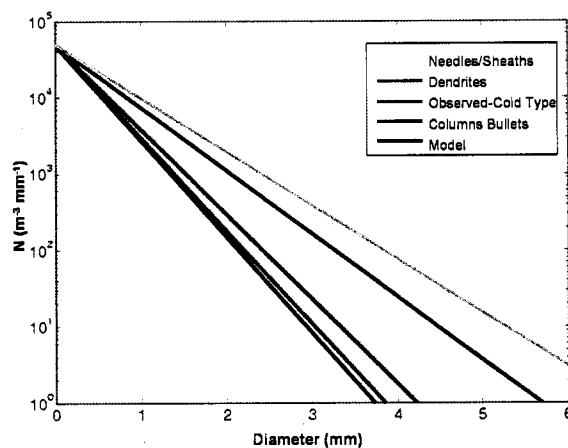
(b)

Figure 6.11: (a) Observed (solid lines) and modeled (dashed lines) mass concentrations of snow for three legs of the Convair flight track. Locations of legs are shown in Figure 6.4. (b) Number distributions for needles/sheaths (cyan), dendrites (blue), cold type crystals (magenta), and columns/bullets (red) given the mass concentration and $N_{0,S}$ observed for leg 3 of the Convair. Black line is number distribution with the same mass concentration and $N_{0,S}$ but with the assumed modeled bulk snow density of 100 kg m^{-3} and assuming spherical particles.

particles to attain a mass of 0.25 g m^{-3}. This is because the mass of a given diameter for dendrites and needles/sheaths is less than that for cold type crystals or bullets according to the empirically derived mass-diameter relationships. Conversely, since the density of snow particles in the model is much greater than that of any of the observed ice crystal habits, fewer and smaller snow particles are required to get the same mass. Therefore, even if the model managed to accurately predict the snow mass and correctly parameterize the intercept of snow, it would still underpredict the number and size of snow particles present. Such an error directly affects many of the key terms in the BMP, including growth of snow via deposition, riming of snow, and the fall speed of snow.

The spread of the lines in Fig. 6.11b illustrates that density actually varies considerably by given snow crystal habit, degree of riming, and aggregation etc., and that the assumption in the model for snow particle shape and density is not representative of the variety of observed particle types. Therefore, if parameters in the model (such as $N_{0,S}$) are taken from empirical formulas derived from experimental data, the snow densities or habits must be adjusted to more faithfully represent the observed particle types.

Comparisons of snow, graupel, and CLW mass concentrations measured at lower levels aboard the P-3 during its cross-mountain transect with those of the model simulations are shown in Fig. 6.12 and Table 6.1. Above the lee slopes, the predominant observed precipitation type was snow, with only minimal amounts of graupel. The model greatly overpredicted the amount of snow in this area, particularly close to the crest where strong downward vertical motions were present (Fig. 6.12). The model also appeared to overpredict the lee subsidence as seen by the vertical velocity. Over the windward Cascade slopes (labeled Win 1 in Table 6.1), the model also overpredicted the amount of snow, while underpredicting the amount of graupel. As mentioned previously, the definition of snow versus graupel in the model has important implications on precipitation amounts. As the P-3 progressed to the windward foothills and descended to 3.2 km, the model continued to overpredict snow amounts, but provided a relatively accurate portrayal of the graupel field.
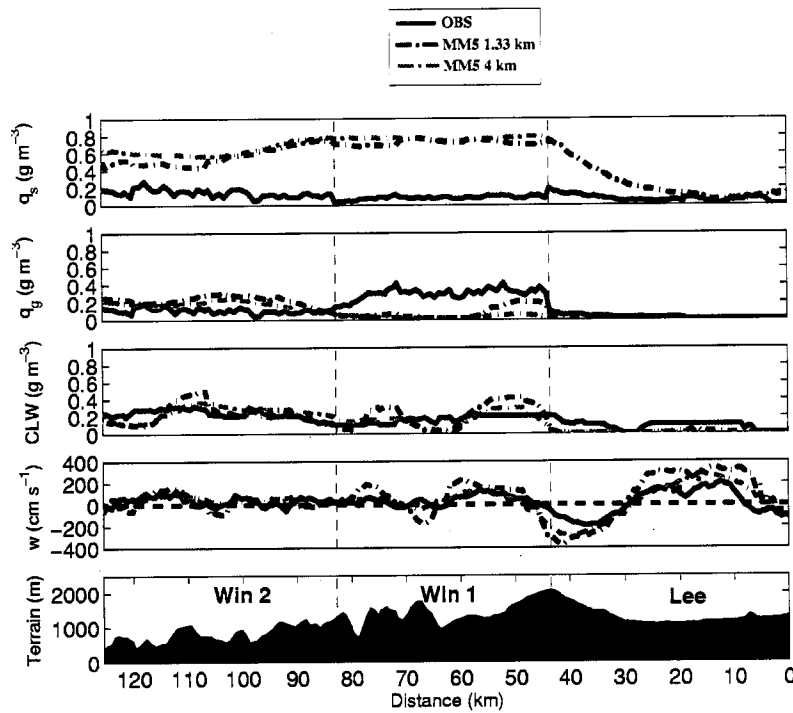
Figure 6.12: Snow (q_s), graupel (q_g), cloud liquid water (CLW) vertical velocity (w), and terrain along the P-3 flight track depicted in Fig. 6.4. The solid blue line are observed measurements, the red dashed lines are values from the 1.33-km resolution MM5 simulation, and green dashed lines are values from the 4-km resolution MM5 simulation. The last panel shows the elevation of the underlying terrain in meters.

6.6 Summary and Conclusions

Airborne in-situ measurements of the storm showed that at upper levels between 700 and 450 hPa, the growth of snow particles was dominated by depositional growth. The model replicated the volumetric extent of the snow particles and correctly indicated that the deposition of water vapor to snow was the predominant growth mechanism. However the model overpredicted the mass concentrations of snow particles in this area by a factor of 2-3. In addition, comparisons of measured and modeled snow particle size distributions between altitudes of 4.9 and 6 km showed that the model erroneously decreased the snow intercept

with decreasing height (i.e., increasing temperatures), while the measurements indicated an increase in the concentrations of small particles with decreasing height. Errors in the model simulations of the snow intercept and mass concentration contributed to the modeled slope of the snow distribution being less than observed, resulting in the model overpredicting the concentrations of moderate to large snow crystals and underpredicting the smaller particles.

Below the upper-level snow field, observations from the P3 showed a transition from snow to heavily rimed snow and graupel between 650 and 800 hPa over the windward slopes of the Cascades, with conversion of snow particles to graupel, riming of snow, and deposition being the predominant growth mechanisms. The model accurately simulated this transition, with the conversion of snow to graupel occurring around 650 hPa.

Closer to the crest, observations indicated a transition from cold-type snow crystals to a mix of graupel and densely rimed snow particles at 600 hPa along the P-3 flight track. The model simulation indicated that deposition and riming of snow were the predominant growth mechanisms over the crest between 600 and 650 hPa, yet indicated little to no production of graupel. This was reflected in the modeled mass concentrations, which continued to overpredict snow while underpredicting graupel. At lower levels along the P-3 flight track at 4.1 km, the model overpredicted the mass concentrations of snow in the immediate lee of the crest. This occurred in a region of substantial downward vertical velocity associated with a large amplitude mountain wave downwind of the crest.

Between 650-850 hPa, the model indicated that conversion of snow to graupel and melting of graupel were important processes, especially along the upper ridges of the windward slopes. In the simulation, melting of snow occurred in the valley sites and in the lee of the Cascade Crest where snow from aloft was advected downward in mountain waves. Over the windward foothills, snow mass concentrations were overpredicted by the model but the mass concentration of graupel was portrayed accurately. Along the lower-level P-3 flight track, the temperature-dependent intercept in the model represented the substantial observed decrease in the number of smaller particles.

Accretion of CLW by rain was also an important process over the windward slopes,

but due to the absence of measurements quantitative comparisons of the importance of this process could not be made. A comparison of CLW from a 1.33-km resolution model simulation with measurements of CLW along a flight track of the P-3 aircraft showed that the model greatly overpredicted CLW at lower levels over the Willamette Valley and the windward slopes of the Cascades. A 4-km resolution model run yielded CLW values closer to measurements but, in this case, the lower values of CLW appeared to be due to underprediction of vertical velocity. Over the mountain crest, the model underpredicted CLW, with the underprediction increasing over the immediate leeward slopes. Over the far lee slopes, both the model and measurements indicated minimal CLW.

The results of the microphysical analysis suggest that the excessive mass concentrations of snow aloft in the model simulations contributed to the overprediction of precipitation to the immediate lee of the Cascades. The excessive snow may have been due to errors in the representation of the depositional growth of snow and/or problems with the temperature-dependent intercept used in the model. Additional testing and analysis of the depositional terms and intercept parameter of snow should be done to isolate the errors that caused the excessive snow growth aloft from possible errors in model vertical velocity.

Observations also showed that snow density varies considerably for given snow crystal habit, degree of riming and aggregation, etc., and that the model assumption for snow particle shape and density is not representative of the variety of observed particle types. Therefore, if parameters in the model (such as $N_{o,s}$) are taken from empirical formulas derived from experimental data, snow densities and or snow habit types must also be adjusted to more faithfully represent the observations

This research suggests the importance of properly defining graupel versus snow in the model. Presently the fall speed for snow used in the model is based upon the Rutledge and Hobbs (1983) expression, which was derived for unrimed radiating assemblages of plates, side planes, bullets, and columns (Locatelli and Hobbs 1974). This parameterization of the snow fall speed does not consider riming processes, which are represented in the model in terms of snow growth but not in terms of increased snow fall velocity. Since the fall speed

of snow is significantly less then the fall speed for graupel or heavily rimed snow, there are important implications for where the precipitation species falls. A possible remedy for this problem might be to vary the fall speed of snow to take into account riming effects. The next chapter further explore the impacts of sensitivities in snow fall speed and the conversion threshold of snow to graupel on the amount of precipitation.

The fall speed of snow and the definition of snow versus graupel also have implications for the precipitation totals over the windward slopes. Microphysical budget analysis presented in the next chapter indicates that many of the rain gauge overpredictions in the immediate lee of the crest, as well as in some of the windward valleys, were associated with localized areas of snow melt in regions of subsidence where snow is brought down to the surface. Over the windward ridges, where the model appeared to correctly depict precipitation amounts, the major precipitation processes were the melting of graupel and the accretion of CLW by rain.

The transition from an overprediction of CLW over the windward slopes by the model to an underprediction over the crest and lee indicates the possibility that an excessive amount of ice was produced in the model at the expense of liquid water near the crest. Additionally, the overprediction of CLW on the windward slopes suggests that the updrafts might have been stronger than the model's rate of transfer of water mass from cloud droplets to precipitation particles.

Chapter 7

MICROPHYSICAL BUDGETS AND SENSITIVITY STUDIES

This chapter continues the model investigation of the 13-14 December 2001 event, by systematically evaluating several parameters within the Reisner2 BMP through a microphysical water/ice budget analysis and sensitivity tests. Insight in the orographic precipitation processes are also obtained. This is the first study to complete a full three-dimensional microphysical budget for a simulated orographic precipitation event using a complex BMP.

7.1 *Experimental Design*

Colle and Zeng (2004a) showed that by quantifying the relationship among water species, one can determine which microphysical process contributes most to the production and destruction of a specific hydrometeors. Figure 6.2 and equations 7.1-7.6 show how the various Reisner2 processes described in Colle and Zeng (2004a) are related through the water vapor (qv), cloud water (qc), cloud ice (qi), rain (qr), snow (qs) and graupel (qg) mixing ratios. The prognostic equations for each hydrometeor species described in Reisner et al. (1998) are:

$$
\begin{aligned}
\frac{d(p^*qv)}{dt} = \ & p^*(EVAP - COND + Pssub + Pgsub + \\
& Pisub + Prevp - Pidep - Pidsn - Psdep - \\
& Pgdep) + ADV(p^*qv) + DIV(p^*qv) + DIFF(qv)
\end{aligned}
\tag{7.1}
$$

$$\frac{d(p^*qc)}{dt} = p^*(COND - EVAP + Pimlt - Pccnr -$$

$$Pracw - Prgacw - Prsacw - Piacw - Pifzc -$$

$$Pihfzc - Pgiacw - Pggacw - Pgsacw - Pssacw) +$$

$$ADV(p^*qc) + DIV(p^*qc) + DIFF(qc) \tag{7.2}$$

$$\frac{d(p^*qi)}{dt} = p^*(Pidsn + Pidep + Piacw + Pifzc +$$

$$Pihfzc + Pispl - Picng - Praci - Psaci -$$

$$Picns - Pimlt - Pisub) + ADV(p^*qi) +$$

$$DIV(p^*qi) + DIFF(qi) \tag{7.3}$$

$$\frac{d(p^*qr)}{dt} = p^*(Pccnr + Pracw + Prsacw + Prgacw +$$

$$Psmlt + Pracs + Pgmlt + Pgacrm + Pgacwm -$$

$$Prevp - Piacr - Pgsacr - Pgacr - Pfzr +$$

$$Pssacr) + ADV(p^*qr) + DIV(p^*qr) - \mathbf{Prprc} \tag{7.4}$$

$$\frac{d(p^*qs)}{dt} = p^*(Psdep + Picns + Psaci + Psraci +$$

$$Psiacr + Pssacr - Pssub - Pracs - Psmlt -$$

$$Pgracs - Pscng) + ADV(p*qs) + DIV(p*qs) - \mathbf{Psprc} \tag{7.5}$$

$$\frac{d(p^*qg)}{dt} = p^*(Pgdep + Pgiacw + Pggacw + Pgsacw +$$

$$Pgiacr + Pgsacr + Pgacr + Pgfzr + Pscng +$$

$$Pgracs + Picng + Pgraci - Pgsub - Pgmlt - Pgacrm -$$

$$Pgacwm - Pispl) + ADV(p^*qg) + DIV(p^*qg) - \mathbf{Pgprc} \tag{7.6}$$

where p^* is the pressure difference between the surface and model top. The contributions from the microphysical processes are the first set of Pxxxx terms on the right hand side of Eqs 7.1-7.6, with advection (ADV) (horizontal/vertical), divergence (DIV) and diffusion (DIFF) also represented The bold term (**Pxxxx**) represents the fall out of a precipitable species.

The conversion rate for each term in equations 7.1-7.6 was output every 15 minutes

between forecast hours 16 and 20 of the control simulation (2200 UTC 13 December to 0200 UTC 14 December); however, most of the average budget analysis below is restricted to forecast hours 17 through 19 since this is the period of heaviest orographic precipitation. Following Colle and Zeng (2004a) the data was averaged for a box upstream of the crest (Fig. 5.8a). In order to determine the relative importance of each process in moving water mass from one hydrometeor category to another, each process was normalized by the integrated water vapor loss within that same box using

$$\overline{P}_{qqqq} \;=\; \frac{\sum_{i,j,k} p^*(i,j) \times P_{qqqq}(i,j,k) \times \Delta\sigma(k)}{\sum_{i,j,k} p^*(i,j) \times WVL(i,j,k) \times \Delta\sigma(k)} \tag{7.7}$$

where $P_{qqqq}(i,j,k)$ is the conversion rate of a specific microphysical process averaged for the two adjacent sigma levels, WVL is the water vapor loss rate (Cond+Pidsn+Pidep+Psdep +Pgdep), and $p^*\Delta\sigma$ is the pressure thickness of each layer, so that each layer is correctly weighted by its mass.

7.2 Microphysical Budget

Figure 7.1 shows the dominant microphysical processes averaged horizontally and vertically within the solid boxed region of Fig. 5.8a between 2300 and 0100 UTC. Each average process tendency was normalized by the water vapor loss (WVL) rate within the volume, with process values greater that 4% of the WVL rate highlighted in bold. The pathway to cloud water via condensation is the largest sink of water vapor over the windward slope (cond = 73% of WVL). Snow deposition (sdep) accounts for most of the remainder of the WVL (24%). Although ice initiation and ice deposition are small in terms of water mass (<3% of WVL), they are still important since cloud ice autoconverts to snow (icns) at relatively small sizes, and the snow grows rapidly via deposition and riming.

A large fraction of the cloud water is accreted by rain (racw = 27% of WVL), with little cloud water autoconversion present (ccnr << 1%). Most of the rain is initially produced by melting of snow and graupel. Accretion by rain accounts for more than half of the rain fallout over the windward slope, with the fallout scaling as 48% of WVL.
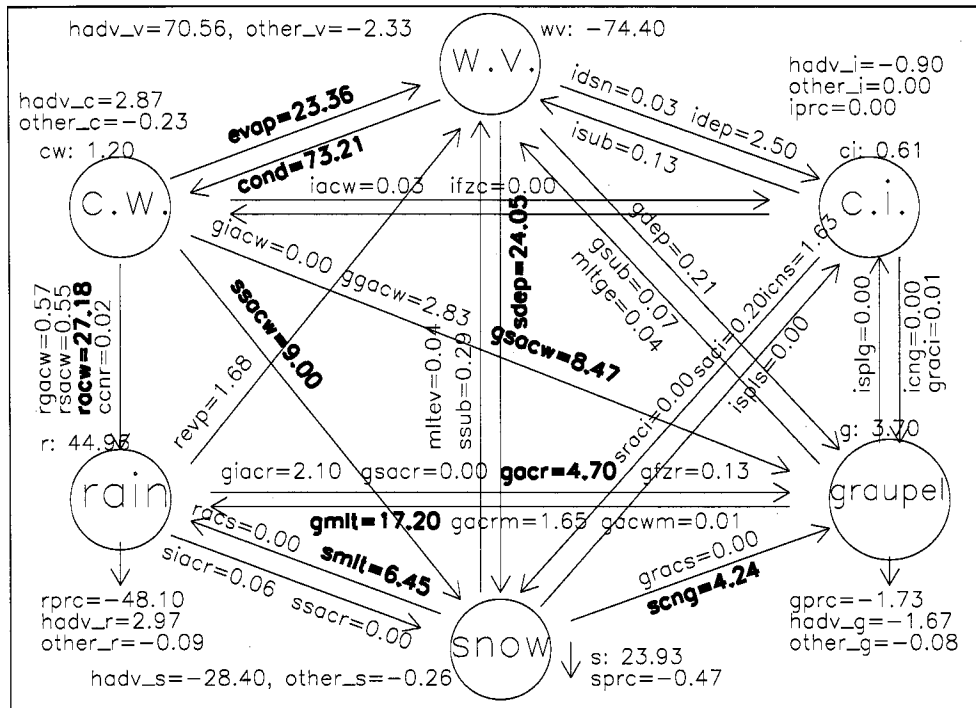
Figure 7.1: Flowchart of the microphysical processes between forecast hours 23-25 (2300-0100 UTC) of the control run for the box in Fig. 5.8a. The values shown are the ratio of each average microphysical process rate to the total water vapor loss (WVL) rate as defined in the text. For example, cond =73.21% means that 73.21% of the WVL results in condensation, and gsacw=6.47 means that the movement of cloud water mass to graupel is equivalent to 6.47% of the total WVL. Microphysical processes greater than 4% of the WVL rate are bold. The sum of all the microphysical process tendencies for each species is given by wv:, cw:, r:, ci:, and s:. This sum does not include horizontal advection and diffusion/divergence, which are labelled as hadv and other respectively. The fallout tendency of rain(rprc), snowsprc), graupel (gprc) and cloud ice(iprc are also shown.

Besides deposition, accretion of cloud water by snow (ssacw) is also a major contributor to snow growth via riming (9% of WVL). Of the snow generated over the windward slope, 16% (6% of WVL) melts to rain (smlt), 11% (4% of WVL) autoconverts to graupel during riming (scng), while 73% (28% of WVL) advects over to the lee of the barrier (hadv_s). The limited snow fallout over the windward slopes (sprc < 0.5% WVL) is consistent with

the relatively high freezing level (775 hPa) and the strong cross-barrier winds ($> 30 \text{ m s}^{-1}$) advecting hydrometeors into the lee.

Half of the snow accretion of cloud water (ssacw) results in snow growth via riming, while the remainder contributes to 50% of the graupel production over the windward slope (gsacw scales as 9% of WVL). The other half of graupel production originates from riming of graupel by rain (gacr) and conversion of snow to graupel (scng). Nearly all the graupel that is produced melts and falls as rain over the windward slope (gmlt scales as 17% of WVL). Graupel melt is the second most common source of rain and it is three times larger than snow melt over the windward slope; therefore, riming processes were important in windward precipitation generation. Woods et al. (2005) showed using aircraft data and rain gauges that riming within the windward "feeder" cloud was important in enhancing the surface precipitation. The large pathway to surface precipitation via graupel melt is also consistent with the lack of profound flow blocking observed by aircraft during this event, which has been shown to favor more graupel production over the steep windward slope of barriers (Medina and Houze, 2003).

The windward precipitation efficiency (PE) is defined as the total amount of fallout of hydrometeors over the windward slopes divided by the total WVL within this same area. The windward PE can be obtained by adding the fallout terms in the microphysical budget (rpsc, sprc, and gprc in Fig. 7.1), since the fallout is normalized by the WVL. The windward PE for the control run is 50%, so only half of the windward WVL leads to surface precipitation upstream of the crest. Over half of the condensate is lost by snow advection into the lee (hadv_s = 28%),while the remainder is lost via evaporation (evap=23%). The simulated PE for this case is lower than that recently diagnosed for the Sierras (PE = 80%) using MM5 (Colle and Zeng, 2004a), since the Cascades are narrower and the cross barrier flow during this IMPROVE event was twice as strong.

7.3 Horizontal Microphysical Budget Analysis

The previous section showed the averaged microphysical budget over the windward slope for a 3-h period. However, to illustrate the small-scale variability over the narrow ridges and valleys across the windward slopes of the Cascades, select processes are plotted horizontally and averaged for a 100-hPa vertical layer centered where the snow, graupel, and rain growth are a maximum (Figs 7.2-7.4).

The snow deposition and riming processes for the 1.33-km domain were averaged between 450 and 550 hPa and 500 and 600 hPa layers, respectively, for the period 2300-0100 UTC 14 December (Fig 7.2). Snow deposition is largest over the middle and upper windward slopes (50 x 10^5 kg s^{-1}), with localized areas of 50% less production in the lee of some windward ridges. The depositional growth increases 20-30 km upstream of the windward slope since the upward motion increases aloft approaching the terrain. The collection of cloud water by snow (riming) also increases snow growth 20-30 km upstream of the barrier, and it is maximized (> 40 x 10^5 g^{-1} kg s^{-1}) between 500 and 600 hPa over some of the steep windward slopes. This supports the findings in Chapter 6 showing that gravity waves forced by the narrow ridges can have a profound impacts on the model microphysical processes at relatively high levels.

Figure 7.3 shows the graupel production terms averaged between 700 and 600 hPa. The largest graupel source is the collection of cloud water by snow (gsacw) over the windward slopes (Fig. 7a). There are large areas of gsacw upstream of the crest (40-60 x 10^5 g kg^{-1} s^{-1}), with the greatest area (80-100 x 10^5 g kg^{-1} s^{-1}) immediately upstream of the Cascade crest. Meanwhile, the autoconversion of snow to graupel (scng) is specified in Reisner2 to be exactly half of gsacw (not shown), and it is the second largest contribution to graupel. The collection of cloud water by graupel (gacw) is largest over the lower windward slope and has magnitudes of 10-20 x 10^{-5} g kg^{-1} s^{-1} (Fig. 7.3b). The collection of rain by graupel occurs over a similar location as ggacw (not shown), but with about half the magnitude.
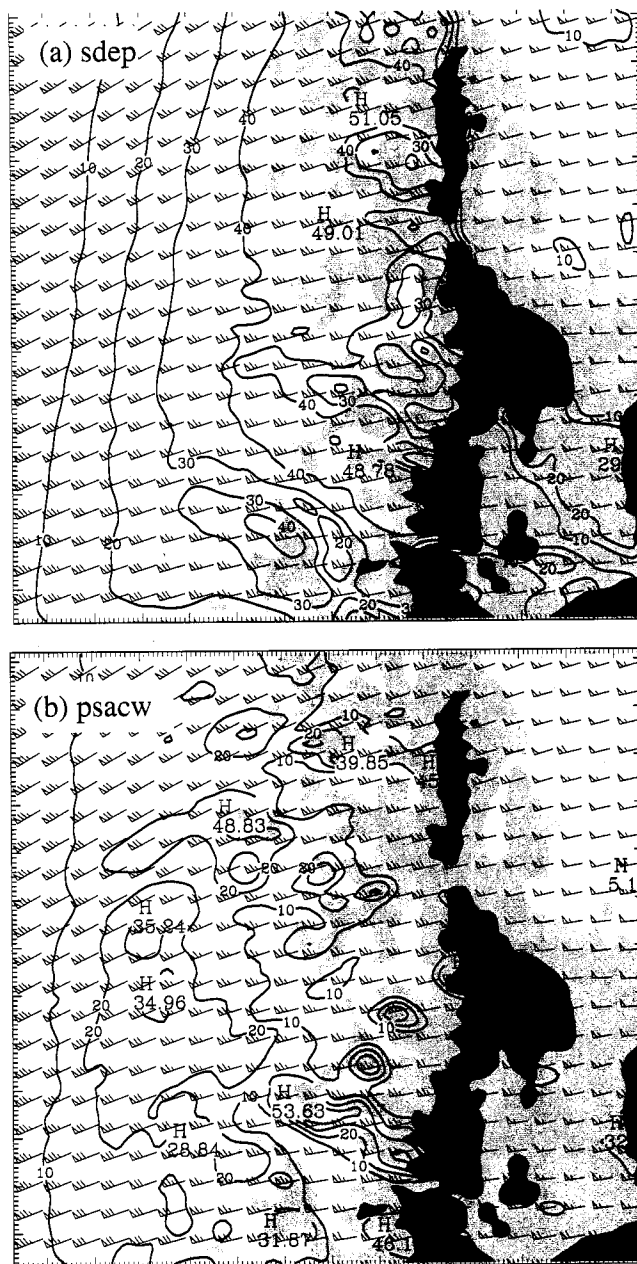
Figure 7.2: (a) Snow deposition every $10 \times 10^5 \text{g kg}^{-1} \text{ s}^{-1}$ and winds (1 full barb = 10kts) averaged between 450 and 550 hPa using 15 minute microphysical output from the 1.33-km domain for 2300-0100 UTC 14 December. (b) Same as (a) except for the accretion of cloud water by snow averaged between 500 and 600 hPa. Terrain from the 1.33-km domain is shaded for reference.

Figure 7.3: (a) Same as Fig. 7.2 except for the 600 to 700 hPa layer showing graupel growth via (a) accretion of cloud water by snow water (every $10 \times 10^5 \mathrm{g\ kg^{-1}\ s^{-1}}$) and (b) accretion of cloud water by graupel.

The rain production is plotted horizontally for the layer just below the melting level between 850 and 750 hPa (Fig. 7.4). Accretion of cloud water by rain is largest along the steep areas of the lower windward slopes ($> 150 \times 10^5$ g kg^{-1} s^{-1}) (Fig. 7.4a). Most of the rain precipitation generated over the middle windward slope is from melting of graupel, with localized maximum ($> 250 \times 10^5$ g kg^{-1} s^{-1}) in the immediate lee of the windward ridges. Meanwhile, there is a large amount of snow melt in the lee of the Cascades ($> 500 \times 10^5$ g kg^{-1} s^{-1}) (Fig. 7.4b), and there are some localized maxima of snow melt associated with spillover into some of the windward valleys under strong southwesterly flow.

Chapter 5 and Fig 5.8a showed a sharp gradient in model bias scores across the central Cascades. One can attempt to relate the gauge verification to the model microphysical processes in order to determine which hydrometeor species may have contributed to the model precipitation errors. Within a valley on the windward slopes (Fig. 7.4a), there are rapid transitions in the model bias scores within short distances (less that 10-15 km). Figure 7.4 shows bias scores ranging from 120% of observed precipitation (X) at the western edge of the valley to 205% (O) and 165% (o) for stations slightly farther eastward. The furthermost west point (X) has little contribution to rain from snow melt, while the gauge 10 km to the east has a 40-50% contribution from snow melt associated with the spillover over the ridge to the south (Fig. 7.4b). Farther up the windward slope of the Cascades the precipitation is within 130% of observed, and this area is dominated by graupel melt and fallout (Fig. 7.4c). Meanwhile, there is large overprediction in the lee of the Cascade crest again associated with snow melt. These results suggest that one reason for the model overprediction is the large snow melt to the lee of the Cascade crest and windward ridges.

7.4 Sensitivity Tests

A set of experiments were completed using different microphysical parameters within Reisner2 to quantify the process sensitivities for the 13-14 December event. The model microphysics are evaluated during the 2300-0100 UTC period using different intercepts for the number concentration of snow, a slower snow fall speed, a decreased threshold for snow
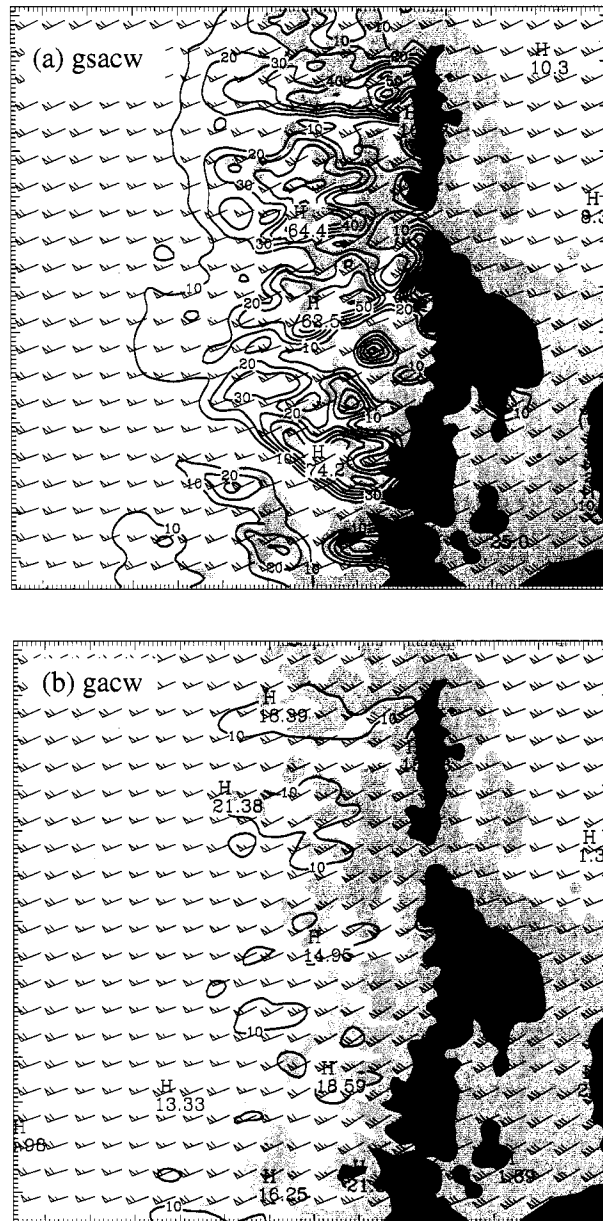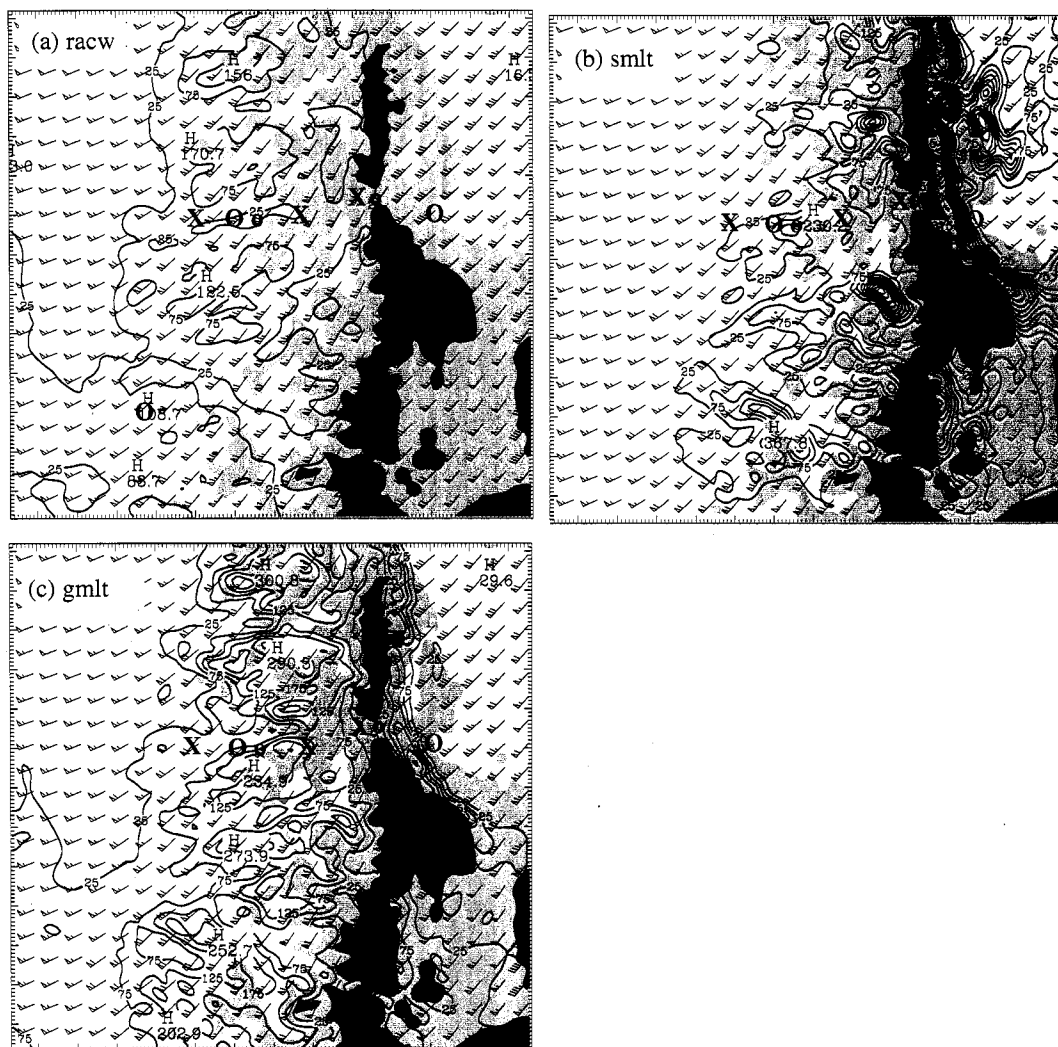
Figure 7.4: (a) Same as Fig. 7.2 except for the 850 to 750 hPa layer showing rain growth via (a) accretion of rain by cloud water (every 10 x 10^5g kg^{-1} s^{-1}) (b) snow melt and (c) graupel melt. A transect of rain gauge locations are shown across the Cascades, with model precipitation within 30% of the observed shown by a 'X', greater than 130% of observed by an 'o', and greater than 180% observed by an 'O' for the 2000 UTC 13 December to 0200 UTC 14 December period.

riming, a different cloud water autoconversion, and two other simplified BMPs within the MM5. The goal of these sensitivity simulations is not to find a fix to the BMP, but to focus primarily on those processes, which are important to snow and graupel growth. The following section provides summaries of the important sensitivity tests. For a more complete discussion the reader is referred to Colle et al. (2005).

7.4.1 Intercept for snow number concentration (N_{os})

The intercept in the Marshall-Palmer distribution of snow influences the snow fallout, riming, deposition and melting of snow. For this first series of experiments, the snow intercept parameter (N_{os}) in the control (CTL), which depends on temperature (Eqn. 6.2), was changed to either a fixed $N_{os} = 2 \times 10^7$ m^{-4} as in other well-known BMPs (Lin et al., 1983; Rutledge and Hobbs, 1983) or a function of snow mixing ratio as described in Reisner et al. (1998). The N_{os}(T) approach used in the control run is designed to parameterize the decreasing number concentration of snow associated with the aggregation process at warmer temperatures. Using a N_{os}(T) results in less snow crystals than a fixed N_{os} for temperatures warmer than -19°C. Meanwhile, a intercept dependent on the snow mixing ratio (N_{os}(qs), Reisner et al. 1998) typically favors more large snow particles and fewer small particles than the other parameterized N_{os}(T).

Using a fixed N_{os}, there are large differences compared to the CTL in the amount of snow, cloud water, and graupel. Since a fixed N_{os} allows more snow particles than N_{os}(T) at relatively warm temperatures, snow mass is increased by 50% in the 500-750 hPa layer for a fixed N_{os}. The increased number of snow particles in this layer also acts to deplete the available cloud water, and therefore decreases graupel production. The snow and graupel differences with the CTL are largest over the barrier around 700 hPa, where there are large vertical motions and snow accretional processes (cf. Fig. 6.5b). The additional snow produced aloft by the fixed N_{os} is in the opposite direction needed to improve the model. A fixed N_{os} favors a microphysical pathway involving slightly more snow deposition (wv$\Rightarrow$sdep$\Rightarrow$snow) rather than graupel production via riming (wv$\Rightarrow$cond$\Rightarrow$ggacw,

gsacw⇒graupel). These changes are consistent with the greater number of snow parti-cles using fixed N_{os} at cold temperatures, which can more efficiently deplete the available supersaturated water vapor.

Using a fixed also N_{os} reduces the precipitation by 5-10 mm (15%) over many areas of the upper windward slopes due to a decrease of graupel and rain fallout. Meanwhile, the increase in snow aloft results in more lee side spillover, where there is 25 mm (20%) more precipitation in the lee than the CTL. Unfortunately, this is in the opposite direction needed to improve the forecast in the lee.

Using a $N_{os}(qs)$ relationship favors a broader snow distribution, with fewer snow par-ticles at colder temperatures. As a result, snow is reduced by 0.5 g kg^{-1} over the upper windward slope and crest as compared to the CTL. The decrease in snow is almost com-pletely offset by the increase in cloud water and graupel. This additional cloud water above the crest is needed to improve the verification given the underprediction shown for this region. There is little difference with the CTL upstream of the barrier where the vertical motions are weak.

$N_{os}(qs)$ results in a 60% reduction in snow deposition over the barrier. As a result, the amount of snow advection (hadv_s) is reduced by 40% as compared to the control and there is slightly less snow melt (smlt) and accretion of cloud water by snow (ssacw), which was closer to observations. Meanwhile, the pathway to cloud water and cloud ice is increased, with 10% more condensation than in the CTL run and over twice as much cloud ice deposition. The increased cloud water results in slightly more rain accretion and fallout as well as accretion by snow to form graupel. The greater graupel and rain than the CTL results in 5-15 mm more precipitation over much of the windward slope region using the $N_{os}(qs)$ with worsened bias scores in this region. Less snow in the lee results in 5-15 mm less in the lee of the Cascades with slightly better verification.

7.4.2 Snow fallspeed (Vs)

Both Colle and Mass (2000) and Colle and Zeng (2004a) showed that precipitation fallout in the MM5 is strongly dependent on the snow fallspeed. The CTL uses the Rutledge and Hobbs (1983) expression for fallspeed, which was derived for an unrimed radiating assemblages of plates, side planes, bullets and columns (Locatelli and Hobbs, 1974). This fallspeed is 20-30% larger than for unrimed radiating assemblages of dendrites (Ferrier, 1994; Cox, 1988). A separate simulation was completed using the slower COX fallspeed to demonstrate the sensitivity and ramifications of switching to this relationship.

The COX trajectories originating as snow above 600 hPa fall out 20-30 km farther downwind than the CTL. There is less snow falling out over the upper windward slope in the COX, which results in less riming and graupel. The slower fallspeed results in 5-15 mm less precipitation near the crest and 5-15 mm more storm total precipitation in the lee as compared to the CTL. Additional lee side precipitation is a problem, since it already adds to an existing positive bias in this region. Snow deposition also decreased for the COX run, since more snow is advected across the barrier above the layer of greatest depositional growth around 525 hPa. This reduction in snow growth is accompanied by less snow riming below 600 hPa. The windward PE decreases from 50% in the CTL to 46% given the additional spillover of snow into the lee with the slower COX fallspeed.

7.4.3 Snow accretion of cloud water

An accurate prediction of the partition between snow and graupel aloft is important since more (less) graupel favors faster (slower) precipitation fallout over the windward slope. The initial generation of graupel in Reisner2 is determined primarily by the snow to graupel autoconversion (scng), and this process is initiated when the amount of snow riming (psacw) exceeds depositional growth (sdep) by a factor of 2.5 (Thompson et al., 2004). An experiment was completed in which this factor was reduced to 1.0 (Murakami, 1990), a threshold, which was applied in earlier versions of Reisner2 (Reisner et al., 1998). Reduc-

ing this threshold favors more snow to graupel autoconversion in the area of riming below 500 hPa. The reduction in snow results in less depletion of super-cooled water around 600 hPa, so cloud water was increased by 0.15 g kg^{-1} over the windward slope.

Also, with more autoconversion from snow to graupel there is less snow available for depositional growth and riming, so these terms for snow growth decrease compared to the control. Meanwhile, condensation increases and there is more accretion of cloud water and rain by graupel. As a result of the increased microphysical pathway to more rain and graupel fallout, the windward precipitation efficiency increases from 50% in the CTL to 53%. Enhanced graupel increases the precipitation by 5-10 mm (5-10%) over the windward ridges, while the precipitation within some of the windward valleys is decreased by 5-10 mm. This reduction of valley precipitation reduces the overprediction shown in Fig. 5.3. The largest impacts are in the immediate lee of the Cascades, with reduced snow spillover resulting in 10-15 mm (10-15%) less precipitation, which helps reduce some of the overprediction.

7.4.4 Cloud water autoconversion

The CTL simulation used the Berry and Reinhardt (1974) method for the cloud to rain autoconversion, which is described in Reisner et al. (1998). For several years the Kessler (1969) approach was utilized in Reisner2, which uses a threshold (0.35 g kg^{-1}) and a simple Heaviside function to do the conversion. The CTL approach resulted in very little autoconversion in the windward mass budget (cf. Fig. 7.1); therefore, another simulation was completed using Kessler (KESS). This approach increased the autoconversion, and the amount of cloud water in the average cross section decreased. The reduction of cloud water also reduces the riming growth of snow over the lower windward slope and graupel over the crest by an equivalent amount. As result, this decreases the snow and cloud water over-predictions noted in the previous chapter. The KESS run has 5-30 mm more precipitation over some of the steeper windward slopes; however, the vertical differences in mixing ratio using KESS are smaller than the ice sensitivities shown above.

7.4.5 Simple ice and warm rain schemes

In order to further quantify the importance of riming processes on the surface precipitation, the simulation was rerun without these processes. Specifically, a simulation was completed using the "simple ice" BMP (SICE), which neglects super-cooled water, and only includes snow and cloud ice below 0°C with no riming or graupel processes. The SICE scheme also uses a fixed N_{os} approach to the snow number concentration; therefore, the results can be compared to the fixed N_{os} run above.

Since liquid water below 0°C can not exist aloft in SICE, the microphysical pathway is dominated by depositional growth, resulting in a snow maximum immediately over the crest that is nearly double that of the Reisner2 CTL run. This maximum in snow in SICE gets advected into the immediate lee, resulting in a well defined rain maximum in this region and nearly twice as much precipitation as the control, which makes the lee side overprediction problem much worse. Meanwhile, there is less fallout of rain over the upper windward slope by 20-30 mm (30-40%) since there is no contribution by graupel melt or cloud water accretional processes aloft. The combination of a fixed N_{os} and no super-cooled water aloft results in much more spillover of precipitation in the SICE run, which is the opposite trend needed to improve upon the CTL run.

On the other hand, some ice is important, as demonstrated by a simulation using the warm rain scheme (WRAIN) with no ice processes. This scheme is dominated by condensational and rain accretional processes; therefore, a broad area of rain exists over the lower windward slope that is 20-40% greater than the CTL. There are also sharper gradients of precipitation upstream of the Cascades and in the immediate lee in the WRAIN since there is no snow fallout from aloft into these regions. As a result, the surface precipitation is reduced by half in the immediate lee of the Cascades and nearly doubled in many areas of the windward slopes.

128

7.5 Summary and Conclusions

A systematic evaluation of several parameters within the Reisner2 BMP was performed by using a microphysical water/ice budget analysis for a 3-hour period characterized by relatively heavy orographically enhanced precipitation during the 13-14 December 2001 event. During the 2300 UTC 13 December to 0100 UTC 14 December period, the largest water vapor loss rate over the windward slope of the Cascades in the 1.33 km domain was associated with condensation (73% of WVL) and snow deposition (24%). The cloud water led to accretion of cloud water by rain, which resulted in more than half the rain fallout integrated over the windward slope. A large fraction of cloud water also led to riming of snow and graupel over the windward ridges, with graupel fallout and melt contributing to the second most important source of windward surface precipitation.

Snow fallout and melt were relatively small on average along the windward slope because of the significant spillover into the immediate lee. Yet, many of the model overpredictions in the immediate lee of the Cascades as well as some of the windward valleys were associated with localized areas of snow melt. This result was also highlighted in Chapter 6, which showed that Reisner2 produced nearly twice as much snow as observed over the windward slope at mid-levels.

Several parameters were evaluated within the Reisner2 BMP. The surface precipitation was most sensitive to the snow size distribution and fallspeed, while decreasing the riming threshold for snow to graupel conversion had the greatest positive impact on the precipitation forecast. The partition between condensation and deposition and the resulting surface precipitation is strongly affected by the method used to define the snow intercept parameter (N_{os}). Using a fixed N_{os} approach favors smaller snow particles and fewer larger ones at warmer temperatures, so deposition of snow aloft was more than twice as large as using a N_{os} approach that is a function of mixing ratio. A fixed N_{os} reduced the precipitation by 5-10 mm (15%) over many areas of the upper windward slopes due to a decrease of graupel and rain fallout; however, the additional snow aloft resulted in more overprediction in the

immediate lee. This is consistent with a separate simulation using a simple ice scheme, which includes no super-cooled water and a fixed N_{os} approach, and this resulted in the worst precipitation simulation. Having some ice and snow aloft is important, since a warm rain run with no ice resulted in too little precipitation in the immediate lee of the Cascades.

These experiments suggest that the ice growth rates in the model were greater than observed and the model broadened the size distribution too rapidly; therefore, model growth processes such as deposition, riming, and aggregation need closer analysis in future studies. Simulating the proper ice distribution and riming aloft is also dependent on the N_{os} parameter for snow, so this parameter may need a more advanced relationship than just a function of temperature or mixing ratio. Finally, additional field cases must be analyzed to determine the generality of the model verification and microphysical sensitivities presented in this study.

Chapter 8

SUMMARY AND CONCLUSIONS

This chapter discusses the major results of the thesis and provides suggestions for future research. A description of the multiscale mountain waves observed during the 13-14 December event and their influence on precipitation distributions is highlighted. Additionally, errors in the important microphysical parameters and assumptions inherent to the model BMP are discussed and suggestions for improvement are provided.

8.1 Motivation and Description of the 13-14 December 2001 Event

During 13-14 December 2001, a comprehensive set of observations over the central Oregon Cascades was collected as part of the IMPROVE-2 field project, permitting an unprecedented opportunity for the investigation of a heavy precipitation event over complex terrain. The unique dataset included microphysical measurements from the UW Convair-580 research aircraft, radial velocity and reflectivity observations from the NCAR S-band dual-polarization radar (S-Pol), as well as airborne Doppler and in situ measurements from the National Oceanic and Atmospheric Administration (NOAA) P-3 research aircraft. The data gathered by these and other observational platforms allowed for a comprehensive analysis of the 13-14 December storm and extensive verification of a mesoscale model simulation. The collection of the thermodynamic and kinematic observations concomitantly with microphysical measurements provided a unique chance to isolate errors in the model's microphysical parameterizations, which may be contributing to errors in QPF.

The 13-14 December 2001 event featured the passage of a strong forward-tilting frontal system and large area of stratiform precipitation. The Fifth Generation Penn State / NCAR Mesoscale Model (MM5) V3.5 was run at various resolutions to simulate the system. The

MM5 was able to represent accurately the synoptic-scale features associated with the storm system, including the depiction of the tipped-forward structure of the front, the upstream moisture profile, and the strength of the associated baroclinic zone. The performance of the model in simulating the synoptic features associated with the 13-14 December 2001 storm system was sufficiently accurate to permit further comparisons of mesoscale and microphysical data with the model provided that errors in the simulated speed of the low-level jet and the slope of the front above 650 hPa were taken into account when performing the verification.

8.2 Multiscale Mountain Waves and Precipitation Distribution

Analysis of the model was primarily focused on the prefrontal period when precipitation rates were the highest and dual-Doppler coverage was most extensive. Two high-resolution simulations with 4-km and 1.33-km grid spacing were compared with in situ and airborne Doppler observations. The spatial coverage of the in situ and Doppler data provided a unique opportunity to obtain detailed descriptions of terrain-induced perturbations over complex terrain on a variety of scales. The Doppler observations greatly supplemented the in situ measurements by providing a fully three-dimensional, uninterrupted view of reflectivity and kinematic fields spanning the complex terrain of the Cascades, extending from the Willamette Valley eastward to the lee slopes.

The MM5 depicted a layer of low θ and θ_e air associated with strong low-level meridional (V) flow adjacent to the highest terrain. The gradient in θ values were consistent with reflectivity observations from the P-3 dual-Doppler showing the bright band sloping downward to the Cascade crest. Trajectory analysis indicates that the low-θ air originated to the south of the study area in a region of sub-saturation. A strong vertical gradient in θ (and θ_e) lay atop the U-shear zone and coincident with a decrease in the V-component. Parcels within the strong U-component airstream originated well west of the study area over the Pacific in an area of high-θ and saturation. As this high-θ_e air approached the mountainous study area, it experienced acceleration and lifting, rising over the low-θ_e air (Fig 8.1). The
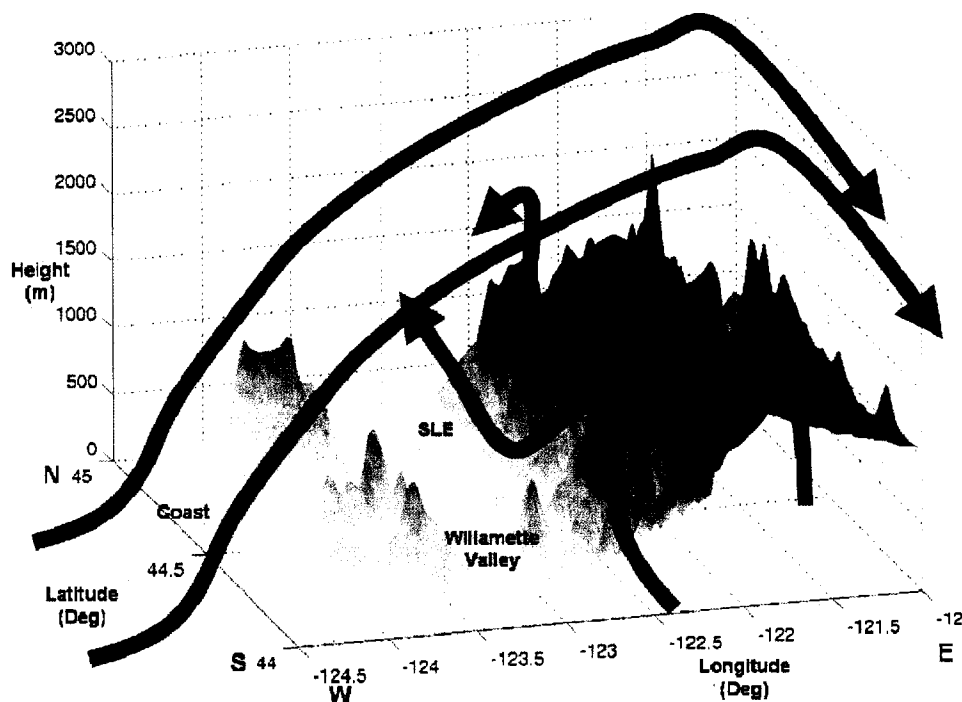
Figure 8.1: Three dimensional idealized schematic of topography, and wind flow over the IMPROVE study area from 2300-0100 UTC 13-14 December 2001. Blue arrows show strong southerly low-θ_e air flow at low-levels along the windward (west-facing) slopes of the Cascade range, which was subsequently involved in wave generation over multiple small-scale E-W oriented ridges/valleys within the Cascade foothills. Red arrows show the high-θ_e cross barrier flow that surmounted the low-θ_e air and exhibited a vertically propagating mountain wave structure anchored to the mean N-S Cascade crest.

kinematic structure of the 13-14 December 2001 case, with low-level along barrier flow and a strong cross-barrier jet atop a sloping shear-layer, was also present in other IMPROVE and MAP cases (Medina et al., 2005). It would be useful to further examine more cases in IMPROVE and MAP to document the repeatability and generality of the phenomena established in this thesis.

8.2.1   Larger-Scale Wave over the Cascade crest

As the strong cross-barrier flow surmounted the barrier, dual-Doppler observations showed the high U-momentum air plunging downward in the immediate lee of the Cascade crest as part of a vertically propagating mountain wave. The MM5 also depicted this feature, but the simulated strong U-momentum air clearly reached closer to the ground and over a larger horizontal distance than observed. Collocated with the higher reflectivity values over the Cascade crest, simulated maximum snow mixing ratios extended from ~40-km upstream of the crest to the immediate lee. The enhanced snow mixing ratios and observed reflectivities originated in an area of dendritic growth and strong vertical ascent associated with the mountain wave over the mean crest. The high snow mixing ratios were subsequently advected beyond (i.e., east of) the barrier in the strong cross-barrier flow before being deposited in the immediate lee of the Cascades.

The gravity wave's modulation of the snow field resulted in reduced modeled surface precipitation near the crest and an area of markedly enhanced precipitation totals in the immediate lee. Although this precipitation distribution could not be extensively verified against observations, an examination of observed precipitation amounts from 1400-0800 UTC 13-14 December 2001 indicated some tendency for reduced precipitation totals near the crest versus over the windward slopes and in the immediate lee. The strong gradient in simulated snow mixing ratio to the lee of the Cascades was in close agreement with an observed reduction of radar reflectivity values. Despite this qualitative agreement, numerous sites in the lee of the Cascades experienced a substantial overprediction, with bias scores of greater than 150 percent. The results of a comprehensive microphysical analysis suggest that the excessive mass concentrations of snow aloft in the model simulations contributed to this overprediction of precipitation to the immediate lee of the Cascades. The excessive snow may have been due to errors in the representation of the depositional growth of snow and/or problems with the temperature-dependent intercept for snow distributions used in the model. Additional testing and analysis of the depositional terms and intercept parame-

ter of snow should be done to isolate the errors that caused the excessive snow growth aloft from possible errors in model vertical velocity.

To assess the impact of the shear and boundary layer depth on the simulated mountain wave, a variety of sensitivity tests were completed using three different planetary boundary layer parameterization (PBL) schemes. It was shown that all of the PBL schemes underpredicted the height of the U-shear layer and produced U-flow that was too strong at the surface. The PBL tests clearly indicated that the amplitude and strength of the mountain wave are extremely sensitive to the upstream shear layer and choice of PBL-parameterization. The incorrect depiction of the upstream shear layer in the simulation could be an important source of errors in the strength and amplitude of the modeled lee wave and precipitation overprediction to the lee of the Cascades. It is therefore imperative that errors in the model boundary layer parameterizations and depiction of the upstream shear layer be corrected in order to further improve quantitative precipitation forecasts over terrain.

8.2.2 Smaller-Scale Waves over the Windward Slopes

It was also seen that short-wavelength perturbations in the meteorological variables were present along the N-S legs of the P-3 flight track especially over the windward slopes of the Cascades (Fig 8.1). These variations in vertical velocity, temperature, wind direction, and wind speed were directly related to small-scale mountain waves caused by the complex terrain. The 1.33-km model's vertical velocity field compared well with the Doppler and in situ observations, simulating the dramatic oscillations associated with the strong southerly component of the flow interacting with the complex terrain. The model vertical velocity oscillations were stronger than the corresponding signatures of the smoothed Doppler-derived w-field but wholly consistent with values obtained through analysis of the in situ flight level data. The simulated w-oscillations also showed greater vertical penetration than the Doppler data and were probably closer to reality given the artificial boundary condition of $w=0$ at echo top imposed in the dual-Doppler analysis. It was found the model required a 1.33 km grid spacing to capture the small scale oscillations.

Model depictions of the precipitation and CLW fields over the windward slopes showed that complex microphysical interactions were produced by these locally strong vertical velocity perturbations. Pockets of high CLW were present over individual ridges, and shown to be associated with upstream areas of strong upward vertical velocity above upslope portions of the underlying terrain. Where the upper-level snow field intersected with these high CLW pockets, riming of the snow particles and graupel formation above the 0°C level was indicated by the model. The rimed snow particles and graupel evidently resulted in enhancement of the observed bright band over and immediately leeward of the ridge crests as these particles fell through the melting layer. The increase in precipitation rates was illustrated by the higher mixing ratios of rain over the crest and to the immediate lee of several of the ridges. These windward-slope waves exhibited horizontal scales far greater than the turbulence-induced vertical motions shown by Houze and Medina (2005), which developed within a layer of enhanced vertical shear that is prominent in both airborne Doppler analyses and MM5-simulated flow patterns detailed. The turbulence-related oscillations, whose inferred horizontal wavelengths were in the 1-2 km range, represent yet another scale of vertical perturbations that might potentially contribute to orographic enhancement of precipitation.

An analysis of the model QPF between 2200-0100 UTC showed that the small-scale waves increased the modeled precipitation amounts over the windward slopes by 4-14% compared to a smoothed terrain model simulation. Yet during this 3-hour period, the smoothed terrain resolution did not significantly alter the total amount of precipitation over the domain, but instead redistributed the precipitation in different areas. When a longer 18-hour period was considered, which included prefrontal, frontal, and postfrontal precipitation regimes, the total precipitation amount over the windward slopes showed a net increase of 12% over the smoothed simulation. This increase appeared to be directly tied to an increase in CLW production and precipitation over the windward slopes caused by the smaller-scale wave perturbations.

The 1.33-km domain bias scores indicated substantial variability over relatively short

distances along the windward slopes. QPF data from nineteen sites along the windward slopes were examined and placed into two categories: ridge and valley. There appeared to be tendency for high bias scores to be present over the valley sites, while over the ridges bias scores appear to be near one. Sensitivity tests and microphysical budget analyses indicated that many of the model overpredictions in the the valleys were associated with localized areas of snow melt in regions of localized subsidence. Over the windward ridges, where the model appeared to correctly depict precipitation amounts, the major precipitation processes were the melting of graupel and the accretion of CLW by rain. The precipitation distribution at the surface was therefore very sensitive to the amount of riming, the fall speed of the particles, and the phase and amplitude of the small-scale waves. Due to the relatively small number of measurements, possible errors in precipitation gauges, and sparse distribution of precipitation sites, further analysis of future storms is needed to validate this trend.

8.3 Microphysical Analysis and Sensitivity Tests

From the modeling-based and observational analyses performed on the 13-14 December 2001 event, several microphysical assumptions and parameters were identified that require further research as summarized below.

8.3.1 Intercept of snow distribution ($N_{o,s}$)

Analysis of the 13-14 December 2001 case has illustrated potential problems with the intercept (N_{os}) and slope (λ_s) parameter for snow. The model produced a broader distribution of snow particles than was observed, underestimating the amount of smaller particles and overestimating the amount of larger particles. In addition, comparisons of measured and modeled snow particle size distributions showed that the temperature-dependent $N_{o,s}$ erroneously decreased the slope intercept with decreasing height (i.e., increasing temperatures), while the measurements actually indicated an increase in the concentrations of small particles with decreasing height. Sensitivity studies for the 13-14 December case

showed that the intercept of snow had a significant impact on the predicted quantity and fall speed of snow, which greatly affected precipitation totals. Therefore any modifications to this parameter will have substantial impacts on the QPF. Continued analyses of the large IMPROVE data set will assist in quantifying an improved parameterization for the snow intercept parameter.

8.3.2   CLW

The transition from an overprediction of CLW over the windward slopes by the model to an underprediction over the crest and lee indicates the possibility that an excessive amount of ice was produced in the model at the expense of liquid water near the crest. Additionally, the overprediction of CLW on the windward slopes suggests that the updrafts might have been stronger than the rate at which the model scheme could transfer water substance from cloud water to precipitation particles. Idealized studies quantifying the sensitivity of CLW amounts to model vertical velocity are suggested to better understand CLW formation within the model and compare it to observations.

8.3.3   Density of snow (ρ_s)

The model assumes a bulk density of snow of 100 kg m^{-3} that appears to originate from the results of a 19th century study (Roebber et al., 2003). Yet comprehensive measurements of snow density have established that this value is an inadequate characterization of the actual range of density for snow crystals. Observations have shown that snow density varies considerably for given snow crystal habit, degree of riming and aggregation, etc., and that the model assumption for density is not representative of the variety of observed particle types. The study by Roebber et al. (2003) showed ρ_s ranging from 21.4 to 526 kg m^{-3} with a mean density of 80.9 kg m^{-3}. For the 13-14 December 2001 storm system microphysical observations indicated the mean densities of snow crystals ranging from 40-80 kg m^{-3} (Chris Woods, personal communication, 2004) depending on crystal type. Therefore, if

138

parameters in the model (such as $N_{o,s}$) are taken from empirical formulas derived from experimental data, the snow densities and/or particle habits must also be adjusted to more faithfully represent the observed particle types.

8.3.4   Diameter Definitions

Potter (1991) and McFarquhar and Black (2004) have touched on the inconsistent definitions of snow diameter, fall speeds for snow, $N_{o,s}$, ρ_s and λ_s. For example, some parameterizations for the number distributions of snow are based upon relationships derived from equivalent liquid diameter of snow while fall speed algorithims were based on a maximum diameter of snow crystals. In the past, differences in the diameters were commonly ignored. Using the microphysical data set gathered in IMPROVE, refined parameterizations using a consistent definition of diameter can be devised.

8.3.5   Growth of snow via deposition

The results of the research suggest that excessive mass concentrations of snow aloft in the model simulations contributed to the overprediction of precipitation to the immediate lee of the Cascades. The excessive snow may have been due to errors in the representation of the depositional growth of snow and/or problems with the temperature-dependent intercept used in the model. The depositional term is highly dependent on the ambient supersaturation and $N_{o,s}$, making it a complex process that needs to be explored in depth. Additional testing and analysis of the depositional terms and intercept parameter of snow should be done to isolate the errors that caused the excessive snow growth aloft from possible errors in model vertical velocity. Accurately measuring synoptic or barrier-scale vertical velocity is presently very difficult, if not impossible. Therefore, additional sensitivity tests, idealized simulations, or laboratory work is necessary to investigate possible problems associated with the depositional term.

8.3.6   Definition of Snow and Graupel

The research completed suggests the importance of properly defining graupel versus snow in the model. Presently the fall speed for snow used in the model is based upon an expression originated by Rutledge and Hobbs (1983), which was derived for unrimed radiating assemblages of plates, side planes, bullets, and columns (Locatelli and Hobbs, 1974). This parameterization of the snow fall speed does not consider riming processes that can be correctly depicted in the model. Since the fall speed of snow is significantly less than that for graupel or heavily rimed snow, there are important implications for where the precipitation species falls. A possible remedy for this problem might be to vary the fall speed of snow to take into account possible riming effects. Additionally, when looking at fall speed and mixing ratios it is important that precipitation rate also be investigated.

BIBLIOGRAPHY

Baumgardner, D., 1983: An analysis and comparison of five water droplet measuring instruments. *J. Climate and Appl. Meteor.*, **22**, 891–910.

Benjamin, S. G. and N. L. Seaman, 1985: A simple scheme for objective analysis in curved flow. *Mon. Wea. Rev.*, **84**, 1184–1198.

Berry, E. X. and R. Reinhardt, 1974: An analysis of cloud drop growth by collection. part IV: A new parameterization. *J. Atmos. Sci.*, **31**, 2127–2135.

Bond, N., 2003: Personal communication.

Bond, N. A., C. F. Mass, B. F. Smull, R. A. Houze, M.-J. Yang, B. A. Colle, S. A. Braun, M. A. Shapiro, B. R. Colman, P. J. Neiman, J. E. Overland, W. D. Neff and J. D. Doyle, 1997: The coastal observation and simulation with topography (COAST) experiment. *Bull. Amer. Meteor. Soc.*, **78**, 1941–1955.

Bougeault, P., P. Binder, A. Buzzi, R. Dirks, R. Houze, J. Kuettner, R. B. Smith, R. Steinacker and H. Volkertand, 2001: The MAP special observing period. *Bull. Amer. Meteor. Soc.*, **82**, 433–462.

Bousquet, O. and B. F. Smull, 2003a: Airflow and precipitation fields within deep Alpine valleys observed by airborne Doppler radar. *J. Appl. Meteor.*, **42**, 1497–1513.

Bousquet, O. and B. F. Smull, 2003b: Observations and impacts of upstream blocking during a widespread orographic precipitation event. *Quart. Roy. Meteor. Soc.*, **129**, 391–409.

Brown, P. R. A., 1970: *Terminal Velocities of ice crystals*. Master's thesis, Colorado State University.

Browning, K. and N. Roberts, 1996: Variation of frontal precipitation structure along a cold front. *Quart. Roy. Meteor. Soc.*, **122**, 1845–1872.

Bruintjes, R. T., T. Clark and W. D. Hall, 1994: Interactions between topopgraphic airflow and cloud/precipitation development during passage of a winter storm in Arizona. *J. Atmos. Sci.*, **51**, 275–285.

Cairns, M. M. and J. Corey, 2003: Mesoscale model simulations of high-wind events in the complex terrain of western Nevada. *Wea. Forecasting.*, **18**, 249–263.

Colle, B., M. F. Garvert and J. Wolfe, 2005: Simulations of the 13-14 December 2001 IMPROVE-2 event, Part 3: Microphysical budgets and sensitivities. *J. Atmos. Sci.*, **62**, 3535–3558.

Colle, B. and C. F. Mass, 1996: An observational and modeling study of the interaction of low-level southwesterly flow with the Olympic Moundains during COAST IOP 4. *Mon. Wea. Rev.*, **124**, 2152–2175.

Colle, B. and C. F. Mass, 2000: The February 5-9 1996 flooding event over the Pacific Northwest: Sensitivity studies and evaluation of the MM5 precipitation forecasts. *Mon. Wea. Rev.*, **128**, 593–617.

Colle, B., J. B. Olson and J. S. Tongue, 2003: Evaluation of high-resolution precipitation forecasts over the Northeastern United States. *Wea. Forecasting.*, **18**, 458–480.

Colle, B., K. Westrick and C. F. Mass, 1999: Evaluation of MM5 and Eta-10 precipitation forecasts over the Pacific Northwest during the cool season. *Wea. Forecasting.*, **14**, 137–154.

Colle, B., K. Westrick and C. F. Mass, 2000: MM5 precipitation verification over the Pacific Northwest during the 1997-99 cool season. *Wea. Forecasting.*, **15**, 730–744.

Colle, B. and Y. Zeng, 2004a: Bulk microphysical sensitivities and pathways within the MM5 for orographic precipitation. Part I, the Sierra 1986 event. *Mon. Wea. Rev.*, **132**, 2780–2801.

Colle, B. and Y. Zeng, 2004b: Bulk microphysical sensitivities within the MM5 for orographic precipitation. Part II: Impact of barrier width and freezing level. *Mon. Wea. Rev.*, **132**, 2802–2815.

Colle, B. A., M. Garvert, J. A. W. Cox, W. J. Steenburgh, D. E. Kingsmill, J. Wolfe and C. P. Woods, 2004: Comparisons Between IMPROVE-2 and IPEX Kinematic and Precipitation Structures and Bulk Microphyscial Verification. *11th Conference on Mountain Meteorology and the Annual Mesoscale Alpine Program (MAP).*

Cox, G., 1988: Modeling precipitation in frontal bands. *Quart. Roy. Meteor. Soc.*, **114**, 115–127.

Cox, J., J. Steenburgh, D. E. Kingsmill, J. C. Shafer, B. A. Colle, O. Bousquet, B. F. Smull and H. Cai, 2005: The kinematic structure of a Wasatch mountain winter storm during IPEX IOP3. *Mon. Wea. Rev.*, **133**, 521–542.

Doyle, J. D., D. R. Durran, C. Chen, B. A. Colle, M. Georgelin, V. Grubisic, W. R. Hsu, C. Y. Huang, D. Landau, Y. L. Lin, G. S. Poulos, W. Y. Sun, D. B. Weber, M. G. Wurtele and M. Xue, 2000: An intercomparison of model-predicted wave breaking for the 11 January 1972 Boulder windstorm. *Mon. Wea. Rev.*, **128**, 901–914.

Dudhia, J., 1989: Numerical study of convection observed during the Winter Monsoon Experiment using a mesoscale two-dimensional model. *J. Atmos. Sci.*, **46**, 3077–3107.

Durran, D., 2003: Lee waves and mountain waves. *Encyclopedia of Atmospheric Science.* Elsevier Science Ltd.

Durran, D. and J. Klemp, 1982: On the effects of moisture on the Brunt-Väisälä frequency. *J. Atmos. Sci.*, **39**, 2152–2158.

Einaudi, F. and D. Lalas, 1973: The propagation of acoustic gravity waves in a moist atmosphere. *J. Atmos. Sci.*, **30**, 365–376.

Ferrier, B. S., 1994: Double-moment multiple-phase four-class bulk ice scheme. Part I: Description. *J. Atmos. Sci.*, **51**, 249–280.

Fovell, R. G. and Y. Ogura, 1988: Numerical simulation of a midlatitude squall line in two dimensions. *J. Atmos. Sci.*, **45**, 3846–3879.

Fritsch, J. M., R. A. Houze., R. Adler, H. Bluestein, L. Bosart, J. Brown, F. Carr, C. Davis, R. H. Johnson, N. Junker, Y.-H. Kuo, S. Rutledge, J. Smith, Z. Toth, J. W. Wilson, E. Zipser and D. Zrnic, 1998: Quantitative precipitation forecasting: Report of the eighth prospectus development team, U.S. Weather Research Program. *Bull. Amer. Meteor. Soc.*, **79**, 285–299.

Frush, C. L., P. H. Hildebrand and C. Walther, 1986: The NCAR airborne Doppler radar. Part II: System design considerations. *23rd Radar Meteorology Conference*, AMS, 151–154, Snowmass, CO.

Garvert, M. F., B. Colle and C. Mass, 2005: 13-14 December 2001 storm system. Part 1. Synoptic and mesoscale evolution and comparison with a mesoscale model simulation. *J. Atmos. Sci.*, **62**, 3474–3492.

Grell, G. A., 1993: Prognostic evaluation of assumptions used by cumulus parameterizations. *Mon. Wea. Rev.*, **121**, 764–787.

Hildebrand, P. H., 1998: Shear-parallel moist convection over the tropical ocean: A case study from 18 February 1993 TOGA COARE. *Mon. Wea. Rev.*, **126**, 1952–1976.

Hobbs, P. V., 1975: The nature of winter clouds and precipitation in the Cascade mountains and their modification by artificial seeding. Part I. Natural conditions. *J. Appl. Meteor.*, **14**, 783–804.

Hong, S.-Y. and H. L. Pan, 1996: Nonlocal boundary layer vertical diffusion in a medium range forecast model. *Mon. Wea. Rev.*, **124**, 2232–2339.

Houze, R., 1993: *Cloud Dynamics.* Academic Press.

Houze, R., P. Hobbs, P.H.Herzegh and D. Parsons, 1979: Size distributions of precipitation particles in frontal clouds. *J. Atmos. Sci.*, **36**, 156–162.

Houze, R. and S. Medina, 2005: Turbulence as a mechanism for orographic precipitation enhancement. *J. Atmos. Sci.*, **62**, 3599–3623.

Hsie, E.-Y., R. A. Anthes and D. Keyser, 1984: Numerical simulation of frontogenesis in a moist atmosphere. *J. Atmos. Sci.*, **41**, 2581–2594.

Janjic, Z. I., 1990: The step-mountain coordinate: Physical package. *Mon. Wea. Rev.*, **118**, 1429–1443.

Janjic, Z. I., 1994: The step-mountain Eta coordinate model: Further developments of the convection, viscous sublayer, and turbulence closure schemes. *Mon. Wea. Rev.*, **122**, 927–945.

Jorgensen, D. P. and B. F. Smull, 1993: Mesovortex circulations seen by airborne Doppler radar within a bow-echo mesoscale convective system. *Bull. Amer. Meteor. Soc.*, **74**, 2146–2156.

Kessler, E., 1969: On the distribution and continuity of water substance in atmospheric circulations. *Meteor. Monograph*, **32**, 84.

King, W. D., J. E. Dye, , J. Strapp, D. Baumgardber and D. Haffman, 1985: Icing wind tunnel tests in the CSIRO liquid water probe. *J. Atmos. Oceanic Technol.*, **2**, 340–352.

King, W. D., D. A. Parkin and R. J. Handsoworth, 1978: A hot wire liquid water device having fully calculated response characteristics. *J. Appl. Meteor.*, **17**, 1809–1813.

Knollenburg, R., 1976: Three new instruments for cloud physics measurements: The 2-D spectrometer, the forward scattering spectrometer probe, and the active scattering aerosol spectrometer. *Conf Cloud Physics*.

Lawson, R., R. Stewart, J. Strapp and G. Issac, 1993: Aircraft observation of the origin and growth of very large snowflakes. *Geophys. Res. Lett.*, **20**, 53–56.

Lin, Y., R. Farley and H. Oriville, 1983: Bulk parameterization of the snow field in a cloud model. *J. Climate and Appl. Meteor.*, **22**, 1065–1092.

Locatelli, J. and P. Hobbs, 1974: Fall-speeds and masses of solid precipitation particles. *J. Geophys. Res.*, **79**, 2185–2917.

Locatelli, J., M. Stoelinga, M. F. Garvert and P. V. Hobbs, 2005: Variation of frontal precipitation structure along a cold front. *J. Atmos. Sci.*, **62**, 3431–3455.

Magono, C. and C. W. Lee, 1966: Meteorological classification of natural snow crystals. *J. Fac. Sci.*, **2**, 321–335.

Manning, K. W. and C. A. Davis, 1997: Verification and sensitivity experiments for the WISP94 MM5 forecasts. *Wea. Forecasting.*, **12**, 719–735.

Marwitz, J. D., 1982: The kinematics of orographic airflow during sierra storms. *J. Atmos. Sci.*, **40**, 1218–1227.

Marwitz, J. D., 1987a: Deep orographic storms over the sierra nevada. Part I: Thermodynamic and kinematic structure. *J. Atmos. Sci.*, **44**, 159–173.

Marwitz, J. D., 1987b: Deep orographic storms over the sierra nevada. Part II: The precipitation processes. *J. Atmos. Sci.*, **44**, 174–185.

McFarquhar, G. M. and R. A. Black, 2004: Observations of particle size and phase in tropical cyclones: Implications for mesoscale modeling of microphysical processes. *J. Atmos. Sci.*, **61**, 422–439.

Medina, S. and R. Houze, 2003: Air motions and precipitation growth in alpine storms. *Quart. Roy. Meteor. Soc.*, **129**, 345–371.

Medina, S., B. Smull, R. Houze and M. Steiner, 2005: Cross-barrier flow during orographic precipitation events: Results from MAP and IMPROVE. *J. Atmos. Sci.*, **62**, 3850–3598.

Meyers, M. P. and W. R. Cotton, 1992: Evaluation of the potential for wintertime quantitative precipitation forecasting over mountainous terrain with an explicit cloud model. Part I: Two-dimensional sensitivity experiments. *J. Appl. Meteor.*, **31**, 26–50.

Murakami, M., 1990: Numerical modeling of dynamical and microphysical evolution of an isolated convective cloud - the July 1981 CCOPE cloud. *J. Meteorol. Soc. Jpn.*, **128**, 107–128.

Neiman, P. J., F. M. Ralph, A. B. White, D. E. Kingsmill and P. O. Persson, 2002: The statistical relationship between upslope flow and rainfall in california's coastal mountains: Observations during CALJET. *Mon. Wea. Rev.*, **130**, 1468–1492.

Noh, Y., W. G. Cheon, S. Y. Hong and S. Raasch, 2003: Improvement of the K-profile model for the planetary boundary layer based on large eddy simulation data. *Boundary-Layer Meteorology.*, **107**, 401–427.

Peng, M. S. and W. T. Thompson, 2003: Some aspects of the effect of surface friction on flows over mountains. *Quart. Roy. Meteor. Soc.*, **129**, 2527–2557.

Potter, B. E., 1991: Improvements to a commonly used cloud microphysical bulk parameterization. *J. Appl. Meteor.*, **30**, 1040–1042.

Rauber, R., 1992: Microphysical structure and evolution of a central Sierra Nevada orographic cloud system. *J. Appl. Meteor.*, **31**, 3–24.

Ray, P., C. Ziegler, W. Bumgarner and R. Serafin, 1980: Single and multiple Doppler radar observations of tornadic storms. *Mon. Wea. Rev.*, **108**, 1607–1625.

Reisner, J., R. Rasmussen and R. Bruintjes, 1998: Explicit forecasting of supercooled liquid water in winter storms using the MM5 mesoscale model. *Quart. Roy. Meteor. Soc.*, **124**, 1071–1107.

Reynolds, D. W. and D. S. Arnett, 1986: A review of the sierra cooperative pilot project. *Bull. Amer. Meteor. Soc.*, **67**, 513–523.

Roebber, P. J., S. L. Bruening, D. M. Schultz and J. V. C. Jr, 2003: Improving snowfall forecasting by diagnosing snow density. *Wea. Forecasting.*, **18**, 264–287.

Rotunno, R. and R. Ferretti, 2001: Mechanisms of intense Alpine rainfall. *J. Atmos. Sci.*, **58**, 1732–1749.

Rutledge, S. A. and P. V. Hobbs, 1983: The mesoscale and microscale structure and organization of clouds and precipitation in midlatitude cyclones. VIII: A model for the seeder-feeder process in warm-frontal rainbands. *J. Atmos. Sci.*, **40**, 1185–1206.

Rutledge, S. A. and P. V. Hobbs, 1984: The mesoscale and microscale structure and organization of clouds and precipitation in midlatitude cyclones. XII: A diagnostic modeling study of precipitation development in narrow cold-frontal rainbands. *J. Atmos. Sci.*, **41**, 2249–2972.

Smith, R. B., 1979: The influence of mountains on the atmosphere. *Advances in Geophysics*, Vol. 21, pp. 135–137. Academic Press.

Smith, R. B., 1989: Hydrostatic airflow over mountains. *Advances in Geophysics*, **31**, 1–41.

Stauffer, D. R. and N. L. Seaman, 1990: Use of four-dimensional data assimilation in a limited-area mesoscale model. Part I: Experiments with synoptic scale data. *Mon. Wea. Rev.*, **118**, 1250–1277.

Stauffer, D. R., N. L. Seaman and F. S. Binkowski, 1991: Use of four-dimensional data assimilation in a limited-area mesoscale model. Part II: Effects of data assimilation within the planetary bounday layer. *Mon. Wea. Rev.*, **119**, 734–754.

Steenburgh, J. and C. Mass, 1996: Interaction of an intense extratropical cyclone with coastal orography. *Mon. Wea. Rev.*, **124**, 1329–1352.

Stoelinga, M., P. V. Hobbs, C. F. Mass, J. D. Locatelli, B. A. Colle, R. A. Houze, A. L. Rango, N. A. Bond, B. F. Smull, R. M. Rasmussen, G. Thompson and B. R. Coleman, 2003: Improvement of Microphysical Parameterizations through Observational Verification Experiments IMPROVE. *Bull. Amer. Meteor. Soc.*, **84**, 1807–1826.

Thompson, G., R. R. Rasmussen and K. Manning, 2004: Explicit forecasts of winter precipitation using and improved bulk microphysics scheme. Part I: Description and sensitivity analysis. *Mon. Wea. Rev.*, **132**, 519–542.

Varley, D., 1980: Microphysical properties of large scale cloud systems. Environmental research paper 690, Air Force Geophysics Laboratory.

Wang, J., D. Carlson, D. Parsons, T. Hock, D. Lauritsen, H. Cole, K. Beierle and E. Chamberlain, 2003: Performance of operational radiosonde humidity sensors in direct comparison with a chilled mirror dew-point hygrometer and its climate implication. *Geophys. Res. Lett.*, **30**, 1–4.

Westrick, K. W., 1998: *A coupled high resolution hydrometeorlogical modeling study of a cool-season flood event in a coastal mountainous watershed.* Master's thesis, University of Washington.

White, A. B., J. R. Jordan, B. E. Martner, F. M. Ralph and B. W. Bartram, 2000: Extending the dynamic range of an S-band radar for cloud and precipitation studies. *J. Atmos. Oceanic Technol.*, **17**, 1226–1234.

Woods, C., M. T. Stoelinga, J. D. Locatelli and P. V. Hobbs, 2005: Cloud structures and microphysical processes during the December 13, 2001 IMPROVE 2 event. *J. Atmos. Sci.*, **62**, 3493–3519.

Yu, C. K. and B. F. Smull, 2000: Airborne observations of a landfalling cold front upstream of steep coastal orography. *Mon. Wea. Rev.*, **128**, 1577–1603.

VITA

Matthew Garvert was born in Washington DC in September 1975. Starting at a young age, Matt developed an insatiable interest in the weather and anything related to it. After graduating high school, Matt attended Colgate University and graduated with an Economics degree in 1997. He then moved to Seattle in 1999 to pursue his real passion, atmospheric sciences.